universität wien

MAGISTERARBEIT

Titel der Magisterarbeit

Head Tail High Velocity Clouds:

A possibility to test the theory of dark matter mini-halos

Verfasserin

Sylvia Plöckinger Bakk. rer. nat.

angestrebter akademischer Grad

Magistra der Naturwissenschaften (Mag. rer. nat.)

Wien, im Oktober 2009

Studienkennzahl lt. Studienblatt	A 066 861
Studienrichtung lt. Studienblatt	Astronomie
Betreuer	Univ.-Prof. Dipl.-Phys. Dr. Gerhard Hensler

Contents

Chapter 1

Introduction

High velocity clouds (HVCs) are gas clouds containing neutral hydrogen (HI) with velocities that are out of character referring to the differential rotation of the galactic disk. They were first predicted by Spitzer in 1956. In his publication he made several theoretical considerations about an "interstellar galactic corona" having a temperature of about 10^6 K with embedded gas clouds consisting of neutral hydrogen with typical temperatures of about 100 K and densities of about 10 atoms/cm^3. Münch (1956) was looking for cloud signatures in the spectra of O and B stars with galactic latitudes of more than 30°, having apparent luminosities of more than 8.0 mag. Because stars with distances larger than 500 pc show more complex lines, Spitzer assumed that a large fraction of these clouds are more than 500 pc away. Without any surrounding medium, the pressure in that space would be only 5 % of that in the galactic plane. In such an environment the cloud would expand at the speed of sound and its pressure would approach the environment's pressure in about 10^7 years.

> "Thus we may conclude that the measures by Münch suggest strongly that the clouds at large z are moving through a medium in which the gas pressure is comparable with that in the galactic plane. A tenuous gas at high kinetic temperature , in the range of 10^5 to 3 x 10^6 degrees, provides a simple explanation for the continued existence of absorbing clouds far from the galactic plane."
> (Spitzer, 1956)

There were also some presumptions about the possible velocity of these clouds. In the introduction by Wakker, van Woerden (1997) they explained:

> "In the late 1956, Oort suggested to one of us (HvW) that such corona might contain neutral hydrogen (HI) having high velocities, and that this gas might replenish the gas expanding away from the Galactic Center region."
> (Wakker, van Woerden, 1997).

Spitzer predicted in 1956 that the heat conduction from the corona would lead to a "transition layer surrounding the cloud" which suits the later observed two-phase structure of HVCs as described by Wolfire et al. in 1995. A few years

later the systematic search for the predicted clouds succeeded and E. Raimond made the first detections of HI at high velocities (Muller et al. 1963).

More than 50 years after Spitzer's first assumptions and although the possibilities both in observations and in numerical simulations increased dramatically since then, the origin of the high velocity clouds is still under discussion. The full knowledge of their origin, evolution and current place in space would have a large impact on many other fields of both galactic and extragalactic astronomy and cosmology. The existence, the morphological appearance, the physical parameters and the distances of these hydrogen clouds are, in the case they belong to the galactic environment, closely connected to the characteristics of this "interstellar galactic corona", the so called galactic halo. This halo, in turn, depends on the understanding of dark matter, which is one connection to the wide field of cosmology and its dark matter models. On the other hand, if the high velocity clouds are of extragalactic origin, like the remnant "building blocks" of the Local Group as Blitz et al. (1999) suggested, or possible candidates for the missing satellite problem (Klypin et al. 1999) they would be good probes for any cosmological simulation. In addition to the significance for the large scale picture of the universe, HVCs play an important role in the interstellar mass and energy budget, since in-falling gas can trigger local star formation.

> "However, an understanding of their internal physics, their origin, and their role in galactic evolution requires more information on distances and element abundances, which can be determined from absorption spectra of background probes."
> (Wakker et al. 1996)

In the last decades, many observations were made in different wavelength for several issues related to the topic of high velocity clouds. Spatial distribution, column densities, structures and radial velocities are measured in large radio surveys in the 21 cm line of neutral hydrogen. Depending on their distance, the gas clouds are likely to be exposed to the galactic or intergalactic ionization radiation, which leads to an amount of ionized hydrogen, measurable as the Hα flux. Various observations about their metallicities and a possible dust content are made. In chapter 2 the properties of HI clouds with high anomalous velocities, those of the large complexes distributed over a large area in the sky as well as those of the population of compact high velocity clouds are described. In chapter 3 different theories of possible origins are discussed. This thesis focus on an origin, where the high velocity clouds are tracers of the dark matter sub-haloes arising out of many cosmological simulations, like the millennium simulation (MPA Garching, Springel et al. 2005) based on the theory of the Λ-CDM model, which is explained in section 3.4. The simulations of this thesis are created with FLASH2.5, a hydrodynamic, adaptive mesh refinement code developed by the ASC / Alliance Center for Astrophysical Thermonuclear Flashes at the University of Chicago. The Code is described in chapter 4, the initial setup and the included processes in chapter 5 and the results can be found in chapter 6.

Chapter 2

Properties of HVCs

Beside the HI amount, the velocity of the gas cloud is the strongest criterion if these structures belongs to the ensemble of high-velocity clouds. For the classification of HVCs a lower limit in their velocity is needed to distinguish between high and intermediate velocity clouds. Due to differential rotation of the galactic plane a lower boundary value in dependence of the local standard of rest (v_{LSR}) or the galactic standard of rest velocity (v_{GSR}) would be ambiguous, because at low galactic latitudes co-rotating disk gas could be misinterpreted as high velocity clouds. A way to reduce the effect of differential rotation on the classification of HVCs is to use the deviation velocity v_{dev} as a boundary between intermediate and high velocity gas. The deviation velocity was defined by Wakker (1991) as the difference between the measured radial velocity of the cloud and the maximum velocity that can be explained by differential galactic rotation at the corresponding galactic longitude and latitude. Since the radial velocities of HVCs are either highly positive (cloud is moving away) or highly negative (cloud is moving towards the sun, in LSR frame, or the galaxy, in GSR frame), the deviation velocity for a neutral hydrogen cloud to be catalogued as high velocity cloud is $|v_{dev}| = 50..100\,km/s$, depending on the observation criteria of the different catalogues. For example in the all-sky catalog by de Heij et al. (2002), which is a combination of the data from the Leiden/Dwingeloo Survey and the HIPASS data a minimum deviation velocity of $|v_{dev}| = 70\,km\,s^{-1}$ was used, while Braun & Burton (1999) defined a lower limit with $|v_{dev}| = 50\,km\,s^{-1}$.

2.1 Observations

2.1.1 Neutral hydrogen

Hendrik van der Hulst predicted in 1944 a radio emission at a wavelength of 21.1 cm, which occurs due to a hyperfine transmission of ground-state hydrogen. Due to magnetic coupling between the electron and the proton of the neutral hydrogen atom, the energy of an atom with parallel spin, which means that the spin directions of the proton and electron spins are the same, is slightly higher than of an atom with anti-parallel spin, which means spins oriented in the opposite direction (see Fig. 2.2). The transition from parallel to anti-parallel

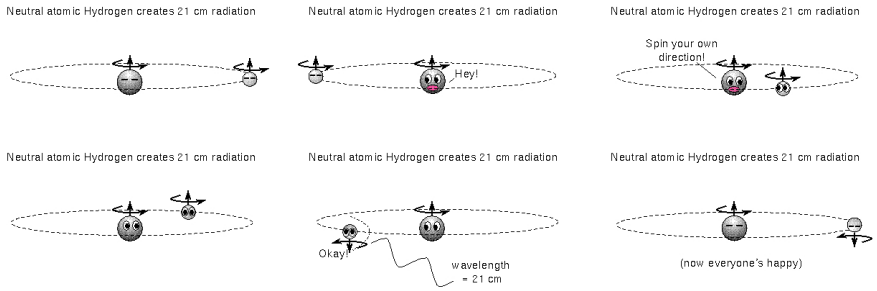

Figure 2.1: Sketch of HI hyperfine transmission that creates the 21 cm line of neutral hydrogen. The energy niveau of an electron and a proton with the same spin direction is slightly higher than of a configuration with opposite spin directions, which leads to an emission of a photon with an energy corresponding to a wavelength of 21 cm during the spin flip. Figures from http://www.pgie.ufrgs.br/portalead/oei/cgu/interm/interm.htm

configuration is highly forbidden with a probability of $2.9 \times 10^{-15}\, s^{-1}$. Nevertheless since the total numbers of neutral hydrogen in the interstellar medium is very high this line can be observed with radio telescopes in an accurate way, because of the very narrow line. In 1951, Ewen and Purcell first observed the line at 1420.495 MHz/sec ($\lambda = 21.1\, cm$) in the Galactic Radio Spectrum. This line can both be in emission and in absorption depending on the relation between the hydrogen spin temperature T_s and the temperature characterizing the background radiation in this part of the galactic radio spectrum T_{BG}. If $T_s < T_{BG}$ the hyperfine-structure line is in absorption, if $T_s = T_{BG}$ no line will be expected and for $T_s > T_{BG}$ the line will be in emission with the total intensity depending only on the difference between T_s and T_{BG}. Several radio surveys were made to get to know the distribution of these clouds by the 21 cm hydrogen line. For column densities larger than $7 \times 10^{17}\, cm^{-2}$ the sky-covering fraction for high-velocity clouds is derived by Murphy et al. (1995) with 40%. Observed optical and FUV absorption line measurements (Richter et al. 2005) show that even column densities with $N(HI) < 7 \times 10^{17}\, cm^{-2}$ exist. For this case HVCs are not single phenomena but wide-spread over large ranges in the sky. In Fig. 2.1.2 an Aitoff projection all sky map of the Galactic HVCs in Galactic coordinates is shown. They are arranged in large complexes, which are indicated in Fig. 2.1.2. The largest and best studied complexes are complex A, C, H, the Anti-center Cloud and the Magellanic Stream. Beside these large buildings there are also several small, well-defined and isolated signatures of high-velocity neutral hydrogen, which are called compact high-velocity clouds (CHVCs). See Section 2.3 for the spatial distribution of the neutral hydrogen gas in detail.

Calculate the column density out of the brightness temperature: In many publications the contour lines of HI observations are given with the brightness temperature T_B. If the brightness temperature of the signal is larger than those of the continuum, the column density N(H) can be derived using

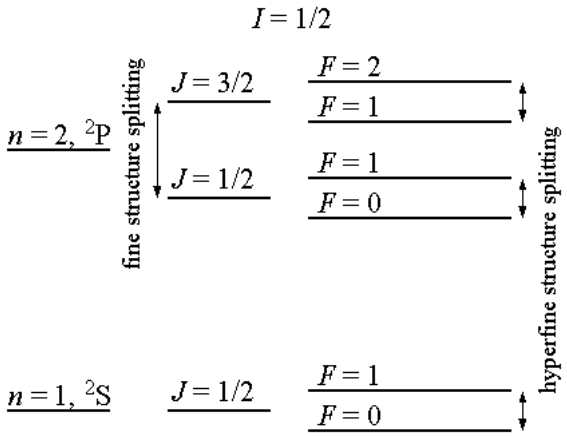

Figure 2.2: Scheme of the fine-structure and hyperfine-structure transmissions of hydrogen. The 21 cm line arises from the small energy difference between F=1 and F=0 of the ground-state (n=1). Figure from wikipedia.com

$$N(H) = 1.823 \times 10^{18} \int T_s \tau(\nu) d\nu \tag{2.1}$$

where T_s is the spin temperature, which refers to the kinetic temperature in most cases, and $\tau(\nu)$ is the optical depth as a function of the frequency ν. The optical depth of the 21 cm line with a Gaussian line profile is given by

$$\tau = 5.2 \times 10^{-19} \frac{N(H)}{T_s \Delta V} \tag{2.2}$$

where ΔV is the line FWHM in $km\,s^{-1}$. Accounting for hydrogen in emission only (no absorption), $T_0 = 0$ and $\tau(\nu) << 1$ the following relation by Dopita & Sutherland (2004) can be used:

$$T_B = T_s \tau(\nu) \tag{2.3}$$

$$T_B = T_s \cdot 5.2 \times 10^{-19} \cdot \frac{N(H)}{T_s \Delta V} \tag{2.4}$$

$$N(H) = \frac{T_B \Delta V}{5.2 \times 10^{-19}} \tag{2.5}$$

Brüns et al. (2000) observed the head-tail HVC 128-36-425 (see Fig. 2.3) with the following data:

$$T_B = [0.12 - 0.68] K \tag{2.6}$$

$$\Delta V = 174\,km\,s^{-1} \pm 7.5\,km\,s^{-1} \tag{2.7}$$

The column densities therefore reach from $2.275 \times 10^{20}\,cm^{-2} \pm 9.81 \times 10^{18}\,cm^{-2}$ at the core to $4.015 \times 10^{19}\,cm^{-2} \pm 1.73 \times 10^{18}\,cm^{-2}$ at the weakest contour line (see Fig. 2.3).

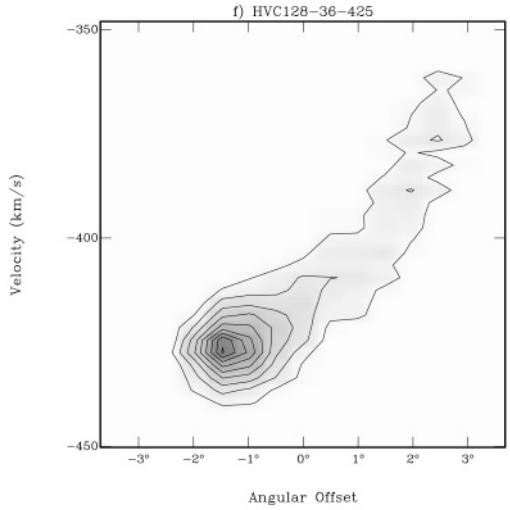

Figure 2.3: HVC128-36-425 as observed by Bruens et al. (2000): Gray-scale indicates T_B, the darker the colour the higher T_B. The contour lines start at $T_B = 0.12\,K$ in steps of $\Delta T_B = 0.08\,K$.

Deuterium Abundance: Deuterium (^2H) is an isotope of hydrogen, containing a proton and an electron as the most common hydrogen isotope, also called protium (^1H) and an additional neutron in the core. The ratio between deuterium and hydrogen (D/H) is a very important tracer for the chemical evolution of the observed material since there is no known production of a significant amount of deuterium beside the Big Bang nucleosynthesis (Burles et al. 2001). In cosmology, the nucleosynthesis of primordial elements just a few minutes after Big Bang is supposed to be the dominant production scenario of deuterium and other elements like the helium isotopes ^3He and ^4He, the Lithium isotopes ^6Li and ^7Li and the unstable isotopes tritium ^3H, ^7Be and ^8Be (Beryllium). Though deuterium is not produced in the recent universe it can be destroyed in stellar nucleosynthesis. The abundance of deuterium should therefore decrease with time. Sembach et al. (2004) presented the first detection of D I Lyman series absorption in the local universe in another location than the Galactic disk. They found atomic deuterium in the HVC Complex C, in some intermediate velocity clouds and in the Milky Way ISM using the Far Ultraviolet Spectroscopic Explorer (FUSE). For Complex C the emission towards the background source PG 1259+593 was measured. The line of sight passes through a dense hydrogen core of Complex C with a hydrogen column density, observed with the Westerbork Synthesis Radio Telescope (WSRT) interferometer map together with the single-dish data from the Effelsberg 100m radio telescope, of $N(HI) = (9.0 \pm 1.0) \times 10^{19}\,cm^{-2}$. The column density of deuterium is given by $N(DI) = (2.0 \pm 0.6) \times 10^{15}\,cm^{-2}$ and the oxygen column density with $N(OI) = 7.2 \pm 2.1) \times 10^{15}\,cm^{-2}$. These values lead to light-element abundance ratios of $D/H = (2.2 \pm 0.7) \times 10^{-5}$ and $O/H = (8.0 \pm 2.5) \times 10^{-5}$. The uncertainties are all 1σ errors. In comparison the deuterium abundance D/H in the local ISM is determined to be about $D/H \approx 1.5 \times 10^{-5}$ (Moos et al.

2002) and for sight lines in the Galactic disk but with distances of for example about 800 pc (HD 195965, Hoopes et al. 2003) $D/H = (0.85 \pm 0.34) \times 10^{-5}$ (2σ) and $d \approx 2200\,pc$ (HD 191877, Jenkins et al. 1999): $D/H = 0.78^{+0.52}_{-0.25} \times 10^{-5}$ (2σ). Although there are too few sight lines available yet for a statistical investigation, there seems to be a higher astration of deuterium in Complex C than in the Galactic disk even if a D/H ratio similar to the local ISM cannot be ruled out with the discussed measurements. This provides a support for the theory that the origin of Complex C is rather extragalactic than located in the Galactic disk, because an ejected disk gas would not show higher D/H than the remaining disk gas due to the lack of deuterium production mechanism.

2.1.2 Ionization of elements

The ionization of elements can be either due to ionizing radiation or by dynamical interactions with an ambient medium like the galactic halo or an intergalactic medium. An internal ionizing energy source in HVCs like stars have not been observed until now. Observations of $H\alpha$ in HVCs play an important role in the distance determination of the clouds. Models of the galactic ionizing radiation field can be compared with the observed $H\alpha$ emission. Even more, it is possible to rule out a Local Group membership (contrary to a galactic halo population) since the cosmic ionizing background is too low and no $H\alpha$ emission is expected for HVCs at a distance in the order of 1 Mpc. In addition there are complexes with quite narrow distance ranges, which can be used for a better understanding about the radiation escaping from the Galactic disk and additional ionizing processes in the halo. Putman et al. (2003) used both the Anglo-Australian Telescope and the William Herschel Telescope to measure $H\alpha$ emission in the large HVC complexes, including the Magellanic Stream, as well as in the CHVCs. They made several detections and non-detections, each in both CHVCs and HVCs. Within the group of HVCs Complex H shows the largest $H\alpha$ emission (EM = 3697 mR), the Smith Cloud (GCP) and several cores of complex L also very high emission (Complex L: EM = 263 .. 639 mR, Smith Cloud: EM = 360 and 450 mR) while in complex A (EM = 108 mR) and C (EM = 133 mR) only moderate $H\alpha$ fluxes can be observed. For the five CHVCs with $H\alpha$ emissions distance estimates between 1.1 and 27.8 kpc are made, while the six CHVCs, where no $H\alpha$ emission was found, either the distances are in the range of 50 kpc and more or the non-detection comes from a weaker ionization radiation at that place. This could be the case if some clouds lie above spiral arms or HII regions (as Complex L and the Smith Cloud are supposed to be) while others do not. The detection of $H\alpha$ in an unneglible fraction of CHVCs shows that the population of CHVCs is also settled in the Galactic Halo.

In addition also highly ionized ions, namely C IV (1548 Å), Si IV (1394 Å), N V (1238 Å) and O VI (1032 Å) are measured for three lines of sight towards Complex C with similar velocities and abundance relations of [C IV/O VI]= -0.31 .. -0.40, [Si IV /O VI] = -0.90 .. -0.93 and [N V/O VI] < -0.38 .. < -0.82 (Collins et al. 2007). This amount can not be explained by the galactic ionization field only, for a roughly limited distance for Complex C of d<25 kpc. Sembach et al. (2002) focused on HVCs with measured O VI since it is a very good tracer for dynamical interactions with hot gas at a temperature around $10^5 - 10^6$ K. They found O VI in the Magellanic Stream, in Complex

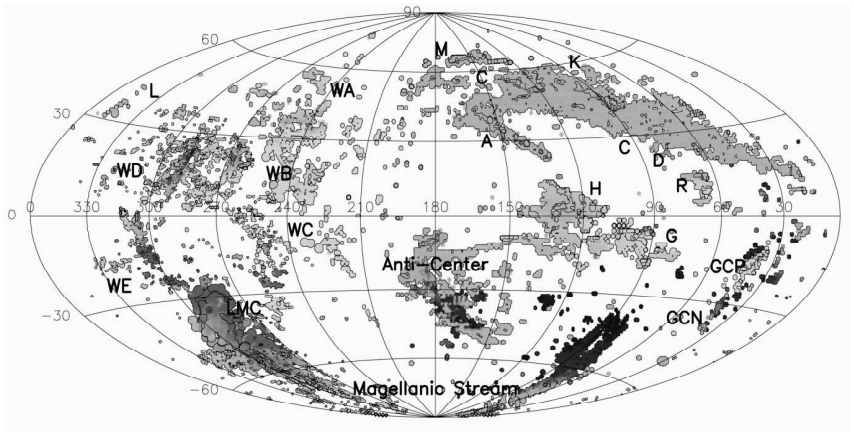

Figure 2.4: HI column densities $> 2 \times 10^{18}\, cm^{-2}$, based on the 21 cm data from Hulsbosch & Wakker (1988) and Morras et al (2000). Figure by Wakker (2004).

C and other HVCs and conclude that the quantity of highly ionized elements can not only be produced by photo-ionization but more likely with interactions of the cold or warm medium of the cloud with a hot surrounding medium like either the galactic halo gas or the Local Group medium with a density below $10^{-4}\, cm^{-2}$. Ganguly et al. (2006) found also large abundances of highly ionized gas which dominates the neutral gas with a ratio at least of 10:1 in the HVC in the direction of PG 1116+215 and explain that with almost the same scenario as above.

2.1.3 Metal abundances

For many larger complexes observations according to their metal abundance were made. One of the best studied complexes is Complex C, where recent, very accurate FUSE and Hubble Space Telescope (HST) measurements by Collins et al. (2007) are available. Since the angular extent of Complex C in the sky is huge (≈ 2000 deg^2) a lot UV bright quasars in the same direction can be used as background sources. The regions where the lines of sight pass the HVC have HI column densities from $10^{18.1}\, cm^{-2}$ to $10^{20.1}\, cm^{-2}$. While the oxygen abundance [OI/HI] reaches values of 0.09 to 0.29, the nitrogen abundance is significantly lower with $[N/H] = (0.01 - 0.07)$. Both the differences in the oxygen abundance over the whole complex and the lower nitrogen content relative to solar can be indicators for the origin and history of Complex C. Oxygen and other α-process elements are mainly produced by Type II supernovae (SNe) but the larger amount of nitrogen is produced by lower mass stars on the asymptotic giant branch (AGB). Comparing the oxygen and nitrogen abundances to those of solar, metal enriched gas by SNe should be more dominant in Complex C as in the solar neighborhood. The broad range of oxygen abundances is a hint for yet unclear mixing processes of low metallicity gas, probably primordial material with $Z = 0.1\, Z_\odot$ with SNe enriched gas, with an origin either in the galactic disc, which is ejected by a galactic fountain or expelled by LG dwarf galaxies.

The metallicity measurements of Complex M show a quite larger amount of enriched gas with a metallicity derived from Si II emission lines (Wakker 2000)

of 0.8 ± 0.3 solar, which together with an upper distance limit of 4 kpc are indicators for an origin in the Galactic disk.

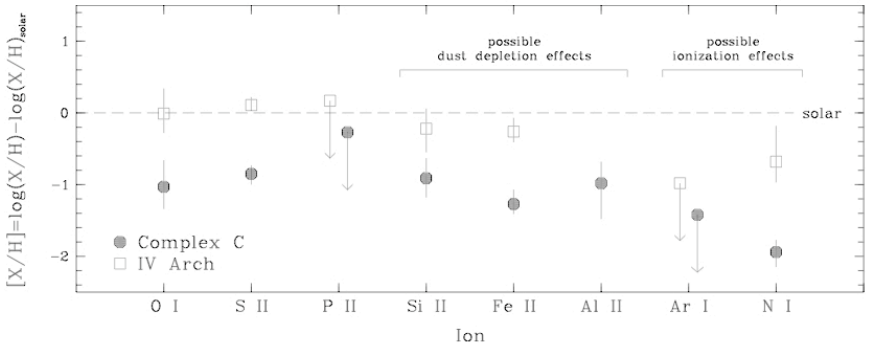

Figure 2.5: Overview of metals observed in Complex C. Figure by Richter et al. (2001).

While for the larger complexes, several metallicity measurements were made, it is very unlikely to find a suitable background source in the line of sight of a CHVC due to their very small angular extent. Sembach et al. (2002) found that the position on the sky of quasar Ton S210 is at the edge of CHVC 224.0-83.4-197 leading to the rare possibility for direct metallicity measurements. The comparisons were made between high spectral resolution observation at the Parkes 64m telescope for the hydrogen content and Far Ultraviolet Spectroscopic Explorer (FUSE) observations for OI (λ = 1039.230 Å), OVI (λ = 1031.926 Å), CII (λ = 1036.337 Å) and CIII (λ = 977.020 Å). Combining the OI and HI results the upper boundary of the oxygen abundance (O/H) is 2.5×10^{-4} for a 3σ confidence level. This correlates to a metallicity of < 0.46 solar if $(O/H)_{\odot} = 5.45 \times 10^{-4}$ (Holweger 2001). Since the quasar is not located in the center of the cloud but in the outer layers, the measurements are for hydrogen gas in its warm phase and the presence of ionized elements as CIII and OVI is explained by the ionized layer of the cloud.

2.1.4 Dust

Wakker & Boulanger (1986) looked for $100\,\mu m$ dust emission in HVCs using Infrared Astronomical Satellite (IRAS) data. They made several non-detections and inferred that the dust could either be cooler or the dust content is lower in HVCs than in low-velocity HI clouds. For the case that the dust is too cool they derived a lower distance limit of 11.5 kpc, where the Galactic radiation field is weak enough for these low dust temperatures. The Spitzer Space Telescope, launched in 2003 provides a much larger sensitivity and Miville-Deschenes et al. (2005) reported the first dust detection in Complex C. The temperature of the dust in Complex C $T = 10.7^{+0.9}_{-0.8}\,K$ $(1\,\sigma)$, is lower than in the local interstellar medium T=17.5 K, which is expected because of their larger distance to the Galactic plane. The dust-to-gas ratio, which should scale with metallicity assuming a standard metal depletion, should be proportional to the dust emissivity. Miville-Deschenes et al. (2005) derived the dust emissivity at $160\,\mu m$,

which is quite larger than solar. Together with former metallicity measurements of Complex C ($Z_C = 0.2 \pm 0.1\, Z_\odot$, Tripp et al. 2003) they conclude that the dust and for a fixed dust-to-gas ratio also the gas column density is more than 5 times larger than assumed. They suggest, that HVCs consist of some small, dense molecular clumps with a very low surface filling factor, embedded in a diffuse gas.

2.2 Multiphase structure

Observations using the Westerbork Synthesis Radio Telescope by Wakker and Schwarz (1991) (hereafter WS91) with 1' and $1\,kms^{-1}$ resolutions allowed a more detailed structure analysis. Fig. 2.6 shows the difference between the Westerbork (Fig. 2.6) and the Green Bank 300 ft telescope observations (9'.7 beam) by Giovanelli et al. (1973) (Fig. 2.6). Due to the measured temperatures and the derived pressure a two phase structure of some high-velocity clouds seems to be reasonable. The core temperature is generally between 30 and 300 K. The model of Wolfire et al. (1995) based on the observational indications, that some HVCs have a two-phase structure which is made up of a cold, dense core (T=30...300 K, n=10..100 cm^{-3}) and a warmer, dilute envelope analogical to the CNM (cold neutral medium) / WNM (warm neutral medium) in the galactic plane (McKee & Ostriker, 1977). Wolfire et al. (1995) have made former calculations about a multiphase equilibrium in the interstellar medium so that a coexistence of the CNM and the WNM in the disk is likely. It was assumed, that disk gas is heated by the photoelectric emission from small grains and PAHs (polycyclic aromatic hydrocarbon). Due to the far-ultraviolet radiation, supplied by OB stars, which is absorbed by dust grains, the radiation energy is converted to thermal energy with an efficiency of about 4% in the CNM and about 1% in the WNM (Wolfire et al. 1995). The advisement is, that there must be some range of height and/or pressure (P_{min} ... P_{max}) in which such a two-phase structure is stable. They assume that the clouds are embedded in a hot ionized medium (HIM) which is consistent with the observations of the galactic halo. There was a similar model by Ferrara & Field (1994). They wanted to determine the cloud's distance due to their H I emission, so they calculated the

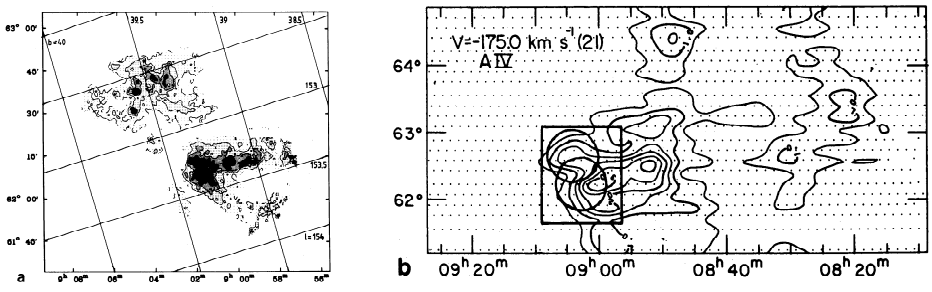

Figure 2.6: Left :WS91's figure 1a shows a column- density map of A IV at a resolution of $52'' \times 60''$. The contour levels are 10,70,130,190, and 250 $\times 10^{18}\, cm^{-2}$. A galactic-coordinate grid is overlaid. Right: WS91's figure 1b shows the A IV core as observed by Giovanelli et al. (1973).

thermal and ionization structure of clouds exposed to the extragalactic Lyman continuum radiation field and halo emission. A relation was found between the column density at which clouds start to develop cold neutral cores and the cloud size. The model of Wolfire et al. (1995) goes a bit further. They include X-ray heating, cosmic ray heating and photoelectric heating from small grains and PAHs. Kalberla et al. (2006) used the Leiden /Argentine/Bonn (LAB) HI line survey, which is a combination of the southern sky survey of the Instituto Argentino de Radioastronomia (IAR) and an improved version of the Leiden/Dwingeloo survey (LDS). They focus on the large complexes and found that an average of 20% of the HVC flux comes from cold gas in dense cores. Only in the Complexes EN, WA, WC, P, L, GCN and D no indications for a multiphase structure were found, which is more likely a problem of resolution than of extraordinary HVCs. DeHeij et al. (2002) observed the compact subpopulation with a cold phase flux of 4-16% of the total flux. Burton et al. (2001) used the Arecibo Sky Survey to observe ten CHVCs cataloged by Braun & Burton (1999). They found a two-phase structure in each of the observed cloud with an cold neutral core and a warmer envelope with an kinetic temperature of about $T_{kin} = 10^4\,K$. In this sample, the cores seemed to be kinematically separated from the warmer envelope, showing a velocity gradient consistent with rotation.

2.3 Spatial distribution

The most dominant line, where HVCs can be detected is the 21 cm line of neutral hydrogen. Several samplings were made to get to know the distribution of these clouds. In Fig. 2.1.2 the column density distribution of high velocity neutral hydrogen can be found. In addition, Fig. 2.3 provides also information about the velocities, ranging from high negative to high positive velocities with an asymmetric appearance. These large complexes are the best studied objects within the high velocity clouds. Due to their large angular extent, several direct distance and metallicity measurements are available. For more details about the large HVC complexes see Sec. 2.3.1. Not indicated in the all sky maps of the large complexes found in Fig. 2.3 are the subclass of compact high velocity clouds, their distribution and more details can be found in Sec. 2.3.3.

2.3.1 Large complexes

The large HVC complexes are well discovered and for many of them quite accurate distance estimates are available (see Table 2.3.1). They cover around 40% of the sky down to a resolution limit of $N_{HI} > 7 \times 10^{17}\,cm^{-2}$ (Murphy, Lockman, Savage, 1995). The direct distance measurement is possible with the help of stars with known distances in the line of sight of the gas cloud. The most common lines for this purpose are the Ca II K and the Na I D lines (Schwarz, Wakker, van Woerden, 1995). If they show any interstellar absorption by the HVC the maximum distance to the cloud is determined since the star has to be behind the cloud within the line of sight. On the other hand a lack of absorption leads to a lower distance limit setting the star in front of the cloud. While for the larger complexes several background sources are available, it is not very likely that a suitable star is exactly in the same direction as the CHVCs having

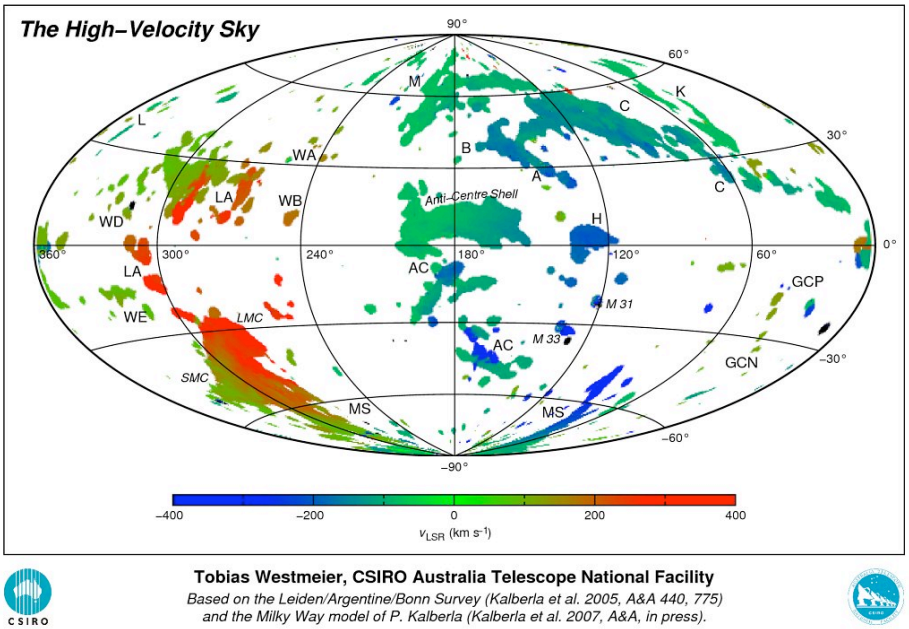

Figure 2.7: All Sky HVC map based on the Leiden/Argentine/Bonn Survey (Kalberla et al. 2005) where the large complexes are indicated with their available local standard of rest velocity information (colorcode). Figure from Tobias Westmeier.

a much smaller angular extent.

While Table 2.3.1 provides informations about distance measurements by several authors according to the large HVC complexes, Kalberla et al. (2006) summarized much more properties of HVC complexes, like the velocities, their core structure, the velocity dispersion and many more. Their circumstantial table can be found in Tab. 2.3.2.

Complex A is one of the most prominent and best studied complexes. Distance estimates by Wakker et al. (2001) settle Complex A in the galactic halo with d=4.4 to 9.9 kpc. Its metallicity is likely to be around $Z_A = 0.1\, Z_\odot$ with velocities ranging from -94 to $216.8\, km\, s^{-1}$ in the local standard of rest (Kalberla et al. 2006). The shape of Complex A is very filamentary with several high column density cores embedded in HI gas with lower column density.

Complex C with LSR velocities between -90 up to $-202.2\, km\, s^{-1}$ and an angular extent of more than 100 deg in Galactic longitude and more than 40° in Galactic latitude is also a very dominant HI complex (see Fig. 2.3.1 and 2.3.1). Similar to Complex A its distance limits are in the range of a few kilo-parsec ($10 \pm 2.5\, kpc$, Thom et al. 2008) and its metallicity is significantly lower than solar $Z_C = 0.1 - 0.2\, Z_\odot$.

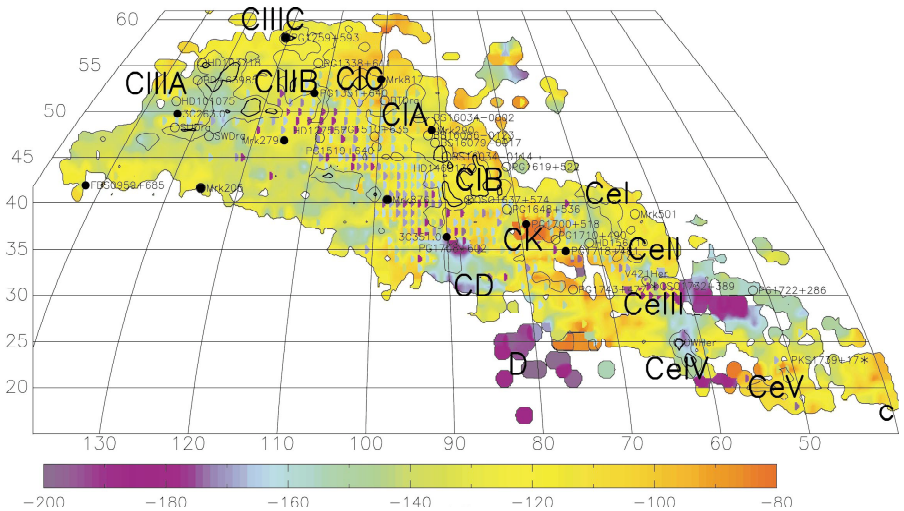

Figure 2.8: Map of HVC complex C, from Hulsbosch & Wakker(1988). Contours indicate brightness temperature levels of 0.05, 0.4 and 1.0 K. Colors indicate velocities, as identified by the wedge, relative to the local standard of rest in units of km/s. The half circles point at direction where two velocities are measured, its colour represents the velocity of the second component. Core names are also given, as are the positions of probe stars. Closed symbols refer to detections, open symbols to non-detection. Figure from Wakker (2001).

Complex H is an extraordinary HVC because of its low Galactic latitude. Lying in the Galactic plane with an angular extent of 25°, it provides a different distance estimate. Assuming the cloud lies in the disk with a galactocentric distance of less than 20 kpc and its measured velocity, the occurring ram pressure would provide a huge energy amount, which should be easily detectable. This leads to an distance estimate of $d > 50\,kpc$ (Blitz et al. 1999) or more recent $d = 33 \pm 9\,kpc$ (Lockman 2003)

The Magellanic Stream (MS) was first discovered in 1972 by Wannier & Wrixon and two years later connected to the Magellanic Clouds by Mathewson et al. (1974). Although it technically belongs to the group of high velocity clouds because of its atypical velocity and it HI emission, the Magellanic Stream is often ruled out of the HVC ensemble because its origin is well understood in contrast to the other HVCs. Nevertheless a reasonable theory about the origin of the HVCs has to include the Magellanic Stream. Although the relation to the Large Magellanic Cloud (LMC) and the Small Magellanic Cloud (SMC) is quite clear, the detailed formation of the MS is still under discussion. The two main theories are relating to either ram-pressure stripping due to a hot gas in the Galactic Halo or tidal disruption scenarios of the LMC and SMC gas.

Complex	Distance Range	Author
C	$10 \pm 2.5\,kpc$	Thom et al. (2008)
WB	$7.7 \pm 0.2\,kpc$ to $8.8^{+2.3}_{-1.3}\,kpc$	Thom et al. (2006)
A	4.4 to $9.9\,kpc$	Wakker (2001)
H	$33 \pm 9\,kpc$	Lockman (2003)
MS	$\approx 50\,kpc$	Kalberla (2006)
EP	$\approx 50\,kpc$	Kalberla (2006)
M	1.5 to $4.4\,kpc$	Danly et al. (1993)
K	0.7 to $6.8\,kpc$	Smoker et al. (2006)

Table 2.1: Overview of distance estimates for some HVC complexes.

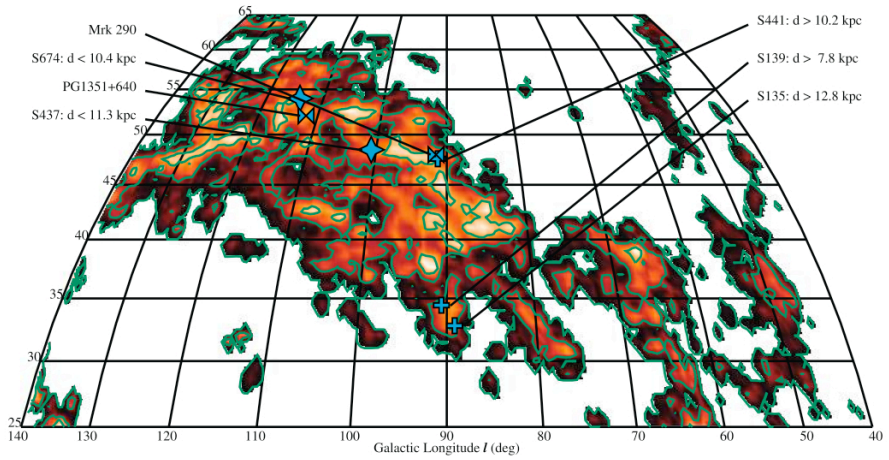

Figure 2.9: Location of SDSS stellar targets with respect to HI emission of Complex C. Contours are drawn at log N(HI) = 18.2, 19.2, and 19.7 cm^{-2}. Figure from Thom et al. (2008)

2.3.2 Head Tail HVCs associated with the large complexes:

Brüns et al. (2000) presented observational results about high velocity clouds using the Leiden Dwingeloo HI Survey, The found 252 clouds with column densities larger than $10^{19}\,cm^{-2}$. About 20% of their sample HVCs show a head-tail structure and are called HT-HVC ($\#HT-HVCs = 45$, see examples in Fig. 2.10). They claim that the majority of the cataloged HT-HVCs belong to the large HVC complexes (see Fig. 2.11). The issue to solve is an explanation for the fraction of clouds showing a HT-structure within every complex. Statistical investigations by Brüns et al. (2000) show, that the fraction of HT-HVC over the total number of HVCs in the large complexes can be fitted with:

$$\frac{\#HTs}{\#HVCs} = (0.0317 \pm 0.0028)\frac{N(HI)}{[10^{19}\,cm^{-2}]} + (0.017 \pm 0.012) \qquad (2.8)$$

while no correlation between $(\#HTs)/(\#HVCs)$ and their local standard of rest velocity v_{LSR} or their galactic longitude or latitude was found. Assuming

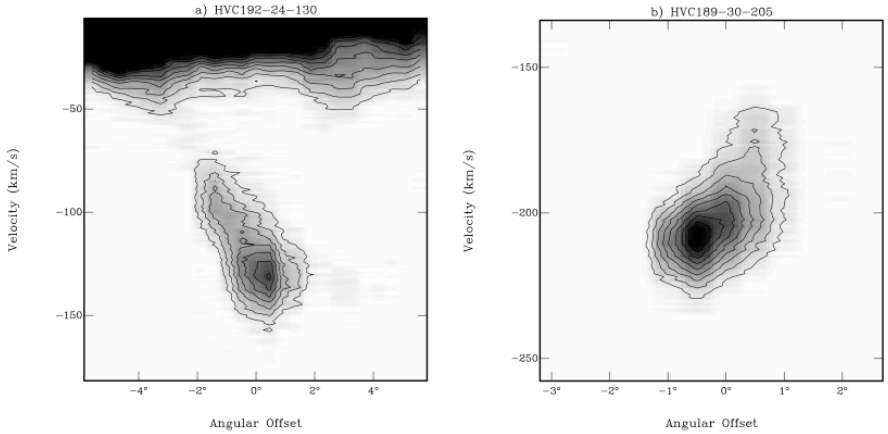

Figure 2.10: Position velocity diagram of HT-HVCs by Brüns et al. (2000). The contour lines indicate T_B and start in both panels at $T_B = 0.21\,K(3\,\sigma)$ in steps of $\Delta T_B = 0.14\,K(2\,\sigma)$.

that ram pressure is responsible for the observed feature of HT structure and the tail is the gas recently stripped off the cloud due to a surrounding halo material, all clouds within one complex and therefore similar heights above the galactic plane should show a head-tail structure. Kalberla et al. (1998) found evidence in the LDS for an diffuse neutral hydrogen halo with velocity dispersions of $60(\pm 3)\,km\,s^{-1}$ and a column density of $N_{HI} = (1.4 \pm 0.1) \times 10^{19}\,cm^{-2}$. The conclude that the galactic halo consist of a multiphase medium with a neutral halo medium (NHM) with temperatures of $T < 10^4\,K$, transition regions already observed as highly ionized atom with temperatures of $T \approx 10^5\,K$ (Savage et al. 1997) and a hot plasma that explains the soft X-ray background (Kerp, 1994) with a temperature of $T \approx 10^{6.3}\,K$. A tracer of the halo regions with low temperatures and therefore larger densities could be found in the distribution of HT-HVCs.

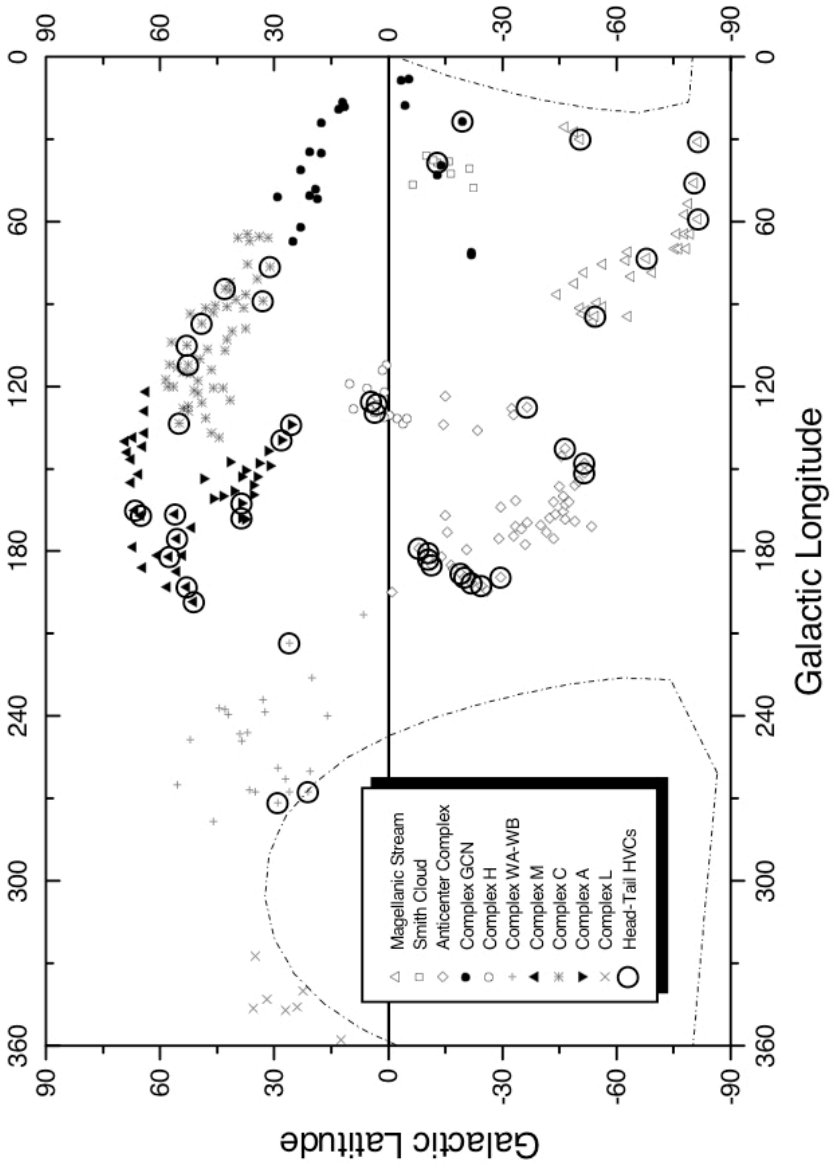

Figure 2.11: HT-HVC in the large complexes. The average fraction of HVCs showing a head-tail structure is about 20% in every complex. Only in complex L no HT-HVC was found. Figure from Brüns et al. (2000).

Table 2.2: Table by Kalberla et al. (2006): Properties of HVC complexes. The columns are: name, longitude, latitude, velocity range, number of positions observed n_{pos} , fraction of positions with cores: f_n, fraction of column density in cores relative to the total column density: f_N, fraction of column density in cores at intermediate velocities: f_{NIV}, first moment of the column density weighted distribution of velocity dispersions: $< \sigma_{NH} >$, first moment of the distribution of velocity shifts $v_i - v_1$ for $M < 1$: $S(M < 1)$, the same for $M < 2.35$: $S(M < 2.35)$, and second moment of the distribution of velocity shifts $v_i - v_1$ for $M < 2.35$: ΔS

Name	Gal. long. [deg]	Gal. lat. [deg]	Vel. range [km/s] Â	n_{pos}	f_n	f_N	f_{NIV}	$< \sigma_{NH} >$ [km/s]	S($M < 1$) [km/s]	S($M < 2.35$) [km/s]	ΔS [km/s]
all HVCs			> |90|	17336	0.238	0.208	0.207	11.8	-1.5	0.5	16.3
all –OA			> |90|	10139	0.111	0.157	0.120	11.7	-0.3	5.8	20.1
OA	48.0 : 190.0	-5.5 : 35.0	-168.6 : -90.	7197	0.416	0.229	0.226	11.8	-1.8	-0.8	14.8
A	130.0 : 172.8	22.0 : 49.0	-216.8 : -94.0	727	0.129	0.114	0.003	11.1	-3.7	-7.5	12.6
C	40.5 : 147.6	17.5 : 61.0	-202.2 : -90.	2646	0.061	0.061	0.015	11.2	-1.3	1.2	18.3
H	109.0 : 152.5	-16.0 : 13.5	-227.8 : -90.	1284	0.255	0.401	0.208	11.3	-0.6	16.3	21.9
H(-120)			-227.8 : -120.	1199	0.169	0.154	0.378	12.0	-4.5	4.4	20.1
M	129.0 : 198.1	47.5 : 69.0	-128.0 : -90.	277	0.058	0.058	0.050	10.3	-4.2	-7.3	9.7
MS+	281.9 : 333.4	-84.5 : -61.	50. : 200.8	150	0.380	0.270	0.000	13.4	-2.7	-4.4	19.1
MS+W	269.4 : 333.4	-84.5 : -22.5	50. : 361.6	1109	0.548	0.563	0.000	13.3	-1.6	-1.1	22.6
MS–	11.4 : 356.2	-85.0 : -39.0	-405.9 : -50.	668	0.075	0.110	0.000	13.7	-11.7	-8.6	22.8
EP	244.0 : 312.5	-27.0 : 28.0	170. : 317.4	290	0.238	0.135	0.002	10.6	0.9	1.7	14.8
ACHV	139.3 : 197.0	-52.0 : -6.0	-167.0 : -90.	853	0.036	0.036	0.006	12.1	1.6	-1.7	19.8
ACVHV	154.7 : 191.5	-54.0 : -7.0	-337.8 : -130.5	646	0.048	0.064	0.000	11.6	-14.1	-1.6	23.9
WB	224.5 : 268.8	0.5 : 45.5	90. : 169.6	599	0.057	0.041	0.119	12.6	5.5	-0.9	20.7
WD	260.0 : 313.0	8.0 : 20.0	90. : 181.9	297	0.306	0.120	0.083	12.1	4.4	5.5	18.5
WE	291.5: 324.5	-25.5 :-8.5	90. : 135.8	85	0.176	0.111	0.084	14.3	1.3	-0.7	14.2
R	62.0 : 73.5	5.5 :15	-156.3 : -100.3	142	0.190	0.096	0.325	11.6	-2.7	1.6	15.0
G	79.0 : 121.5	-19.0 : -1.0	-189.9 : -90.	521	0.190	0.138	0.298	12.2	0.8	1.8	16.5
GCP	34.5 :64.0	-41.5 : -9.5	90. : 137.0	153	0.327	0.123	0.082	11.6	2.3	6.3	12.6
EN	29.0 : 187.5	-59.5 : 33.5	-445.4 : -220.	481	0.017	0.015	0.000	11.1	2.9	-7.0	15.4
WA	231.5 : 273.0	23.0 : 45.0	100. : 196.9	230	0.039	0.007	0.001	10.1	-10.4	-0.6	18.3
WC	208.5 : 259.0	-33.0 : 3.5	90. : 212.7	156	0.071	0.028	0.433	13.4	7.2	-5.3	16.5
P	107.0 : 132.5	-39.0 : -30.0	-429.4 : -320.4	67	0.060	0.048	0.000	8.5	3.0	5.1	9.4
L	340.5 : 348.5	31.0 : 41.5	-156.0 : -90.	30	-	-	-	12.3	-	-	-
GCN	0.5 : 49.5	-40.0 : 10.0	-334.6 : -177.0	125	-	-	-	9.3	-	-	-
D	81.5 : 84.5	24.0 : 25.5	-199.6 : -15.4	6	-	-	-	8.4	-	-	-

2.3.3 Compact High Velocity Clouds

Braun & Burton (1999) used the Leiden Dwingeloo Survey (LDS) database and searched for a more compact and isolated sub-population among the high velocity clouds, called compact high velocity clouds (CHVCs). They are spatially and kinematically distinct from Galactic HI emission, their velocity deviates at least $50\,kms^{-1}$ ($60\,kms^{-1}$ in Putman et al. 2002) from the velocity explained due to differential rotation at the given coordinates. The half power contour (25% peak column density contour, Putman et al. 2002) of each CHVC has to encircle an area less than 4 square degrees, as a criteria for its compactness while the isolation criteria is fulfilled by the condition that it is not connected to any larger complex. A sufficient high column density contrast (more than 3 σ above the local noise floor) is required to exclude low contrast local maxima of filamentary, more extended features, or high column densities arising from line-of-sight overlap. Analogous to the LDS, Putman et al. (2002) used the HI Parkes All Sky Survey (HIPASS) data to find the CHVCs in the Southern Hemisphere.

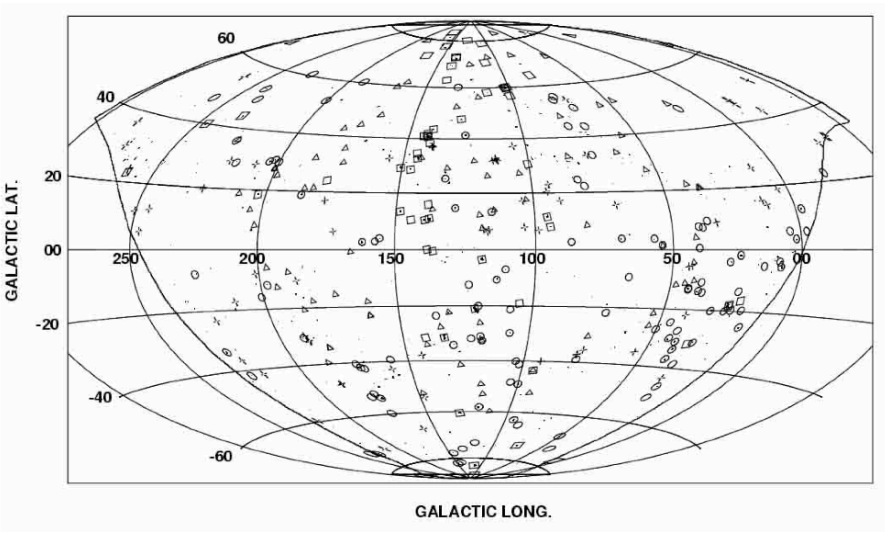

Figure 2.12: CHVC distribution from the LDS. Indicated are 59 cataloged external galaxies (squares), 116 CHVCs (open circles), 72 CHVC candidates which were not confirmed in subsequent observations (crosses), 84 CHVC candidates for which no confirming observations have yet been obtained (triangles). The solid line is the nominal $\delta = 30°$ cut-off of the LDS. Figure from de Heij et al. (2002).

Compact HVCs with head-tail structure by means of HVC 125+41-207 HVC 125+41-207 was placed at extragalactic distance by Braun & Burton (2000). Brüns et al. (2001) used Effelsberg HI 21-cm line data. The lowest contour line indicates a column density of $3 \times 10^{18}\,cm^{-2}$. This corresponds to a $3\,\sigma$ significance level. The peak column density in this map is $1.2 \times 10^{20}\,cm^{-2}$. As observed in several HVCs before (e.g. Wolfire et al. 1995), HVC 125+41-207

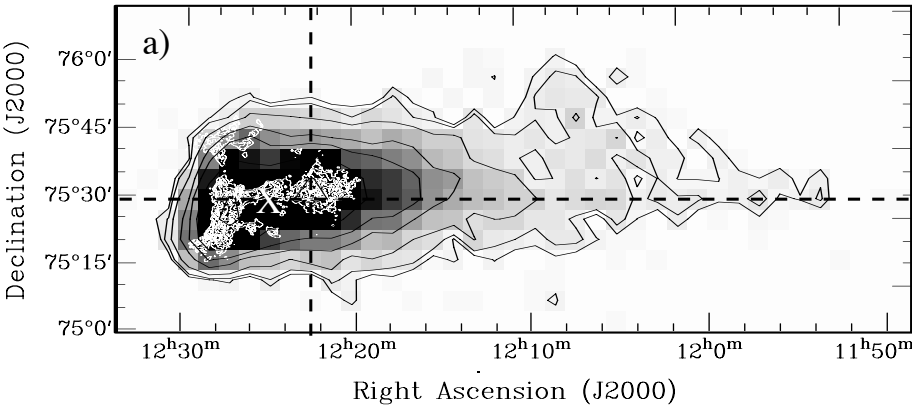

Figure 2.13: Column density distribution of HVC 125+41-207. The white contour level in the core of the cloud are Westerbork data from Braun & Burton 2000, from $5 \cdot 10^{19}\,cm^{-2}$ in steps of $5 \cdot 10^{19}\,cm^{-2}$ while the black contour lines refer to Effelsberg observation by Brüns et al. (2001) at 3, 5, 10, 20, 30, 50, 100 $\cdot 10^{18}\,cm^{-2}$. Figure from Brüns et al. (2001)

shows a two-phase structure with a low and high velocity dispersion for column densities larger than $2 \times 10^{19}\,cm^{-2}$. This cloud consists of two cores with local maxima in the column density, both at about $8 \times 10^{19}\,cm^{-2}$, of the cold gas-phase (Doppler temperature upper limit $T_D < 540K$ for the Westerbork data (Braun & Burton 2000) $T_D = 85\,K$ for the compact cores, due to better resolution) and a highly asymmetric, shifted envelope with an exponentially decreasing tail of warm hydrogen gas ($T_D < 7000\,K$, see Fig. 2.13 and 2.14). Integrated over the whole extent of the clouds the total HI mass scales with the squared distance and is $M_{HI} = 2.4 \times 10^6 (d/200\,kpc)^2\,M_\odot$, where the warm gas phase accounts for 52% of the total HI mass, including the 12.5% of the total HI mass located in the tail. Brüns et al. 2001 derived the total space velocity of the cloud with $v_{total} = 225 \pm 18\,km\,s^{-1}$ due to the effect that the angle between the HVC velocity vector and the line of sight changes over the extent of the cloud. In Fig. 2.3.3 the column density, the FWHM and the galactic standard of rest velocity v_{GSR} along a slice parallel and perpendicular to the direction of the tail is shown. Notice that the galactic standard of rest velocity of the cold component is around $75\,km\,s^{-1}$, with a gradient explained by the extent of the cloud (angle between LOS and the direction of cloud motion varies over the extent of the cloud) while the warmer gas phase is decelerated and for relative positions larger than 0.9° this deceleration increases rapidly. A possible explanation for this feature is the existence of an additional gravitational potential. The increase of the deceleration in this assumption would be located around the edge of the DM halo.

2.3.4 Extragalactic HVCs

Westmeier et al. (2005) presented high resolution Westerbork HI observations for 16 HVCs around M31 and M33, which were found within a Green Bank

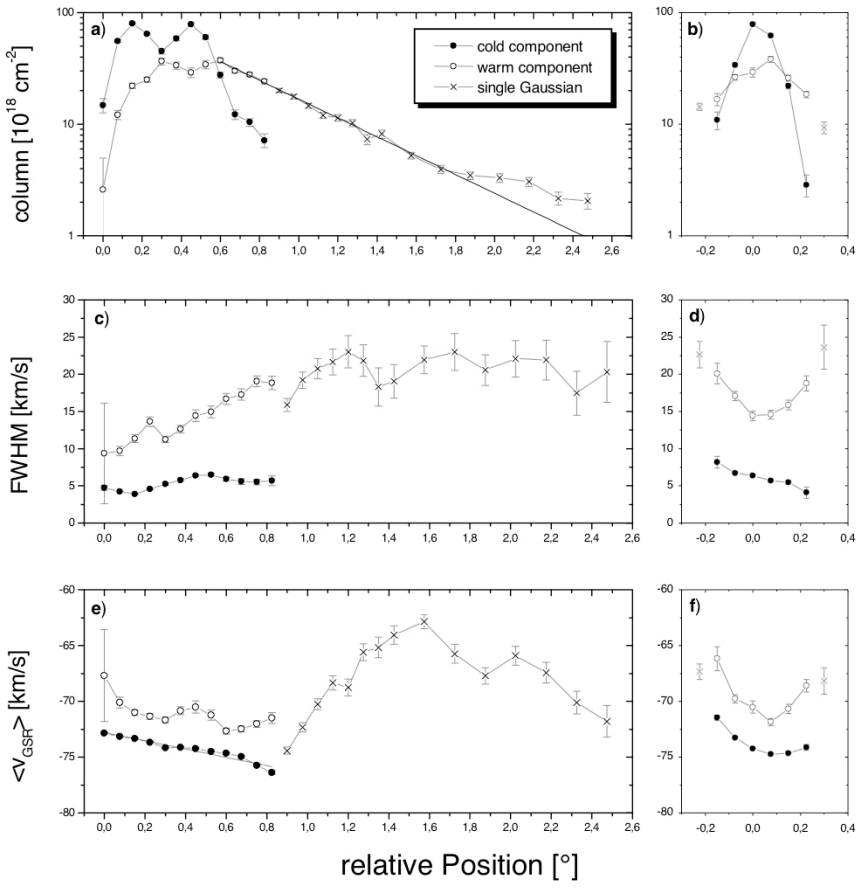

Figure 2.14: Column density, FWHM and v_{GSR} 1D cuts of HVC 125+41-207 as indicated in Fig. 2.13 parallel to the elongation (left panels) and perpendicular to the head-tail structure (right panels). Figure from Brüns et al. (2001).

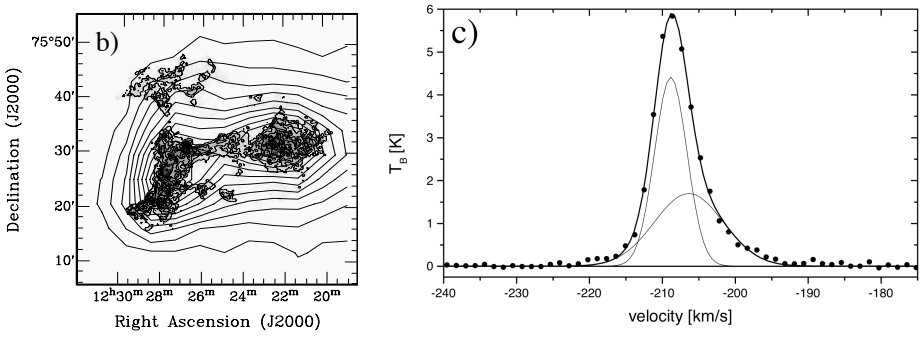

Figure 2.15: Left: Column density distribution of HVC 125+41-207. Density contours of the Westerbork data as in Fig. 2.13 while the contour lines of the Effelsberg data start at $5 \cdot 10^{18}\,cm^{-2}$ in steps of $10^{19}\,cm^{-2}$. Right: Two Gaussian fits representing a cold and a warm gas phase component, where the cold gas is at a higher radial velocity than the cold gas. Figures from Brüns et al. (2001).

telescope survey of $7° \times 7°$ around M31 in the 21 cm line of neutral hydrogen by Thilker et al. (2004). As observed for high velocity HI clouds around the Milky Way, the population around M31 and M33 separates in larger complexes, which are partly overlapping with the stellar stream found by Ibata et al. (2001) and isolated, more compact clouds. Remarkably no additional CHVC down to the HI mass limit of $6 \times 10^4\, M_\odot$ was found with the Effelsberg telescope (Westmeier 2005) up to a projected distance of 130 kpc from M31. Every CHVC found by Westmeier (2005) shows an elongation (see Fig. 2.16). The typical angular extent for these clearly extragalactic HVCs are in the range of 10". Assuming a distance of 780 kpc to M31 and 800 kpc to M33 the physical diameter of the clouds are between 0.43 kpc and 2.6 kpc with a mean of (1.04 ± 0.52) kpc. The HI masses vary from $0.2 \times 10^5\, M_\odot$ to $6.0 \times 10^5\, M_\odot$ with a mean of $(3.0 \times 10^5 \pm 1.9 \times 10^5)\, M_\odot$. Based on the derived physical diameter and HI masses an average particle density for each cloud can be easily calculated, assuming a homogenous density distribution. The particle densities lie between $2 \times 10^{-3}\, cm^{-3}$ and $1.09 \times 10^{-1}\, cm^{-3}$ with a mean for all M31 clouds of $(3.2 \pm 3.0) \times 10^{-2}\, cm^{-3}$. For five HVCs a lower limit for the dynamical mass was derived, giving an indication for an amount of ionized hydrogen and other elements or a large fraction of dark matter. In the following table the five clouds with derived dynamical masses are listed. The fraction of neutral hydrogen to the dynamical mass of the clouds is between 0.6% and 11.4% as upper boundaries. If most of the baryons are in neutral hydrogen, which is supposed to be for HVCs the dark matter amount would be at least 1 or 2 orders of magnitude above the HI mass.

HVC Nr. (Westmeier et al. 2005)	$M_{HI}\ [M_\odot]$	$M_{dyn}\ [M_\odot]$	M_{HI}/M_{dyn}
M31 HVC 1	5.2×10^5	$> 86 \times 10^5$	< 0.061
M31 HVC 2	5.0×10^5	$> 44 \times 10^5$	< 0.114
M31 HVC 6	0.6×10^5	$> 19 \times 10^5$	< 0.032
M31 HVC 8	2.1×10^5	$> 730 \times 10^5$	< 0.003
M31 HVC 10	5.0×10^5	$> 810 \times 10^5$	< 0.006

The clouds M31 HVC 2-12 are very likely connected to the stellar stream and therefore a tidal origin is evident as for M31 HVC 13, which is located only half a degree south of NGC 205 and fits also in the radial velocity. The

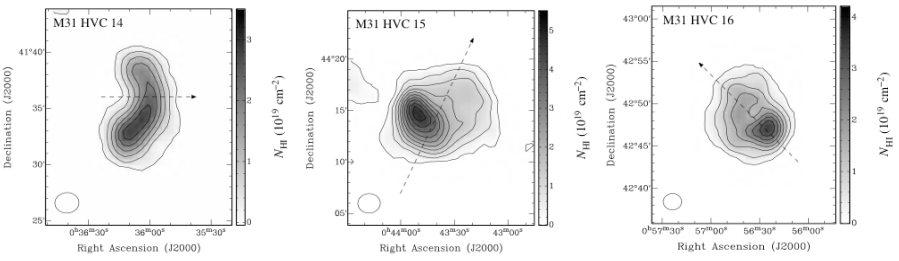

Figure 2.16: HI column density map of hydrogen clouds around M31(M31 HVC 14 - 16, from left to right). Each panel shows the right ascension, velocity (v_{LSR}) slice at a given declination (at the top of each figure). The contours represent T_B in units of mK. Figures from Westmeier et al. (2005).

other clouds M31 HVC 1 and M31 HVC 14-16 have no stellar counterpart and are both in position and in velocity separated from the stellar stream and any known dwarf galaxy associated with M31. It seem that the M31 HVCs can be divided into two groups regarding of their origin. The first group would emerge from tidal stripping of gas during close encounters, while the other group could be an additional evidence for the theory of gas clouds associated with dark matter halos as remnants of the hierarchical process of galaxy formation (Klypin et al. 1999, Moore et al. 1999). These dark matter halos are predicted in several numerical simulations. Kravtsov et al. 2004 simulated the evolution of M31 and found only 2-5 dark matter halos without any internal star formation within 50 kpc from M31, having gas masses of more than $M_{Gas} = 10^6 M_{odot}$. This simulation is in good agreement with the 4 compact high velocity clouds observed around 31.

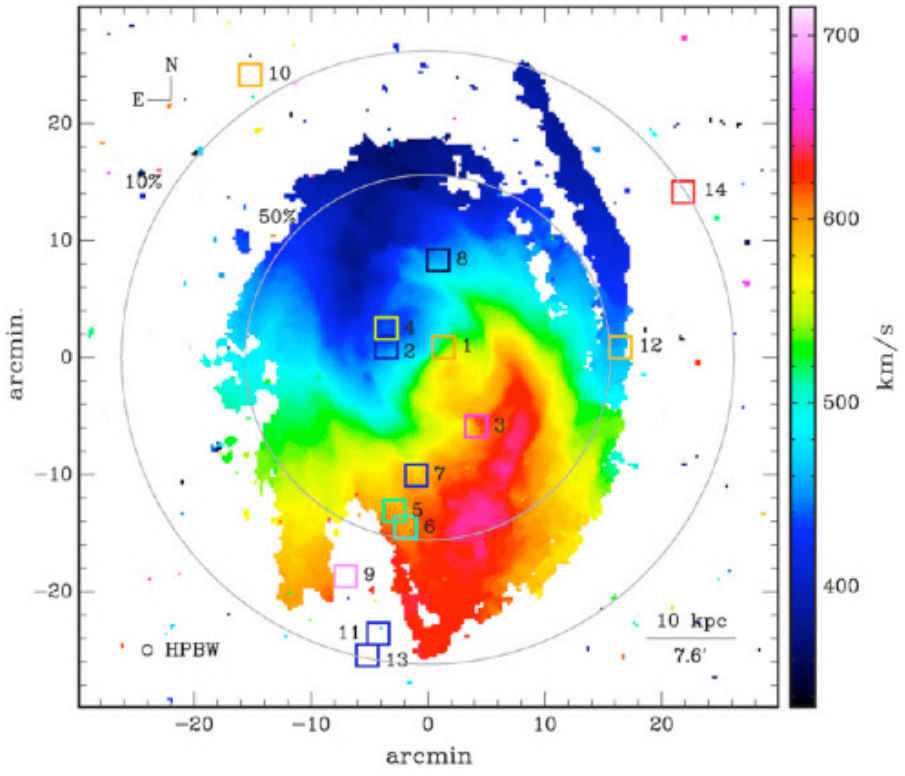

Figure 2.17: The HI distribution of M83 with the locations of the anomalous velocity clouds (AVC) detected by Miller et al. (2009) indicated. The shapes of the AVCs are related to their projected spatial extent down to 1σ in HI column density ($5 \times 10^1 8\, cm^{-2}$). The column density is color coded in units of $10^{20}\, cm^{-2}$. Figure from Miller et al. (2009).

Miller et al. 2009 found 14 HI clouds with anomalous velocities around M83, where only eight of them (AVC 1-8) are considered to be real detections with masses between $6 \times 10^5\, M_\odot$ to $1.5 \times 10^7\, M_\odot$ (see Fig. 2.17). In addition to the clouds they also observed a thick HI layer, which is rotating slower than the

old stellar disk. They proposed that the HI features origin partly from galactic fountains (the thick HI disk and some HI clouds associated with the spiral arms) and from tidal effects which should be responsible for the off-disk cloud production. Due to the large distance of about 4.5 Mpc the spatial resolution for HVC observations around M83 is more coarse than for the HVC observations of M31 and it is therefore very likely that only the more massive end of the HVC ensemble around M83 could be observed. Boomsma et al. (2008) investigated the HI distribution in the spiral galaxy NGC 6946 with a distance of 6 Mpc. They found 121 HI holes, having sizes up to 3 kpc in diameter and widespread, clumpy high velocity hydrogen and conclude that most of the high velocity gas come from a galactic fountain, related to the numerous HI holes.

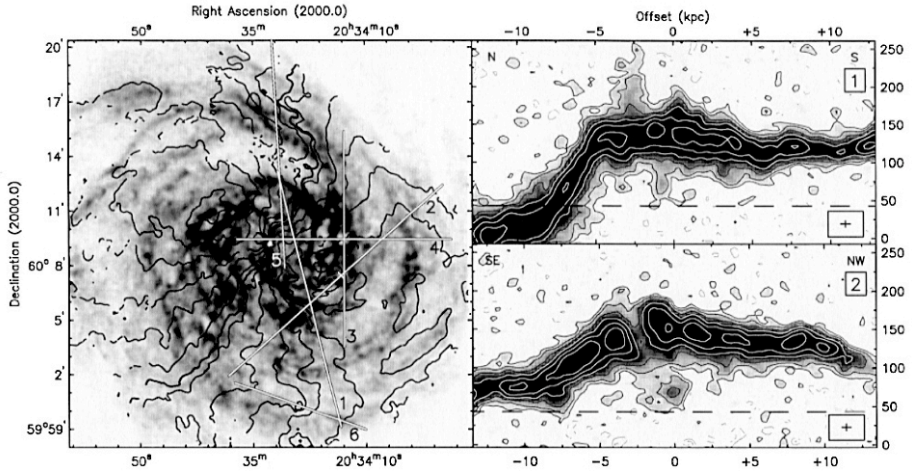

Figure 2.18: Left: HI map of the spiral galaxy NGC 6946. The black solid lines show the velocity field, while the white solid lines indicate the locations for the position-velocity cuts shown in the right panels. For position-velocity plots 3 to 6 see Fig. 12 of Boomsma et al. (2008). Right: Position-velocity plots: spatial offset [kpc] vs. heliocentric velocity [km s^{-1}] . Contours are at -0.75, -0.4, 0.4 ($1.5\,\sigma$), 0.75, 1.5, 3, 6, 12, and 24 mJy beam $^{-1}$. The cross in the lower left corner of the right panels show the resolution (22"). The dashed line is the systematic velocity of NGC 6946. Figure from Boomsma et al. (2008).

Search for extragalactic CHVCs in galaxy groups Pisano et al. (2004) used the Australia Telescope National Facility Parkes Telescope and Compact Array to look for HI clouds in galaxy groups similar to the Local Group. The non-detection of HI without any optical counterpart in the galaxy groups qualitatively similar to the Local Group, namely LGG 93, LGG 180 and LGG 478 down to a detection limit of $10^7\,M_\odot$. This sensitivity limit would be sufficient for a galaxy group origin as proposed by Blitz et al. (1999), with HI masses of $2 \times 10^7\,M_\odot$ but no detection would be expected for circumgalactic clouds with HI masses of $10^5\,M_\odot$ to $10^6\,M_\odot$. Therefore every non-detection in LG analogues is a validation for the theory of a circumgalactic distribution of the HVCs visible around the MW Galaxy.

Chapter 3

Origin

The origin of the high velocity clouds is still under discussion. The different theories are not hardly distinguishable through small details but varying on scales of several orders of magnitude. Beginning on stellar scales from the theory of a galactic fountains driven by multiple supernova explosions (see Sec. 3.1) over intermediate scales in the range of dwarf galaxies (see Sec. 3.2) to massive primordial dark matter halos as relics of the Local Group formation (see Sec. 3.2). The most obvious difference in these theories is the distance to the HVCs but also other observed quantities like metallicity and kinematics can help to either rule out or verify a theory. The challenge for a theory that fully explains the origin and evolution of high velocity clouds is to explain all varieties of neutral gas clouds, the wide-spread complexes, as well as the compact and isolated clouds with an angular extent of less than 1°. Although the Magellanic Stream holds an exceptionally position within the ensemble of high velocity clouds because of its obvious connection to the Magellanic Clouds, an over-all theory of HVCs should also be able to explain the MS.

Scenario	Distance [kpc]	$\lvert v_{dev}\rvert$ $[kms{-}1]$	Size [kpc]	M_{cloud} $[M_\odot]$	Z $[Z_\odot]$
GM in-fall	< 3	< 150	< 1	$< 10^4$	0.1–0.3
Galactic fountain	< 10	< 150	< 1	$10^4 - 10^5$	≥ 1
companion stripping	5–100	< 300	≈ 1	$10^5 - 10^6$	0.1–1
circumgalactic warm clouds	≈ 150	< 300	≈ 1	$10^6 - 10^7$	0.1–0.3
circumgalactic DM halos	≈ 150	< 300	≈ 1	$10^6 - 10^7$	0.1–0.3
Local Group DM halos	≈ 750	< 300	1–10	10^8	0.1–0.3

Table 3.1: Predictions of HVC Production Scenarios by Miller et al. (2009): Sizes and masses shown are typical values based on the median observed parameters of the HVC ensemble. Masses for the first three scenarios assume HI is the primary constituent of the cloud, while the others assume a neutral gas fraction of 0.1 (warm clouds) or HI to dark matter ratio of 0.1 (dark matter halos). Velocities for the Galactic fountain and IGM in-fall models assumes an adiabatic corona of fully ionized gas with $T \approx 10^6$ K.

In the table above (Miller et al. 2009) a nice overview of the different theories

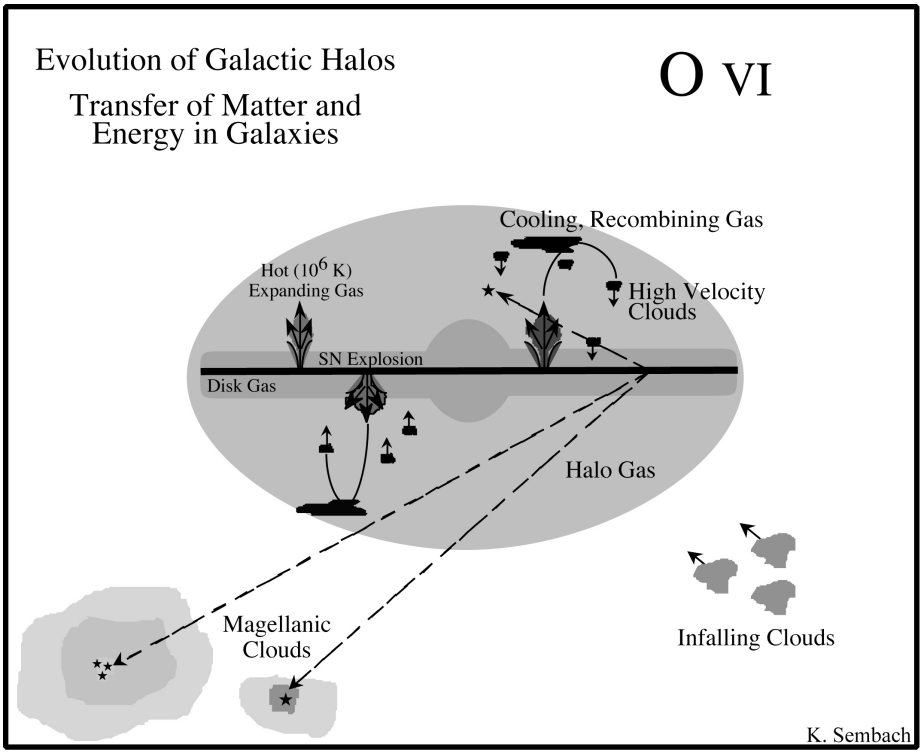

Figure 3.1: Schematic view of several development scenarios of high velocity clouds by Sembach. Indicated are clouds originating from multiple supernova explosions in a narrow range of place and time, the Magellanic Clouds the birthplace for the Magellanic Stream and some in-falling extragalactic gas clouds.

correlated with physical quantities can be found which are discussed in more detail in the following sections.

3.1 Galactic origin

Recent direct distance measurement for the large complexes settle at least the subclass of wide-spread high velocity cloud complexes in the galactic halo with distances of a few kpc for complex A, C, WB, M and K (see Sec. 2.3.1), which could be an indicator for a galactic origin. Shapiro & Field (1976) investigated a hot gas phase ($T = 10^6\,K$) additional to the, at that time, conventional two-phase model in the interstellar medium. They assumed a steady state model and looked for an efficient way to cool the hot gas, since it is reheated on a time-scale of approximately 10^6 yrs by supernova remnant shock waves in the disk. Since neither radiative cooling nor thermal conduction into cold gas is sufficient they look in more detail on the effect of convection. The hot gas will stream through the cool disk gas in the galactic halo, form a corona in hydrostatic equilibrium and subsequently cools and condenses at heights of approximately 1 kpc and fall back on ballistic orbits, with velocities of $\approx 100\,km\,s^{-1}$. These cool, neutral,

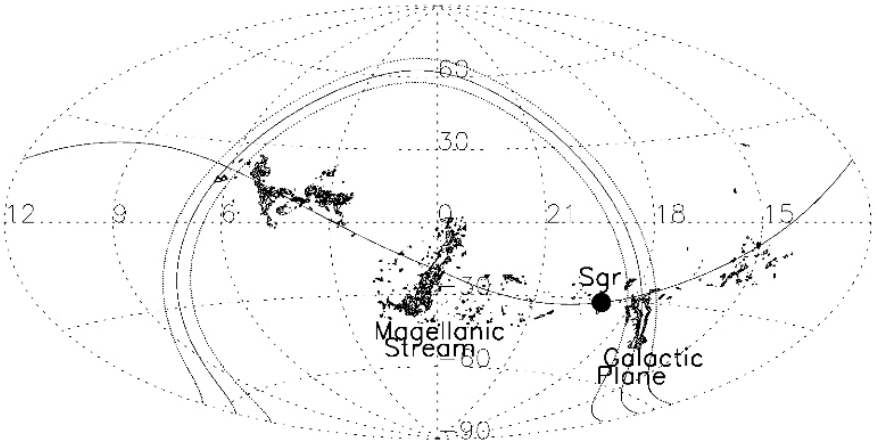

Figure 3.2: HIPASS data for velocities between $v_{LSR} \approx -85$ and $-400\,km\,s^{-1}$ along the Sgr orbit where the contours represent column densities of 0.5, 1.0, 5.0 and $10.0 \times 10^{19}\,cm^{-2}$ in celestial coordinates. Indicated is the galactic plane at $b = 0°$ (solid line through indicated Galactic plane gas) $\pm 5°$ (dotted lines). The current position of Sgr is marked with a large full circle and the solid line through it refers to its orbit (Ibata & Lewis 1998). The large gas complex at $\alpha \approx 3^h..5^h$, $\delta \approx 0°..25°$ is identified as part of the anti-center complex.

back-falling clouds would correlate to the HVCs. This theory predicts distances in the order of one kpc, velocities in the range of $v = 100\,km\,s^{-1}$ and metallicities of solar or even slightly higher than solar, because the gas would be SN enriched disk gas. In Sec. 2.1.3 several metallicity measurements are summarized showing that typical HVCs have metallicities below solar which is an issue for the galactic fountain model as an origin for the HVCs. In addition it is only able to explain distances to the galactic disk of a few kilo-parsec and the observed very high velocity clouds with $v < -200\,km\,s{-}^1$ are also very difficult to account for a ballistic motion since the initial energy to accelerate the hot gas to galactic heights, which explains the large velocities. Already Oort in 1969 mentioned that the observed velocities can not be produced by a free fall from heights a few kilo-parsec. More recently, Spitoni et al. (2008) investigated this theory to explain the origin of HVC Complex C and an intermediate velocity cloud IVC Arch IV and failed in both. While the mass, velocity and inferred galactic height did not fit the predictions of the galactic fountain model for Complex C, the metallicity of IVC Arch IV can only be reproduced if the assumed initial metallicity is as low as $1/100\,Z_\odot$, which is very unlikely for an origin in the galactic disk.

3.2 Tidal disruption of dwarf galaxies

The galactic halo includes in addition to different gas phases also dwarf galaxies which are currently accreted by the Milky Way as supposed in the hierarchical structure formations scenario. From Kepler's second law of motion an object

is sweeping out equal areas during equal intervals of time. For an object with unnegligible physical extent, like a dwarf satellite galaxy, a discrepancy between the velocity of the leading and the trailing part occurs which leads to a compression when reaching the pericenter and to a stretching when approaching the apocenter of the satellite's orbit through the galactic halo. This process leads to tidal disruption and together with ram pressure stripping (see Sec. 5.5.6 for details) material gravitationally bound to the dwarf galaxy can become unbound in a very effective way. Expected are stellar and gaseous over-densities on the derived orbits of the dwarf satellites, which are observed in the MW for example the Magellanic Stream (see Sec. 2.3.1), the Sagittarius Stream (Ibata et al. 1994, Majewski et al. 2003) and the Orphan Stream (Grillmair 2006, Belokurov et al. 2007). For initially gaseous satellites it is very likely that not only stars became unbound but also gas, which could the origin for the high velocity clouds. The Sagittarius dwarf galaxy (Sgr) is an remarkable object since there exist a population of stars associated with Sgr as young as 0.5 to 2 Gyrs indicating a star formation in the past few Gyrs. In this period of star formation, Sgr was supposed to contain a sufficient amount of HI, the star formation 'fuel'. Sagittarius HI observations (Koribalski, Johnston & Otrupcek, 1994) show a rather small amount of HI within this dwarf galaxy with $M_{HI} < 1.5 \times 10^4\, M_\odot[3\,\sigma]$. Burton & Lockman (1999) expanded the search for gas initially bound to Sgr to over 18 deg^2 from $b = -13°$ to $-18°.5$ without a match down to a $3\,\sigma$ mass limit of $M_{HI} < 7 \times 10^3\, M_\odot$. Putman et al. (2004) looked for an accordance of high velocity clouds on the orbit of the Sagittarius dwarf galaxy as possible tidal debris for the star forming material. In Fig. 3.2 high velocity clouds with negative velocities are indicated as well as the calculated orbit of Sgr (Ibata & Lewis 1998) in celestial coordinates. Since Majewski et al. (2003) presented a stream of M giants associated to Sgr following the orbit, but with a quite broad width of several degrees the gas is not expected to be distributed in an extremely narrow range around the proposed orbit. There are several smaller gas clumps with negative velocity as well as part of the anti-center complex (ACHV and ACVHV; Wakker & van Woerden 1991) located on the Sgr orbit. Not indicated in Fig. 3.2 is complex L at $\alpha \approx 15^h15^m$, $\delta \approx -19°.5$ with its high positive velocity not correlated with the position of the positive velocity stars along the stellar stream of the Sagittarius dwarf.

Although this theory is a good explanation for at least some HVCs (like the obvious connection between the Magellanic Clouds and the MS) is provides some problem for the origin of the other complexes, not yet correlated to any known dwarf galaxy and the subclass of compact high velocity clouds.

3.3 HVCs as Local Group building blocks

One of the first assumption of the HVC origin was already proposed by Oort (1969) and refers to the largest scales and the most distant formation both in time and in place. In this picture high velocity clouds are intergalactic gas clouds belonging rather to the Local Group system than to the Galaxy. Although the cosmological standard model of structure formation evolved a lot in the past 40 years, Oort already suggested, that this gas clouds could be part of the still ongoing formation of the Galaxy. Furthermore he correlated the cloudy structure to the galactic halo and estimated the neutral hydrogen gain of the Milky Way

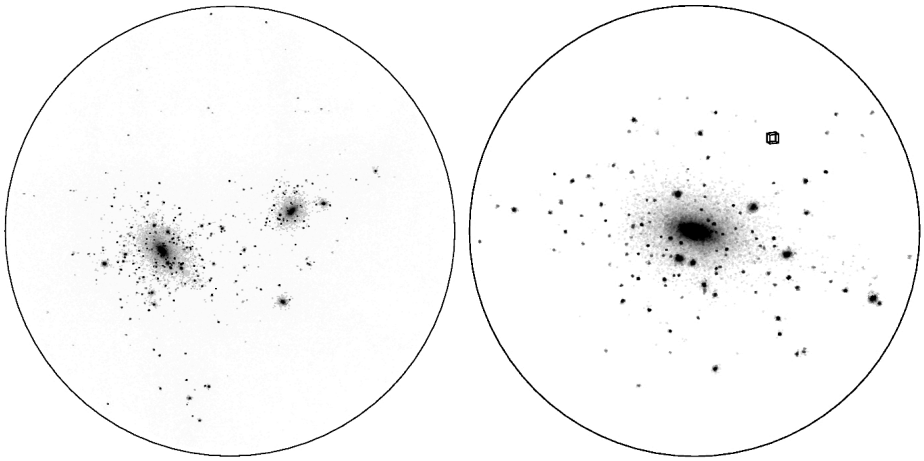

Figure 3.3: The dark matter distribution for a simulation by Klypin et al. (1999). The large circles correspond to a sphere of $1.5h^{-1}$ Mpc in the left figure, while on the right side a zoom-in is shown for a sphere of $0.5h^{-1}$ Mpc. The simulated group consists of two massive halos with $1.7 \times 10^{12} h^{-1}\, M_{\odot}$ and $7.9 \times 10^{11}\, h^{-1}\, M_{\odot}$ and 281 halos with a circular velocity $v_{circ} > 10\, km\, s^{-1}$. The small box indicated in the right figure refers to a size of $20\, h^{-1}$ kpc.

due to in-falling intermediate and high velocity clouds with about $3\, M_{\odot}/yr$. After 30 years of research with both better observations and a more detailed theory about the cosmological structure formation, Blitz et al. (1999) built on the idea of Oort (1969) and denotated the high velocity clouds as the "building blocks of the Local Group". He verified his theory with a simulation about the motion of the HVCs if they were extragalactic objects moving rather with the kinematics of the LG than with those of the Milky Way Galaxy, which was in good agreement with the observed distribution and galactic standard of rest velocities. For the ensemble of HVC he proposed typical distances in the order of 1 Mpc leading to a physical extent of 25 kpc, containing an HI mass of $3 \times 10^7\, M_{\odot}$ and $3 \times 10^8\, M_{\odot}$ of dark matter. Since there are direct distance measurements for the large complexes in the order of a few kilo-parsec these wide-spread object are those clouds captured by the gravitational potential of the MWG and therefore tidally disrupted and currently accreted. This explanation is supported by the higher velocity dispersion within the large complexes. The rest of the high velocity clouds are moving along filaments in the direction of the Local Group barycenter, which explains the group of high positive velocity clouds as well as those with high negative velocity and their asymmetric distribution in the galactic standard of rest frame. In addition Blitz et al. (1999) showed that the dispersion of the CHVC velocities decreases for switching to the LG standard of rest frame. This well-argued theory has issues explaining more recent searches for HVC analogues in other galaxies and in LG analogs with the results that all observed extragalactic HVCs are located within the halo of their host galaxy and until now no detection of HI gas in LG analogs was made (see Sec. 2.3.4). The detection limit in the LG analogs search by Pisano et al. (2004) in the range of $M_{HI} > 10^7\, M_{\odot}$ would be sufficient for the HVCs having masses as proposed by Blitz et al. (1999). For circumgalactic gas clouds with HI masses

of typically 10^5 to $10^6\,M_\odot$ no detection would be expected.

3.4 HVCs and Dark Matter Mini-halos

Sternberg, McKee & Wolfire (2002), hereafter SMW02, took a more detailed look on dark matter related to high velocity clouds. They proposed that the CHVC dark matter halos are probably part of the same family of dark matter halos, where the dwarf galaxies are assigned to. This would include an additional indication for a circumgalactic CHVC population. They also modeled DM mini-halos in distances of more than 780 kpc, referring to the theory by Blitz et al. (1999) but mentioned that in this case, the halos must be highly under-concentrated with DM densities smaller than $0.08\,cm^{-3}$ to reproduce the observed quantities like the column density as well as the observed multiphase structure. Focussing on a circumgalactic distribution of both HVCs and CHVCs the more compact subclass could be the solution to the 'missing satellite' problem, which will be explained in more detail later in this section. The predicted dark matter satellites of a simulation by Klypin et al. (1999) are shown in Fig. 3.3. Beside the fact that there is no star formation in CHVCs other features are in good agreement with observed features in dwarf satellite galaxies and SMW02 denoted them the 'starless cousins' of the dwarf galaxies. For example the multiphase structure in CHVCs can be compared to the multi-phased HI distribution in gas-rich dwarf irregular galaxies (dIrrs) and is similar in many ways.

3.4.1 The existence of non-baryonic Dark Matter

The theory of Dark Matter arises from the huge difference between the visible mass in galaxies and their dynamical mass, that explains the rotation curve of galaxies, the motion of galaxies in clusters or, with the general relativity, the gravitational lensing effect. This mass deviation was first observed by Zwicky (1933) and became together with the Big Bang Theory and a Dark Energy the standard cosmological model. Dark Matter (DM) describes any kind of mass that can not be directly observed, because it does not emit any kind of electromagnetic radiation and interacts only gravitationally. A small fraction of Dark Matter is baryonic, consisting of objects, whose masses are too small to burn helium, like brown dwarfs or planets and the final stages of stellar evolution as very faint white dwarfs and black holes. These object are called massive compact halo object (MACHO). Contrary to the baryonic DM an amount of non-baryonic dark matter is needed to describe many observed features. A very explicit indication for a large amount of non-baryonic dark matter is the abundance of elements supposed to be produced in the Big Bang. A very promising element for investigating the primordial abundances is deuterium, because it cannot be produced during any known process other than in the Standard Big Bang Nucleosynthesis (SBBN) (Epstein et al. 1976) but is destroyed already at quite low temperatures ($\approx 6 \times 10^5\,K$) by (p,γ) reaction and therefore totally burned away in any stellar fusion process. The number distribution of the element produced in the SBBN, H, D, ^{3}He, ^{4}He and ^{7}Li are sensitive to the unknown parameter $\eta_{10} = 10^{10} \times n_b/n_\gamma$, the ratio between the cosmic baryon and photon density in the Universe. The primordial abundance of deuterium ,

^{3}He and ^{7}Li are given by Dar (1995) with

$$[D]_p/[H]_p \approx 4.6 \times 10^{-4} \eta_{10}^{-1.67} \quad (3.1)$$

$$\left[^3He\right]_p/[H]_p \approx 3.0 \times 10^{-5} \eta_{10}^{-0.5} \quad (3.2)$$

$$\left[^7Li\right]_p/[H]_p \approx 5.2 \times 10^{-10} \eta_{10}^{-2.43} + 6.3 \times 10^{-12} \eta_{10}^{2.43} \quad (3.3)$$

Songaila et al. (1994) and Carswell et al. (1994) detected the Lyman α line of deuterium in a distant low metallicity cloud at red-shift Z=3.32. They reasoned from line shape fitting a deuterium abundance of $[D]_p/[H]_p = (1.9-2.5)\times 10^{-4}$. The measurements of ^{3}He show a very large variety and cannot be used for a valuation of the primordial ^{3}He abundance. Thorburn (1994) estimated the primordial ^{7}Li abundance with $\left[^7Li\right]_p/[H]_p = (1.7 \pm 0.4) \times 10^{-10}$. The best agreement between the SBBN and the observations in dependence of η_{10} is for $\eta_{10} = 1.6 \pm 0.1$ with a confidence level of 70 % (see Fig. 3.4). With $n_\gamma = 411 \pm 8\, cm^{-3}$ the number density of the relic photons of the Big Bang, derived from the Cosmic Microwave Background, the baryon density n_b can be calculated with

$$n_b = 10^{-10} \eta_{10} n_\gamma = (6.6 \pm 0.5) \times 10^{-8}\, cm^{-3} \quad (3.4)$$

The baryon mass density over the critical density $\rho_c = 3H_0^2/8\pi G$ is then

$$\Omega_{b(theory)} = \rho_b/\rho_c = (0.0058 \pm 0.0007) h^{-2} \quad (3.5)$$

The mass density of the visible baryons is estimated by Dar (1995) with

$$\Omega_{b(observed)} = \rho_b/\rho_c = (0.0045 \pm 0.0015) + (0.0018 \pm 0.0006) h^{-3/2} \quad (3.6)$$

For the most recent value for the Hubble constant $h = 0.742 \pm 0.036$, released on May 7, 2009 on hubblesite.org, measured with the Hubble Space Telescope (HST), there is not much room for a large amount of baryonic dark matter (see Fig. 3.4 right). Although no non-baryonic dark matter particle was found the theory of weakly interacting massive particles (WIMPs) as an explanation for the missing matter was already introduced in the 1980s (Peebles 1982, Blumenthal et al. 1984, Davis et al. 1985). The total matter (baryons + dark matter) density in terms of the critical density $\Omega_M = (\rho_b + \rho_{dm})/\rho_c$ is derived with cosmic microwave background (CMB) observations for example by the Wilkinson Microwave Anisotropy Probe (WMAP) (Hinshaw et al. 2003) and the BOOMERANG experiment (MacTavish et al. 2006) and with measurements of the gravitational lensing effect (e.g. Dobke et al. 2009). The current critical density $\Omega_0 = \Omega_{CDM,0} + \Omega_{B,0} + \Omega_{\Lambda,0}$ is supposed to be $\Omega_0 = 1$ for a flat universe, which is indicated by observations about the angular power spectrum of fluctuations in the temperature of the cosmic microwave background (de Bernardis et al. 2002) and is expected by an inflationary universe. Ω_Λ is the amount of dark energy in the universe and due to its dominating energy density fraction a very important part for the understanding of structure formation in the ΛCDM theory. Since the distribution of the dark energy is supposed to be homogenous up to very large scales the contribution of dark energy in the kinematics of a gas clouds falling onto a larger galaxy is negligible and is not

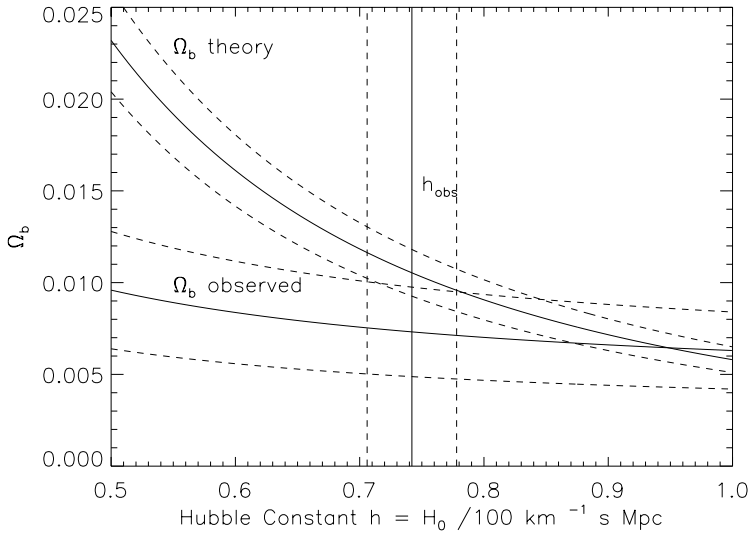

Figure 3.4: The theoretical and the observed baryonic mass density for different hubble constants with error boundaries (dashed lines). The vertical line indicates the most recently published value for h, again with dashed error boundaries.

taken into account in this work. The standard values for the matter density and the dark energy density are $\Omega_M = 0.3$ and $\Omega_\Lambda = 0.7$. See Table 4 of MacTavish et al. (2006) for a summary of cosmological parameters measured from several CMB observations.

3.4.2 Hierarchical Structure Formation

The observed universe shows structures on scales of many orders of magnitude, from stars up to the "cosmic web" made of clusters and super-clusters separated by huge voids. In the Λ-CDM theory all structures evolve from initially small scale density fluctuations, which can still be measured as the Cosmic Microwave Background (CMB) at a black-body temperature of 2.725 K (see Fig. 3.5). The CMB is a result of the era of recombination when the temperature of the universe drops due to its fast expansion during the cosmic inflation and protons and electrons could form the first hydrogen atoms. At this time, after about 0.4 Myrs after Big Bang the universe became transparent since the photons could travel freely in space from this time on. The primordial adiabatic fluctuations follow a power law spectrum that can be measured in the CMB and provides a good prove for the determination of several cosmological parameters. The regions with initially only small over-densities grow due to gravitation and became the progenitors of the large scale structures in today's universe. The Press-Schechter

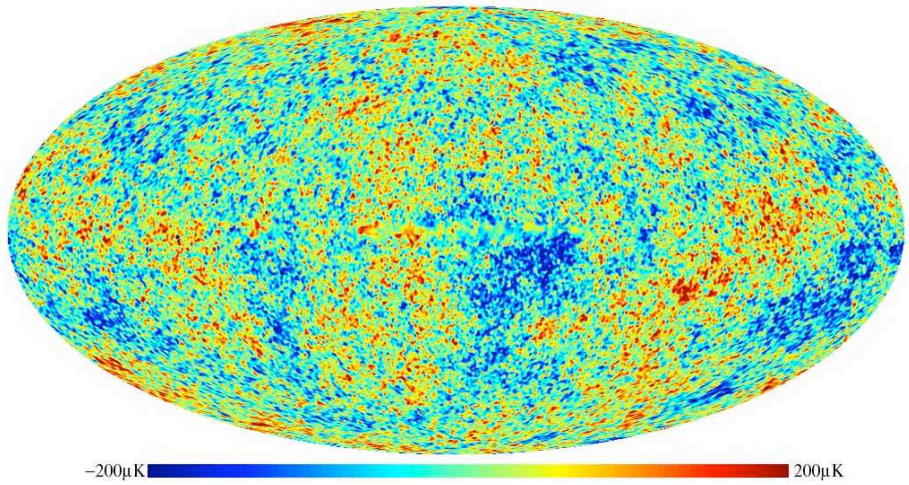

Figure 3.5: WMAP image of the Cosmic Microwave Background. Color coded are the small temperature deviations from the black body temperature of T=2.725 K.

theory bases on a hierarchical structure formation where smaller haloes form first and merge into larger haloes with time.

Giocoli et al. (2007) presented results of the GIF2 simulation (Gao et al. 2004) where the formation histories of large haloes are probed with cosmological parameters $\Omega_m = 0.3$, $\sigma_8 = 0.9$, $h = 0.7$ and $\Omega_b = 0.04$, where σ_8 is the rms mass fluctuation in spheres of $8h^{-1}$ Mpc in radius. For every halo at $z_0 = 0$ more massive than $10^{11.5}h^{-1}\,M_\odot$, they trace them backwards in time, chosing for every $z > z_0$ the progenitor which contributes the largest number of particles. Therefore a mass dependent history of the most massive progenitor is created and shown in Fig. 3.6. Comparing histories of haloes with different masses at z=0 shows that smaller halos form earlier than the more massive ones. While the largest haloes with masses between $\log_{10} M/h^{-1}M_\odot = 13.5-14$ (lower left panel of Fig. 3.6) collected half of their mass at z_0 at a red-shift of approximately z=0.5, the smallest haloes in this simulation with $\log_{10} M/h^{-1}M_\odot = 11.5-12$ are already built up to 50% of $M(z_0)$ around z=1.4.

Another large simulation focusing on the evolution of large scale structures was made by MPA Garching and is called the Millennium simulation. The result is quite similar to those of the GIF2 simulation, smaller halos form at high red-shifts and evolve due to gravitational merging processes into larger systems.

3.4.3 Dark Matter Mini Halos

The ongoing process of hierarchical structure formation described above is not 100% effective. Some of the smaller dark matter haloes should have survived until now and this is in agreement with the observations of satellites around the Milky Way and other galaxies. The number of observed satellites in the vicinity of the MW is much smaller than the number predicted in several numerical

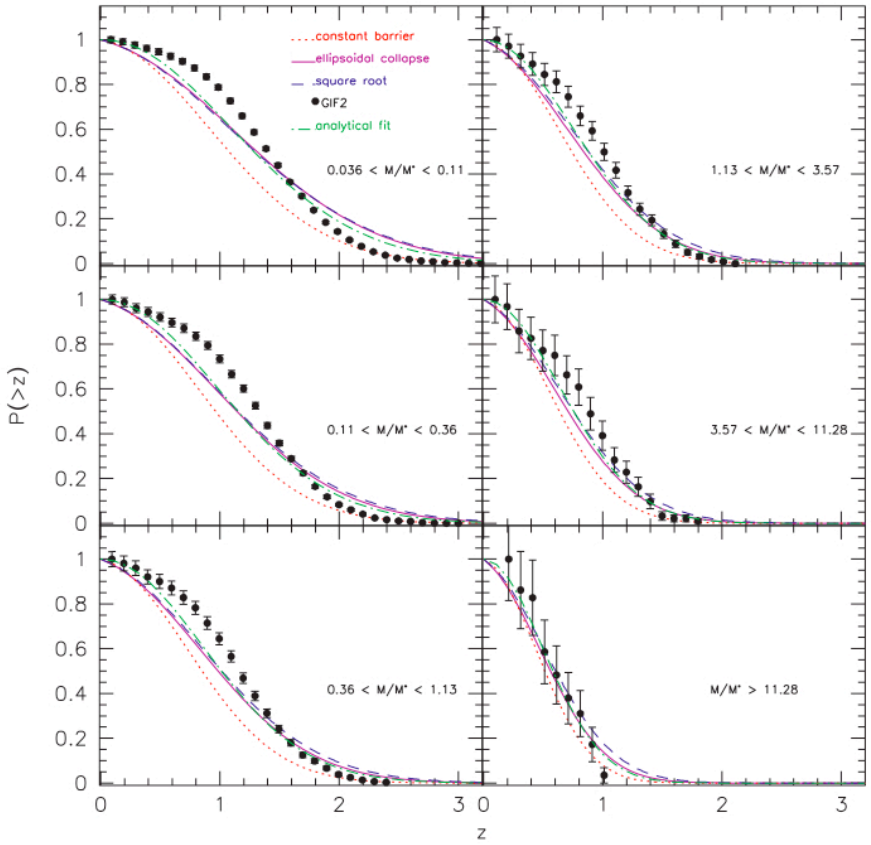

Figure 3.6: Result of the GIF2 simulation compared to several theoretical solutions (for details see Giocoli et al. 2007). The panel from top left to bottom right show the formation of halos with $\log_{10} M/h^{-1}M_{\odot}$ = 11.5-12, 12-12.5, 12.5-13, 13-13.5 and 13.5-14. Figure from Giocoli et al. (2007)

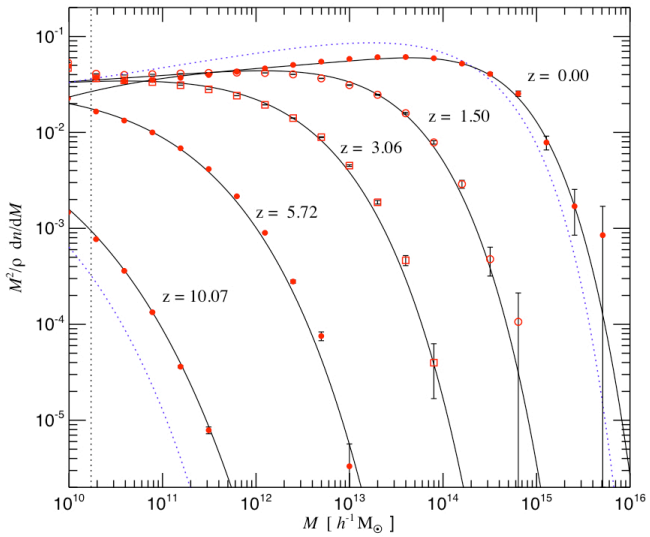

Figure 3.7: Halo number density in dependence of the mass for different redshifts z from the Millennium simulation (Springel et al. 2005). Solid lines indicate the analytic solutions from fitting functions (Gelb & Bertschinger 1994) and dashed lines are the Press-Schechter model et z=10.07 and z=0. Figure from Springel et al. (2005)

simulation for MW sized galaxies (around a dozen satellites observed vs. 50 dark matter haloes predicted with $M > 10^8\,M_\odot$ within a 570 kpc radius, Klypin et al. 1999). The discrepancy is even more considerable on larger scales where the ≈40 observed satellite galaxies in the Local Group are confronted with around 300 predicted dark matter haloes (Klypin et al. 1999). A possible explanation of the missing dark matter satellites are the compact high velocity clouds.

Summary The origin of high velocity clouds can still not be explained with one over-all theory, and it seems that the intrinsic variety within the class of HI clouds with anomalous velocity is too large to aim for an unified theory. Although it is possible that the wide-spread complexes are the local analogs to the more distant CHVC and due to their smaller distance to the Milky Way opposed to tidal disruption, it becomes difficult to balance it with the relation of some complexes, at least the Magellanic Stream, to dwarf satellite galaxies. In addition there also exist intermediate velocity HI clouds, which are more likely to be the back-falling bullets from a galactic fountain than the HVCs. Future observations and the fast increasing field of hydrodynamical simulations provide an optimistic foil to a better understanding of the structure formation of the universe intrinsically tied to the origin of the high velocity clouds.

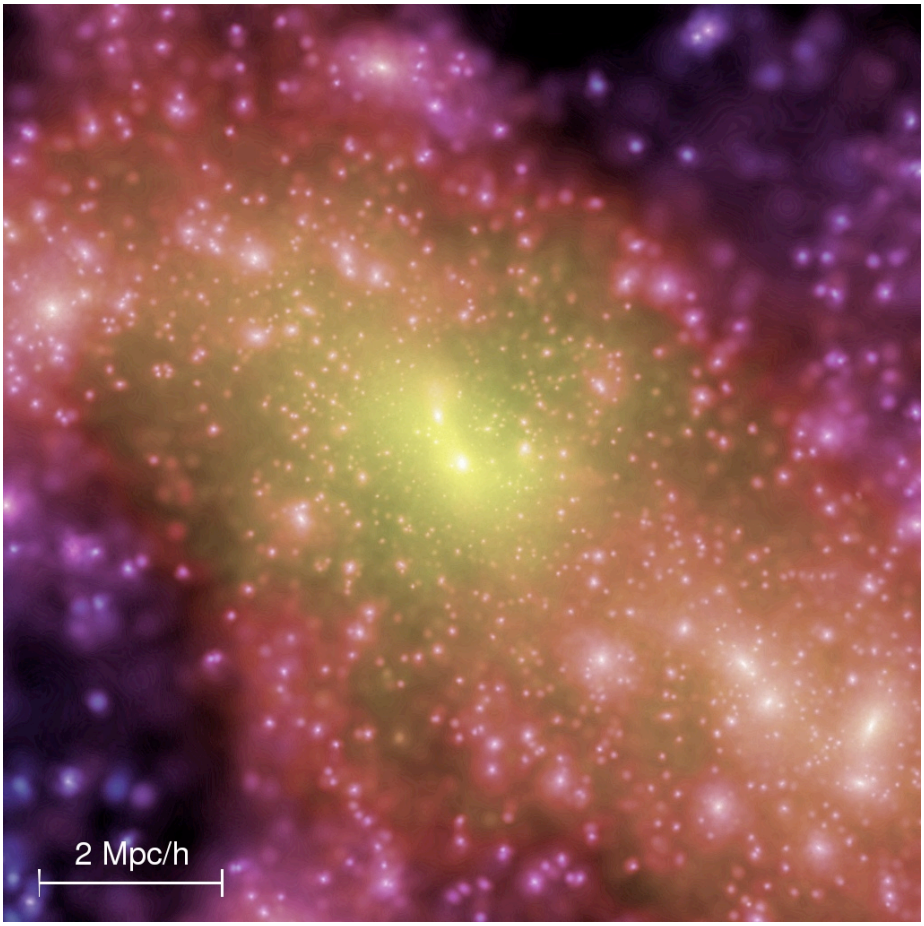

Figure 3.8: Dark matter distribution of the millennium simulation at z=0 for a rich galaxy cluster. Figure from: www.mpa-garching.mpg.de/galform/millennium/

Chapter 4

About the FLASH code

The Center for Astrophysical Thermonuclear Flashes, or Flash Center, was founded at the University of Chicago in 1997 under contract to the US Department of Energy as part of its Accelerated Strategic Computing Initiative (ASCI) to solve several problems especially connected with the X-ray bursts, Type Ia supernovae and classical novae in correlation with neutron stars and white dwarfs. FLASH is a very complex, parallelized (uses Message-Passing Interface, MPI) code with adaptive mesh refinement and many physical modules already included, as modules dealing with hydrodynamics, self-gravity, thermal processes and magnetohydrodynamics. Although FLASH was originally created for different astrophysical environments, its competence in working with strong shocks and the included, well tested modules provide a good basis for necessary adjustments to this specific problem. For all simulations in this thesis, version FLASH2.5 is used.

4.1 Adaptive mesh refinement

The FLASH code uses adaptive mesh refinement techniques (AMR) which are irreplaceable for simulations, which cover a large spatial range but need a high resolution in time-dependent areas. Based on a coarse grid, the AMR makes sure, that a sufficient resolution in "interesting" areas is reached, while in regions without a large variety of the required parameters the grid size is adapted to save memory space and CPU time (see Fig. 4.1). The conditions for a block to be refined are discussed in following paragraph "The PARAMESH package", which is beside DAGH, AMR++ and SAMRAI one of the AMR packages included in the FLASH code. They are all parallel, dynamic and all use guard cells at subgrid boundaries to get informations from the close-by subgrids. For further information about the differences between the single AMR packages see Fryxell et al. (2000).

The PARAMESH package covers the entire domain with a number of parent blocks by halving the calculation range in every dimension. The newly created blocks are then either separated in user applied number of cells, or building other parent blocks with the described halving procedure until the designated resolution is reached. This leads to a hierarchical structure with regions

of different cell sizes. Figure 4.1 explains the tree-like appearance in an example with a two dimensional set of blocks. The whole area is separated into quadrants, furthermore two of them are again divided in different parts. With every partition the cell size is scaling down with a factor of two, leading to an increased resolution, while the number of cells, compared to the parent block, is still the same. Every single PARAMESH block is neighboring a user-supplied quantity of guard cells which are usually filled with data of the nearby blocks or some boundary conditions. Beside the hierarchical building of sub-grids, the main work-scope of PARAMESH is to manage the splitting of the individual blocks to the different processors, the block's spatial configurations and therefore most of the inter-block and inter-processor communication. For this reason every block saves beside the x, y, z coordinates and the bounding box information, integer numbers assigned to each of its parent, child and neighbor blocks and another integer according to the processor on which the block data is located (see bottom part of Fig. 4.1). In case of increasing or decreasing a block's resolution, the single blocks are marked during a special loop depending on a user-defined criterion. The default criteria used in the FLASH code based on Löhner (1987) (Equ. 4.1 to Equ. 4.2) Equ. 4.1 shows a numerical finite difference estimate of the second derivative on a uniform mesh of spacing in one dimension. Δx . The modified second-derivative error norm of a uniform mesh is calculated in Equ. 4.2 for the general multidimensional case, where the indices k and l indicate the multi-dimensions. ϵ is a constant factor with a value of 0.01.

$$\frac{\partial^2 u}{\partial x^2} \approx \frac{u_{i+1} + 2u_i + u_{i-1}}{\Delta x^2} \tag{4.1}$$

$$E_i = \left(\sum_{k,l} \frac{(\partial^2 u / \partial x_k \partial x_l)}{[(|\partial u/\partial x_k|_{i+1} + |\partial u/\partial x_k|_i)/\Delta x_l + \epsilon |(\partial^2/\partial x_k)\partial x_l||u|]^2} \right)^{1/2} \tag{4.2}$$

The tunable constants CTORE and CTODE are criteria for a possible change of resolutions. For each block marked as "refined" ($E_i > CTORE$), a set of two, four or eight individual child blocks is created. Within the tree structure these new blocks are located at the end of the list on the processor of the corresponding parent block. The de-refinement routine (started for blocks with $E_i < CTODE$) simply erases the blocks which are no longer necessary and the memory space is released for overwriting. After the refinement/ de-refinement routine is finished, a redistribution of the blocks is started, to avoid an unbalance between the single processors. This is accomplished using a work-weighted, Morton space-filling curve. For details see e.g. Warren & Salmon (1993), using a Morton curve for a parallel, gravitational N-body tree code, and Dorband (1988) for further information about the parallel bitonic sort used for the redistribution of the Morton number.

In Fig. 4.1 the rearrangement of the refinement structure during a simulation run is shown.

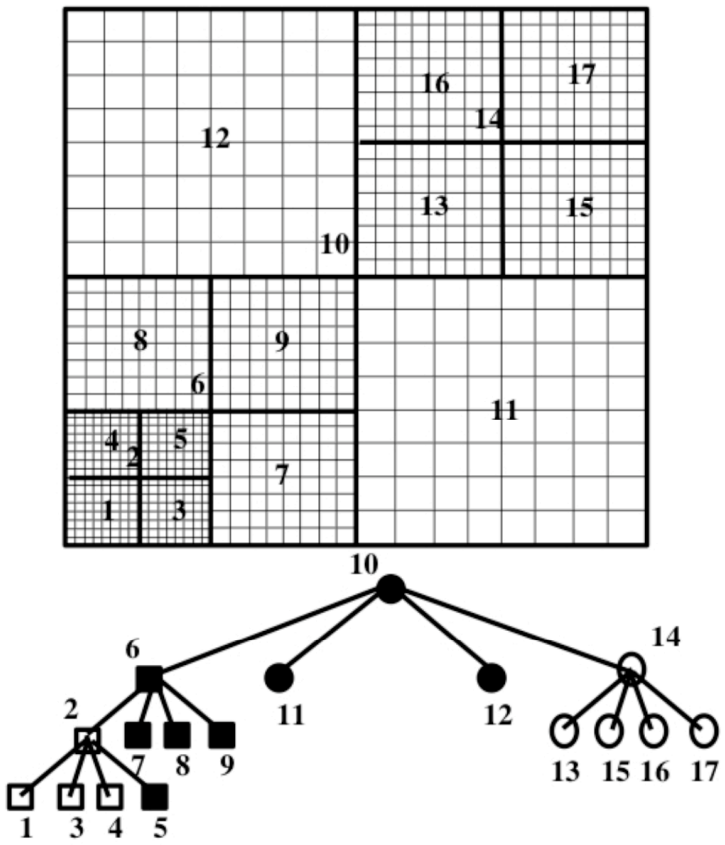

Figure 4.1: The domain in the upper part of this figure (block number 10) is separated into 2 × 2 smaller blocks (blocks 12, 14, 6 and 11). While in the areas covered by blocks 12 and 11 the resolution is sufficient, blocks 14 and 6 are separated again into 2 × 2 smaller blocks to the next level of refinement. The highest resolution in this schematic figure is reached in the area covered by block 2. In the lower part of the figure, the tree based structure for a four processor parallel machine is shown. Each symbol stands for one of the four processors, while the numbers, which are Morton sorted, are according to the block numbers in the upper part of this figure. Figure from Fryxell et al. (2000)

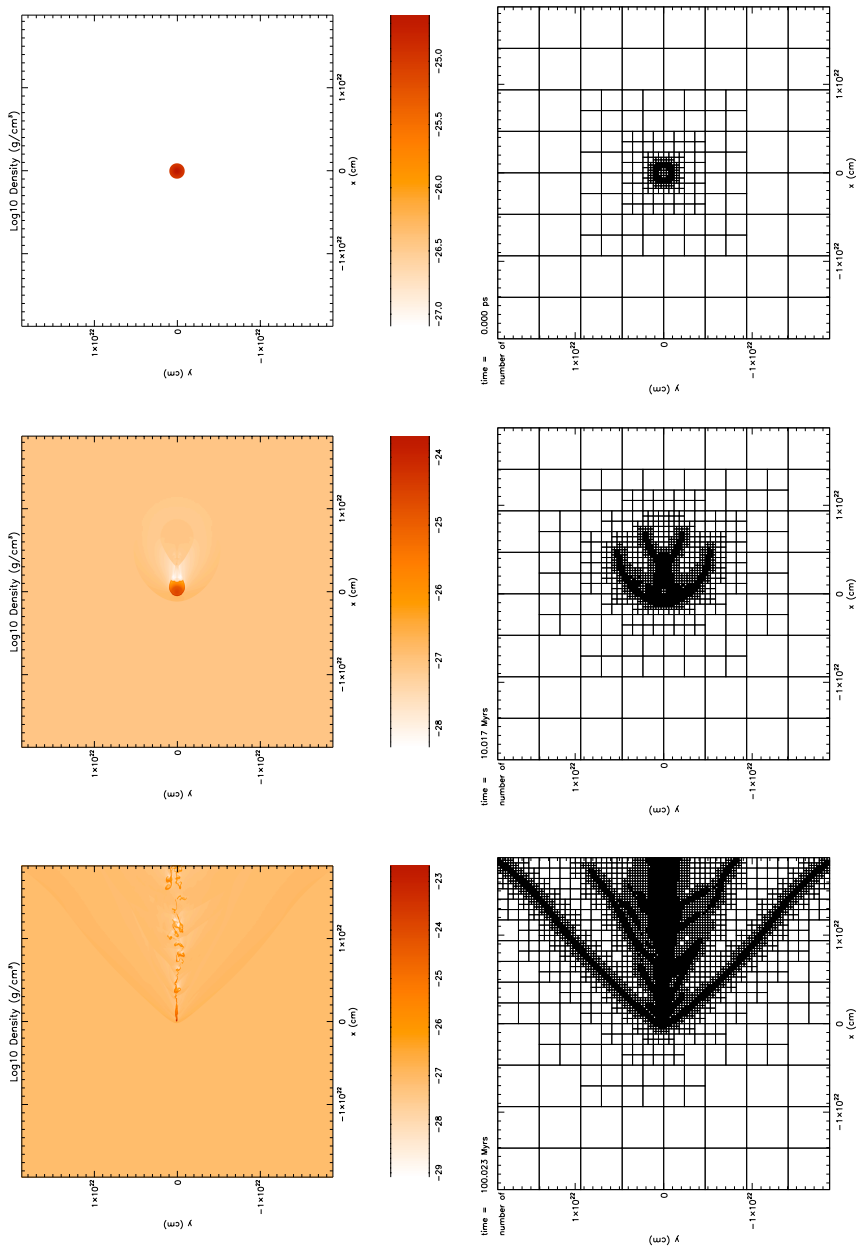

Figure 4.2: Adaptive Mesh Refinement up to six levels of refinement. Left Panels: Log Density distribution of the initial cloud (top), after 10 Myrs (middle) and 100 Myrs (bottom). Right Panels: Blocks of the AMR grid after the same periods of time as in the left figures. Each Block consists of 8x8 cells.

Chapter 5

Simulation

5.1 Initial Conditions

5.1.1 The Lane Emden Equation

In astrophysics, the Lane-Emden equation is Poisson's equation for the gravitational potential of a self-gravitating, spherically symmetric polytropic fluid.

$$\frac{1}{\zeta^2}\frac{d}{d\zeta}\left(\zeta^2\frac{d\theta}{d\zeta}\right)+\theta^n=0 \tag{5.1}$$

where:

$$\zeta = r\left(\frac{4\pi G\rho_c^2}{(n+1)P_c}\right)^{1/2} \tag{5.2}$$

The solution of the Lane Emden equation leads to the radial density profile:

$$\rho = \rho_c\theta^n \tag{5.3}$$

Using the polytropic equation, the pressure distribution is determined by:

$$P = K\rho^{1+\frac{1}{n}} \tag{5.4}$$

$$K = \left(\frac{N_A k_B T}{\mu}\right)\rho^{-1/n} \tag{5.5}$$

Analytical solutions are known for n = 0, 1 and 5. Choosing a more realistic polytropic index (n=1.5) requires a numerical solution. The solution is beside the polytropic index n dependent on the central density and pressure, where the pressure is correlated with the density using the polytropic equation, where other parameters (temperature T and μ) occur. For a constant $\mu = 0.5$ for neutral hydrogen, only the central density and the cloud's temperature remain as free parameters.

Problem: The solution of the Lane-Emden equation does not allow for neither an ambient pressure nor does it accomplish for the thermal equilibrium, so a more general initial distribution is required.

5.1.2 Initial Condition for a Stable Cloud

In agreement with the stable clouds in the Ph.D. thesis by Vieser (2001) the density and temperature distribution and therefore the pressure distribution connected by the equation of state are modified. The requirement for a reasonable initial density and pressure model is in this case the condition that the cloud should be stable over at least 100 Myrs without any additional processes like streaming and the corresponding ram pressure.

Pressure Equilibrium The first and therefore most simple model includes only pure hydrodynamics. The pressure of the cloud is distributed homogeneously and contains the value of the surrounding interstellar medium. In this case the cloud is in pressure equilibrium with the ambient hot medium.

$$p_{cloud}(r) = p_{ism} \tag{5.6}$$

The initial temperature and density distributions are connected within the equation of state, assuming an ideal gas:

$$T_{cloud}(r) = \frac{1}{R_{ideal}} \cdot \frac{p_{cloud}}{\rho(r)} \tag{5.7}$$

where R_{ideal} is the ideal gas constant. This first assumption leads to the pressure equilibrium and running the simulation shows the required stability with a large variety of initial temperature and density profiles.

Self-Gravity The simulated stable clouds have gas masses in the range of 10^5 to $10^6 M_\odot$ and are therefore supposed to be dominated by self-gravity. The simple model of pressure equilibrium is not longer useable and additional constraints to the radial distribution of temperature, density and pressure are needed to compensate the self-gravity, which would lead to a collapse of the cloud. Since no star formation was observed in HVCs so far, a cloud collapse must not occur in the simulation. The hydrostatic equilibrium of a cloud with selfgravitation leads to a relation between the pressure derivative and the derivative of the gravitational potential:

$$\frac{dP}{dr} = -\rho(r)\frac{\partial\phi(r)}{\partial r} \tag{5.8}$$

The inital density profile of the cloud and subsequently its gravitational potential is in spherical symmetry, leading to a gravitational acceleration $\frac{\partial\Phi}{\partial r}$ that depends only on the enclosed mass within the radius r

$$\frac{\partial\Phi}{\partial r} = \frac{G\,M(r)}{r^2} \tag{5.9}$$

with $M(r) = \int_0^r 4\pi\rho(r')(r')^2\,\mathrm{d}r'$ is the enclosed mass.

Since the pressure is dependent of the temperature the pressure derivative can be substituted with $\frac{dp}{dr} = \frac{dp}{dT}\frac{dT}{dr}$ and therefore the radial temperature function is determined by:

$$\frac{dT}{dr} = -G\frac{M(r)\rho(r)}{r^2} \cdot \left(\frac{dp}{dT}\right)^{-1} \tag{5.10}$$

The iteration starts for a given central temperature and central density and the cloud is built up from the innermost core to the edge with

$$\frac{\Delta T}{\Delta r} = -G\frac{M(r)\rho(r)}{r^2}\cdot\left(\frac{dp}{dT}\right)^{-1} \quad (5.11)$$

$$\Delta T = -G\frac{M(r)\rho(r)}{r^2}\cdot\left(\frac{dp}{dT}\right)^{-1}\cdot\Delta r \quad (5.12)$$

$$T(i) = T(i-1)+\Delta T(i) \quad (5.13)$$

where the cloud radius r_c is subdivided into nr parts, where nr is a free parameter and $\Delta r = r_c/nr$ is the length of the iteration step.

The above temperature distribution describes a cloud, which is stable under the effect of self-gravity. The central temperature T_0 of the cloud can be determined with the condition of a pressure equilibrium at the edge of the cloud.

Self-Gravity + Thermal Processes Including the heating and cooling processes described in Sec. 5.6 requires different intial distributions of the physical parameter. The most important modification is that the density in a function of the temperature now, since the cloud should be in thermal equilibrium and the temperature/density parameter pairs therefore have to be located at the equilibrium function of the heating and cooling processes (see Sec. 5.6.3 for details). Equ. 5.10 now reads

$$\frac{dT}{dr} = -\frac{4\pi}{3}G\rho(T)^2 r\cdot\left(\frac{dp(\rho(T))}{dT}\right)^{-1} \quad (5.14)$$

The integration starts again from a central temperature T_c with a corresponding ρ_c which is calculated from the heating and cooling equilibrium curve. The initial 1D temperature profile can be integrated from $r = 0$ to $r = r_c$. Together with $\rho(T)$ at every cloud radius r and the pressure from the equation of state, the initial cloud distribution is determined. Taking into account the ambient hot medium, the central temperature T_c is modified in a way, that the pressure equilibrium is fulfilled within an adjustable accuracy. Therefore the only free parameters are the cloud radius r_{init} and the temperature of the ambient medium T_{ISM} which is together with $\rho(T_{ISM})$ responsible for the pressure of the interstellar medium and subsequently for the construction of the cloud. In all simulations in this thesis, the cloud radius is determined and the central temperature is constructed out of the above temperature distribution and the pressure equilibrium at r_c. Another possibility is to determine the central temperature and the radius of the cloud follows from the radius where the cloud pressure equals the pressure of the ambient medium.

Self-Gravity + Thermal Processes + Dark Matter Mini Halo The aim of this thesis is to investigate the behaviour of the gas cloud for the case, that it is embedded in a dark matter minihalo with masses of 10 to 100 times the gas mass of the cloud. For a stable gas cloud an additional massive gravitational potential would lead to a collapse of the cloud, which can be avoided by using appropriate initial conditions. In this simulation a Burkert (1995) dark matter halo is used following the density distribution:

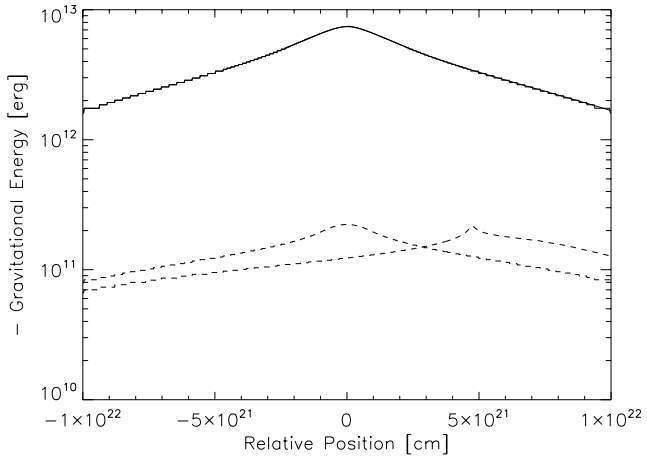

Figure 5.1: Comparison of the gravitational energy with (solid line) and without a DM halo ($r_{halo} = 750pc$, $r_0 = 300pc$, dashed lines). Indicated are the inital 1D distributions and the distributions after 100Myrs. The steps occuring in the line profiles are due to the adaptive mesh refinement.

$$\rho_{DM}(r) = \frac{\rho_0 r_0^3}{(r + r_0)(r^2 + r_0^2)} \tag{5.15}$$

Burkert (1995) showed a correlation between r_0 and the rotational velocity v_0 for dwarf galaxies. Assuming a spherical symmetry, the scaling relation between r_0 and ρ_0 can be derived, leading to a dark matter density distribution only dependent from the parameter r_0.

$$\rho_0 = 4.5 \times 10^{-2} \left(\frac{r_0}{kpc} \right)^{-2/3} M_\odot pc^{-3} \tag{5.16}$$

Solving Poisson's equation (Equ. 5.8) for the density distribution of the Burkert halo leads again to the temperature derivative. As a second parameter the halo size r_{halo} is introduced where for the gravitational potential of the dark matter halo at r_{halo} the condition is: $\Phi(r_{halo}) = 0$.

Beside the initial distribution of the gas cloud, the interaction of the gas and the dark matter has to be determined. For an additional gravitational potential an additional density has to be initialized that should not interact like the baryonic density does. This dark matter density should appear in the self-gravity module, but should not effect the equation of state or any thermal processes. An easy, but very effective way is to modify the right side of the Poisson equation, that the particular DM density (in dependence

of the distance from the initial center of the cloud) is added to the baryonic density, so that the DM only interacts gravitationally, as designated. In FLASH2.5 the right side of Poisson's equation is calculated in the multigrid solver (FLASH2.5/source/mesh/solvers/multigrid/mg_init_src.F90). Initially the stored gas density ρ_{gas} is used to determine the gravitational potential:

$$\triangle\phi = -4\pi G\rho_{gas} \tag{5.17}$$

If the gravitational potential consists of baryonic and dark matter density, the Poisson equation reads

$$\triangle\phi \quad = \quad -4\pi G(\rho_{baryonic}(x,y,z) + \rho_{darkmatter}(r)) \tag{5.18}$$

where the baryonic density distribution $\rho_{baryonic}(x,y,z)$ is taken from the stored density values for each timestep, and is especially in the runs with streaming not radially symmetric and highly varying over time. The dark matter potential stays uneffected since it is not interacting with the interstellar medium and is therefore constant over time. A comparison between a run with dark matter halo an another one without dark matter halo can be found in Fig. 5.1. While the gravitational potential is dominated by the constant dark matter halo in the first case and stays therefore constant over the simulation time of 100Myrs the gravitational potential of the run with only baryonic density the change of the potential is obvious.

5.2 Time-Stepping

Hydro Time-step Courant - Friedrichs - Lewy (hereafter: CFL) condition, named after R. Courant, K. Friedrichs and H. Lewy is an upper time-step limit for numerical solutions with explicit time marching. For the two dimensional case the interrelationship between the velocity (u_x, u_y), the time-step (Δt), the length interval $(\Delta x, \Delta y)$ and a constant C with is dependent of the equation to be solved is:

$$\frac{u_x \cdot \Delta t}{\Delta x} + \frac{u_y \cdot \Delta t}{\Delta y} < C \tag{5.19}$$

5.3 Hydrodynamic Equations

FLASH uses Euler equations for compressible, inviscid fluids. The first hydrodynamic equation, the equation of mass conservation arises from the consideration of a volume, where the deviation of the density within that volume in time $\frac{\partial\rho}{\partial t}$ has to be equal to the total mass flux through the boundaries $\bigtriangledown(\rho\mathbf{v})$.

$$\frac{\partial\rho}{\partial t} + \bigtriangledown(\rho\mathbf{v}) \quad = \quad 0 \tag{5.20}$$

The second Euler equation arises from the momentum conservation analogous to the mass conservation above, leading to a local conservation of momentum $\frac{\partial(\rho v_i)}{\partial t} = -\bigtriangledown_j(\rho v_i v_j)$ (vector-component notation). In addition the effects

of pressure derivative $\bigtriangledown P$, which leads to momentum transfer and an external force due to gravitational acceleration $\rho\mathbf{g}$ are taken into account.

$$\frac{\partial \rho \mathbf{v}}{\partial t} + \bigtriangledown(\rho \mathbf{v}\mathbf{v}) + \bigtriangledown \mathbf{P} = \rho \mathbf{g} \tag{5.21}$$

The last equation represents the conservation of the total energy:

$$\frac{\partial \rho E}{\partial t} + \bigtriangledown[(\rho E + P)\mathbf{v}] = \rho \mathbf{v} \cdot \mathbf{g} \tag{5.22}$$

where ρ is the density of the fluid, $\mathbf{v}$ the fluid velocity, P the pressure, whereas E is the total energy per mass unit (internal energy ϵ plus kinetic energy: $E = \epsilon + 1/2v^2$), $\mathbf{g}$ is the gravitational acceleration and P is the pressure, calculated with the equation of state.

5.4 Equation Of State (EOS)

In the present work, a gamma law equation of state, $P = (\gamma - 1)\rho\epsilon$, is assumed to describe the physical state of the gas, where γ is the ratio of specific heats, ρ the fluid density and ϵ the internal energy.

5.5 Instabilities

5.5.1 Rayleigh-Taylor Instability

The **Rayleigh-Taylor Instability** or RT instability (after Lord Rayleigh and G. I. Taylor), is a hydrodynamic instability arising at an interface between two fluids of different densities, which occurs when the heavier fluid ρ_2 is pushing the lighter fluid ρ_1. This configuration is reached when two fluid layers in a gravitational field are arranged in a way, that the denser fluid is located above the more tenuous one. In astronomy, RT instabilities are often visible in Supernova remnants (SNR) as a finger-like structure. Including magnetic fields, the RT instabilities can align the magnetic field lines.

The instabilities are analyzed using linearisation, a tool in calculation of perturbations, where the initial stationary system is deflected by an infinitesimal perturbation , for example $\rho = \rho_0 + \delta\rho$, where ρ_0 is the stationary value, and $\delta\rho$ the perturbation. Only linear perturbations are take into account, those of higher orders, like $\delta\rho \cdot \delta\rho$ or $\delta\rho \cdot \delta v$ are ignored. For the RT instability, where the density in x-direction and in z-direction is initially constant, the linearised hydrodynamic equations with a gravitational acceleration in z-direction read

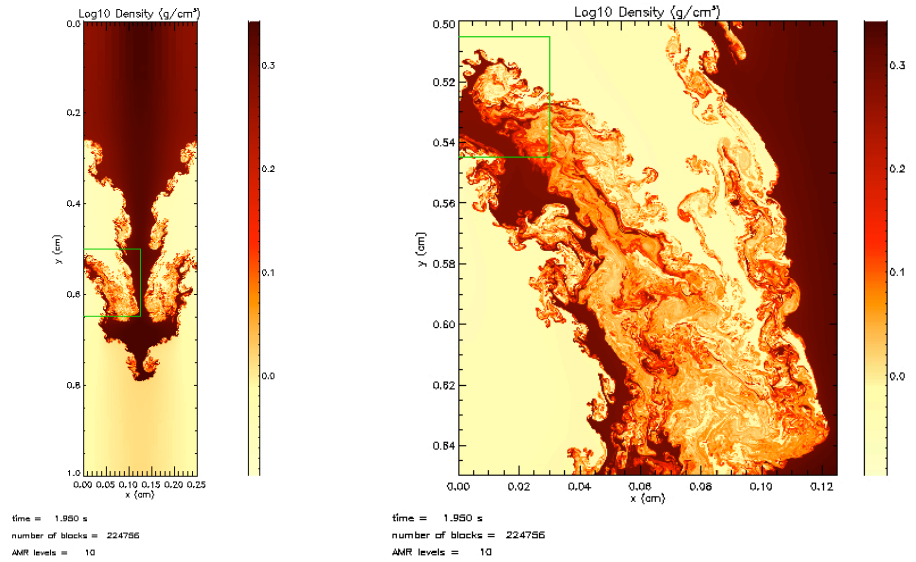

Figure 5.2: Rayleigh-Taylor and Kelvin-Helmholtz Instabilities, created with FLASH Code for 10 levels of refinement. The left figure shows the whole computational domain, while the right figure is a zoom in the green marked area of the figure on the left. (http://flash.uchicago.edu/ zingale/rt_gallery/rt_gallery.html)

$$\frac{\partial}{\partial t}(\delta\rho) = -\delta v_z \frac{\partial \rho}{\partial z} \tag{5.23}$$

$$\rho\frac{\partial}{\partial t}(\delta v_x) = -\frac{\partial}{\partial x}(\delta p) \tag{5.24}$$

$$\rho\frac{\partial}{\partial t}(\delta v_y) = -\frac{\partial}{\partial y}(\delta p) \tag{5.25}$$

$$\rho\frac{\partial}{\partial t}(\delta v_z) = -\frac{\partial}{\partial z}(\delta p) - g_z\delta\rho \tag{5.26}$$

$$\frac{\partial(\delta v_x)}{\partial x} + \frac{\partial(\delta v_y)}{\partial y} + \frac{\partial(\delta v_z)}{\partial z} = 0 \tag{5.27}$$

The dependence of the perturbation in x and y as well as in time is described by $exp[\imath k_x x + \imath k_y y + nt]$. The initially infinitesimal differences from the stationary state increase with time, when nt is not imaginary. At the density discontinuity at z=0 the dispersion relation is given by:

$$n^2 = g_z k \left[\frac{\rho_2 - \rho_1}{\rho_2 + rho_1}\right] \tag{5.28}$$

Therefore the Rayleigh-Taylor Instability occurs for:

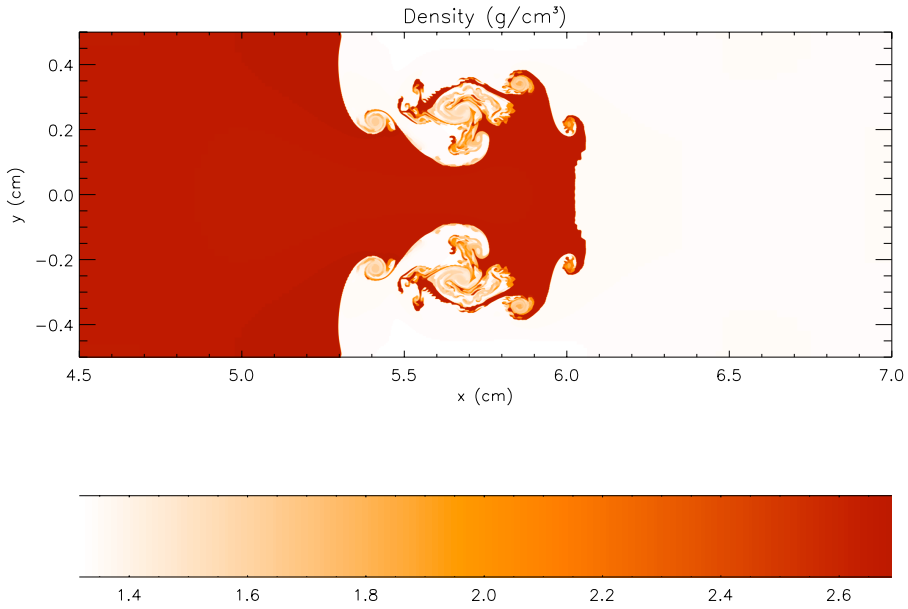

Figure 5.3: Rayleigh-Taylor instability with FLASH2.5 on the Vienna Astro Cluster (32 proc). In the figures above a cutout of the computational domain ($x = [0, 9]$, $y = [-0.6, 0.6]$) after 5s of simulation time is shown. The maximum level of refinement is 6. The density is displayed in color code.

$$\rho_1 > \rho_2 \quad if \quad g_z > 0 \tag{5.29}$$
$$\rho_1 < \rho_2 \quad if \quad g_z < 0 \tag{5.30}$$

Some examples of RT-instabilities are shown in the left panel of Fig. 5.2 and in Fig. 5.3.

Simulating a Rayleigh-Taylor Instability with FLASH2.5. In Fig. 5.3 a wind-tunnel run of two fluids with different densities and velocities is shown. The parameters are initially $p_1 = 1.0$ dyne cm^{-2}, $\rho_1 = 1.4$ g cm^{-3}, $v_1 = 0.5$ cm s^{-1} for the left part of the domain ($y > 0$) and the right part ($y \leq 0$) is parametrised by $p_2 = p_1$, $\rho_2 = 0.8 \cdot \rho_1$, $v_2 = 0$ cm s^{-1}. The initial perturbation is a very flat quarter of a sine wave with an amplitude of 0.05. Density discontinuity at: $0.5 + 0.05 \cdot sin(3\pi y/4y_{max} + 0.5 \cdot \pi)$.

5.5.2 Kelvin - Helmholtz Instability

Kelvin - Helmholtz (KH) instability can occur when velocity shear is present within a continuous fluid or, when there is sufficient velocity difference across the interface between two fluids. The first result is a wave structure on the discontinuity between the two plane parallel layers. As the perturbation grows, the structures are getting much more complex. In Fig. 5.2 the KH instability is produced by the RT instability, since due to that a velocity in y direction is

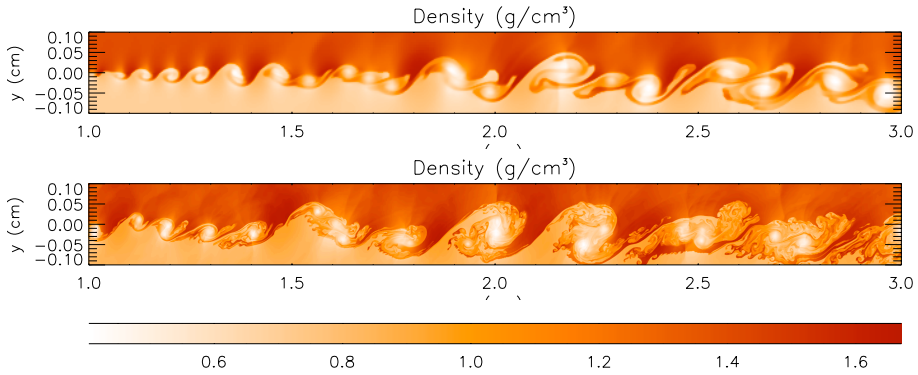

Figure 5.4: Kelvin Helmholtz Instability with FLASH2.5 on the Vienna Astro Cluster (32 proc). In the figures above a cutout of the computational domain ($x = [0, 3]$, $y = [-0.4, 0.4]$) after 4.5s of simulation time is shown. The maximum level of refinement is 4 for the upper panel and 6 for the lower one. The density is displayed in color code.

induced, leading to the required velocity shear between two fluids of different densities. real The analysis of the 3D KH instability is similar to that of the RT instability (see above) but with an additional, time independent velocity field $\vec{V} = (V_x(z), 0, 0)$ again with a gravitational acceleration in z-direction. After the linearisation the hydrodynamic equations for the KH instability are

$$\frac{\partial}{\partial t}(\delta\rho) + V_x \frac{\partial}{\partial x}(\delta\rho) = -\delta v_z \frac{\partial \rho}{\partial z} \tag{5.31}$$

$$\rho\frac{\partial}{\partial t}(\delta v_x) + \rho V_x \frac{\partial}{\partial x}(\delta v_x) + \rho v_z \frac{\partial}{\partial z}(V_x) = -\frac{\partial}{\partial x}(\delta p) \tag{5.32}$$

$$\rho\frac{\partial}{\partial t}(\delta v_y) + \rho V_x \frac{\partial}{\partial x}(\delta v_y) = -\frac{\partial}{\partial y}(\delta p) \tag{5.33}$$

$$\rho\frac{\partial}{\partial t}(\delta v_z) + \rho V_x \frac{\partial}{\partial x}(\delta v_z) = -\frac{\partial}{\partial z}(\delta p) - g_z \delta\rho \tag{5.34}$$

$$\frac{\partial(\delta v_x)}{\partial x} + \frac{\partial(\delta v_y)}{\partial y} + \frac{\partial(\delta v_z)}{\partial z} = 0 \tag{5.35}$$

Again the dependence of the evolution of the perturbation in space and time is described by $exp[\imath k_x x + \imath k_y y + nt]$ and analogous the initially infinitesimal differences from the stationary state increase with time, when n is a real number.

For the special case of

$$\rho = \rho_2 \quad , \quad \vec{V} = \vec{V_2} = (V_2, 0, 0) for z > 0 \tag{5.36}$$

$$\rho = \rho_1 \quad , \quad \vec{V} = \vec{V_1} = (V_1, 0, 0) for z < 0 \tag{5.37}$$

The integration over the density discontinuity leads to the dispersion relation

$$n^2 + 2k_x(\alpha_1 V_1 + \alpha_2 V_2)n + k_x^2(\alpha_1 V_1^2 + \alpha_2 V_2^2) - g_z k(\alpha_1 - \alpha_2) \tag{5.38}$$

with $\alpha_1 = \rho_1/(\rho_1 + \rho_2)$ and $\alpha_2 = \rho_2/(\rho_1 + \rho_2)$
Instability is given for real n and therefore

$$k > \frac{g_z(\alpha_1 - \alpha_2)}{\alpha_1\alpha_2(V_1 - V_2)^2} = k_{min} \tag{5.39}$$

Simulating a Kelvin-Helmholtz Instability with FLASH2.5. In Fig. 5.4 a wind-tunnel run of two fluids with different densities and velocities is shown. The parameters are $p_1 = 1.0$ dyne cm^{-2}, $\rho_1 = 1.4$ g cm^{-3}, $v_1 = 3.0$ cm s^{-1} for the upper layer ($y > 0$) and the lower layer ($y \leq 0$) is parametrised by $p_2 = p_1$, $\rho_2 = 0.5 \cdot \rho_1$, $v_2 = 0.5 \cdot v_1$. The initial perturbation, as in the Rayleigh-Taylor run, is a very flat quarter of a sine wave with an amplitude of 0.025. Density discontinuity at: $0.025 \cdot sin(4x/x_{max})$

5.5.3 Jeans Mass

The investigation of the Jeans instability (after Sir James Jeans) bases on a stable infinite homogeneous fluid with constant density ρ_0 and pressure p_0 and no internal motion and therefore $v_0 = 0$. Euler's equation for fluid motion $\frac{\partial\vec{v}}{\partial t} + (\vec{v}\cdot\bigtriangledown)\vec{v} = -\frac{1}{\rho}\bigtriangledown p - \bigtriangledown\Phi$ for constant ρ_0 and p_0 and without any internal motions read $\bigtriangledown\Phi = 0$. Poisson's equation $\bigtriangledown^2\Phi_0 = 4\pi G\rho_0$ can in this setup only be solved for $\rho_0 = 0$. Nevertheless the Jeans instability provides a good estimate for the gravitational collapse of interstellar gas clouds and subsequent star formation. The fictitious initial assumption is called the Jeans swindle. Within this scenario a sphere of radius r is taken into consideration and perturbed with a small compression from volume V to $(1 - \alpha)$V, where $\alpha << 1$. Whenever the arising gravitational force due to the increasing density is larger than the pressure force working against the compression the system become unstable.

The quantitative analysis of the perturbation (Binney & Tremaine, 1988) uses the linearised fluid equations for the stable parameters $\rho_0 = $ const, $p_0 = $ const, $v_0 = 0$ and therefore, with the Jeans swindle $\Phi_0 = 0$, the perturbed values ρ_1, p_1 and Φ_1 as well as the sound speed $v_s^2 = (dp/d\rho)_{\rho_0}$ and the perturbed specific enthalpy $h_1 = \rho_1/\rho_0(dp/d\rho)_{\rho_0}$

$$\frac{\partial\rho_1}{\partial t} + \rho_0 \bigtriangledown\cdot v_1 = 0 \tag{5.40}$$

$$\frac{\partial v_1}{\partial t} = -\bigtriangledown h_1 - \bigtriangledown\Phi_1 \tag{5.41}$$

$$\bigtriangledown^2\Phi_1 = 4\pi G\rho_1 \tag{5.42}$$

$$h_1 = v_s^2\frac{\rho_1}{\rho_0} \tag{5.43}$$

These equation can be combined to

$$\frac{\partial^2\rho_1}{\partial t^2} - v_s^2 \bigtriangledown^2 \rho_1 - 4\pi G\rho_0\rho_1 = 0 \tag{5.44}$$

and the trial solution is

$$\rho_1(\vec{x}, t) = \int C(\vec{k}e^{i[\vec{k}\cdot\vec{x} - \omega(k)t]}d^3\vec{k} \tag{5.45}$$

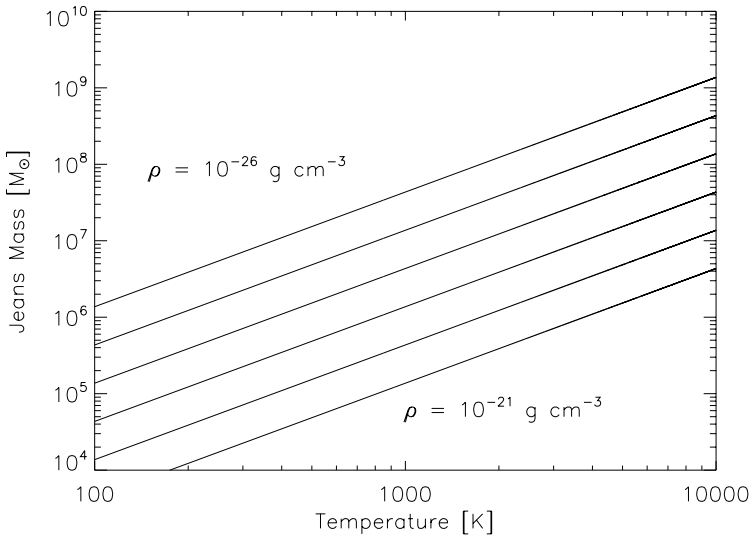

Figure 5.5: The Jeans mass M_J in dependence of the temperature for constant densities from $\rho = 10^{-26} g\,cm^{-3}$ to $\rho = 10^{-21} g\,cm^{-3}$.

with an instability for ρ_1 growing exponentially with time. Together with the dispersion relation

$$\omega^2 = v_s^2 k^2 - 4\pi G\rho_0 \tag{5.46}$$

where k is the wave number and ω is the frequency, the condition for a growing ρ_1 and subsequent an unstable system is

$$k^2 < k_J^2 \equiv \frac{4\pi G\rho_0}{v_s^2} \tag{5.47}$$

where k_J is the Jeans wave-number for the fluid. The Jeans length $\lambda_J = 2\pi/k_J$ is defined as the wavelength corresponding to the wave-number k_J, leading to

$$\lambda^2 > \lambda_J^2 \equiv \frac{\pi v_s^2}{G\rho_0} \tag{5.48}$$

The Jeans mass M_J is the initially enclosed mass in a sphere of diameter λ_J.

$$M_J = \frac{4\pi}{3}\rho_0(\frac{1}{2}\lambda_J)^3 = \frac{1}{6}\pi\rho_0\left(\frac{\pi v_s^2}{G\rho_0}\right)^{3/2} \tag{5.49}$$

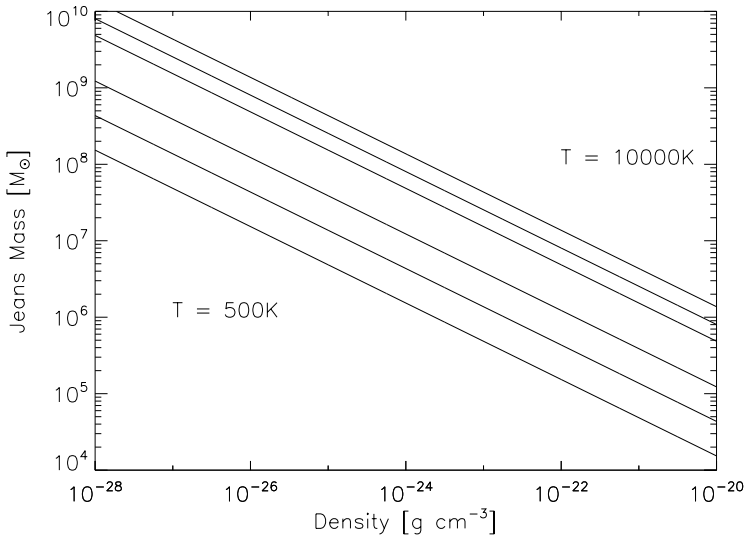

Figure 5.6: The Jeans mass M_J in dependence of the density for constant temperatures of T= 500, 1000, 2000, 5000, 7000 and 10000 K.

Assuming an ideal gas, the sound speed v_s can be determined by $v_{ideal} = \sqrt{\frac{\gamma k_B T_c}{m_H}}$, with $\gamma = 5/3$ and $m_H = 1.6737 \cdot 10^{-24} g$, the mass of a single hydrogen atom. In Fig. 5.5 and 5.6 the temperature and density dependences are shown. For a constant density the Jeans mass is higher if the temperature increases due to the larger gas pressure while for a constant temperature the Jeans mass decreases with larger densities.

5.5.4 Bonnor-Ebert Mass

Ebert (1955) investigated the behavior of HI in the neighborhood of HII regions caused by young O or B stars. The stellar radiation can expand the HII region until a pressure equilibrium with the ambient HI gas is reached. This external pressure can lead to a gravitational collapse of parts of the HI and is therefore a trigger for star formation at the edges of HII regions. Beside plane-parallel layers of HI and HII and a HI cylinder embedded in HII they also looked at the case of spherical symmetric, isothermal HI cloud in a surrounding medium providing an external pressure P_{ext}. While in the first two cases no instability occurs for any external pressure there is a critical pressure P_c for the third case, where for every $P_c < P_{ext}$ the HII region is able to compress the HI cloud in a way, that the cloud collapses under its own gravity. A maximum mass M_{BE} for a HI cloud depending on its temperature and the external pressure of the ambient medium is derived:

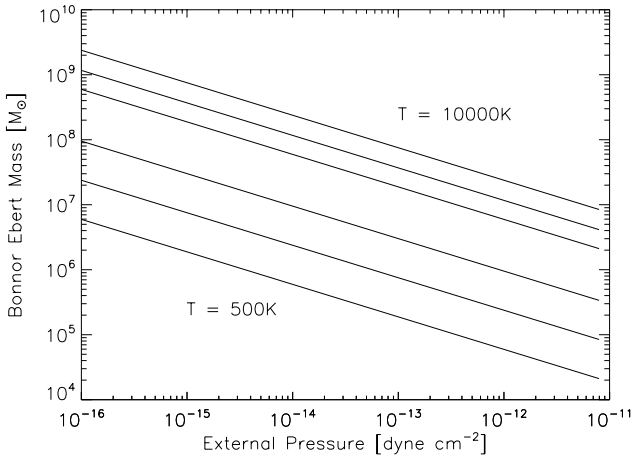

Figure 5.7: The Bonnor-Ebert mass in dependence of the external pressure for constant temperatures of T= 500, 1000, 2000, 5000, 7000 and 10000 K.

$$M_{BE}^2 > 17.6 \frac{(RT_0)^4}{4\pi\mu^4 G^3 P_{ext}} \tag{5.50}$$

where R is the gas constant, G the gravitational constant and μ the molecular weight.

5.5.5 Tidal Radius

The radius r_j is called the Jacobi limit of the mass m, which provides a useful estimate of the system's tidal radius r_t for an orbiting system and is given by Binney & Tremaine (1988) with

$$r_j = \pm D \left[\frac{m}{M(3 + m/M)} \right]^{1/3} \tag{5.51}$$

where M is the mass of the Milky Way, m the mass of the high velocity cloud and D the distance between cloud and galaxy.

Another estimate for the tidal truncation radius was made by Sternberg et al. (2002) as

$$3\bar{n}_{MW}(d) = \bar{n}_C HVC(r_t) \tag{5.52}$$

where $\bar{n}_{MW}(d)$ is the mean density of the Milky Way up to a distance d and $\bar{n}_{CHVC}$ is the mean DM density of the CHVC halo within the truncation radius r_t. In their Galaxy model they assumed $3\bar{n}_{MW} = 2.4 \times 10^{-3}\, cm^{-3}$ at a distance of 150 kpc, leading to a tidal radius of several kpc, for example $r_t = 6.8\, kpc$ for

their $v_s = 12\,km\,s^{-1}$ mini-halo. For typical sizes of CHVCs assuming they are settled in the circumgalactic environment of $r_{CHVC} = 0.5\,kpc$, the CHVCs are not supposed to be tidally disrupted.

5.5.6 Ram Pressure Stripping

An object moving through a fluid faces a drag force, depending on the relative velocity of object and fluid and the density of the streaming matter. Gunn & Gott (1972) investigated the effect of ram pressure stripping of galaxies in the intracluster medium of large galaxy clusters. They compared the ram pressure and the $P_{ram} \approx \rho v^2$ with the object's gravitational restoring force per unit area P_g to get a minimum radius r_{strip} at which the ram pressure is getting too large to keep the gas (or stars) bound. Gunn & Gott (1972) found for P_g:

$$P_g = 2\pi G \Sigma_\star \Sigma_{HI} \tag{5.53}$$

where $\Sigma_\star$ relates to the surface density of the stars within the galaxy and Σ_{HI} refers to the galaxy's interstellar medium. Other authors, as Fujita (1999) describe $\Sigma_\star$ as the gravitational surface mass density, which can be expressed with the rotation velocity v_{rot} of the galaxy: $P_g = v_{rot}^2 R^{-1} \Sigma_{HI}$, where R is the radius of the disk. Rödiger & Hensler (2005) expressed the gravitational surface mass density with the derivative of the gravitational potential in the direction of the galaxy motion $\partial\Phi(r)/\partial z$ and therefore for face-on motions perpendicular to the galactic plane:

$$P_g = \frac{\partial \phi(r)}{\partial z} \Sigma_{gas}(r) \tag{5.54}$$

Mori & Burkert (2000) looked at spherical dwarf galaxies in dark matter halos and found that if the ram pressure exceed the thermal pressure $P_{th} = \rho_{g0} k_B T/(\mu m_p)$ at the center of the CDM gravitational potential the gas it totally stripped out of the dark matter halo. ρ_{g0} is the central density of the gas, m_p is the proton mass and T is expressed by a constant temperature in hydrostatic equilibrium $T = \frac{\mu m_p}{3 k_B} \frac{G M_0}{r_0}$. Therefore the condition for total gas stripping reads

$$\rho_{ICM} v_{ICM}^2 > \frac{G M_0 \rho_{g0}}{3 r_0} \tag{5.55}$$

where M_0 is the is the dark matter mass within the CDM core radius r_0. Furthermore a maximum core mass for total stripping can be calculated with

$$M_0 < 1.27 \times 10^9 \left(\frac{F}{0.1}\right)^{-7/2} \left(\frac{n_{ICM}}{10^{-4} cm^{-3}}\right)^{7/2} \times \left(\frac{v_{ICM}}{10^3 km\,s^{-1}}\right)^7 M_\odot \tag{5.56}$$

where F refers to the fraction of gas to dark matter mass within the core radius r_0.

Sternberg et al. (2002) base on the relation found by Gunn & Gott (1972) and found for neutral clouds with a velocity v through the hot halo gas stripping for

$$\left(\frac{n_{HIM}}{10^{-4}\,cm^{-3}}\right) > 4.4\left(\frac{\Sigma_{DM}}{10^{7}\,M_{\odot}kpc^{-2}}\right)\left(\frac{N_{HI}}{10^{20}\,cm^{-2}}\right)\times\left(\frac{v}{100\,km\,s^{-1}}\right)^{-2} \quad (5.57)$$

with n_{HIM} is the particle density of the surrounding hot halo gas, Σ_{DM} the DM surface density, N_{HI} the HI column density and v the cloud velocity.

In addition to the so-called instantaneous stripping discussed above, where the outer parts of the moving object are stripped away down to the stripping radius r_{strip} on short time-scales, there are other effects of mass loss, like the continuous stripping occurring at the boundaries of the object, driven by turbulence like the Kelvin-Helmholtz instability. This process happens on a relatively large time-scale which separates the evolution of the stripped object in an instantaneous and a continuous stripping phase. Nulsen et al. (1982) calculated the maximum mass loss for a sphere of radius R, moving through a medium of density n_{ICM} with a velocity v_{ICM} for the continuous stripping as

$$\dot{M} \approx 20\left(\frac{R}{20\,kpc}\right)^{2}\left(\frac{n_{ICM}}{10^{-3}cm^{-3}}\right)\left(\frac{v_{ICM}}{1000km\,s^{-1}}\right)\frac{M_{\odot}}{yr} \quad (5.58)$$

5.6 Thermal Processes

5.6.1 Cooling

In this simulation a combination of the cooling function by Böhringer & Hensler (1989), for temperatures above 10^4 K and Slyz et. al (2005) for temperatures below 10^4 K is used. The energy loss due to radiative cooling is given by

$$\frac{\partial\epsilon}{\partial t} = -n^2\Lambda(T) \quad (5.59)$$

where n is the particle density and $\Lambda(T)$ is the cooling function in dependence of the temperature T.

Slyz et al. (2005) for $T < 10^4\,K$: The cooling rate $\Lambda(T)$ is parametrized by the factor $C_{i,i+1}$ and the exponent $\beta_{i,i+1}$ for the temperature range between T_i and T_{i+1}.

$$\Lambda(T) = C_{i,i+1}T^{\beta_{i,i+1}} \quad (5.60)$$

i	T_i [K]	$C_{i,i+1}$ ergs $s^{-1}g^{-2}cm^3K^{-\beta_{i,i+1}}$	$\beta_{i,i+1}$
1	10	2.1507×10^{-27}	2.120
2	310	2.2380×10^{-32}	2.000
3	2000	1.0012×10^{-30}	1.500
4	8000	4.6240×10^{-36}	2.867
5	39811	3.1620×10^{-30}	1.600

Table 5.1: Slyz et al. (2005) parameters of their cooling function.

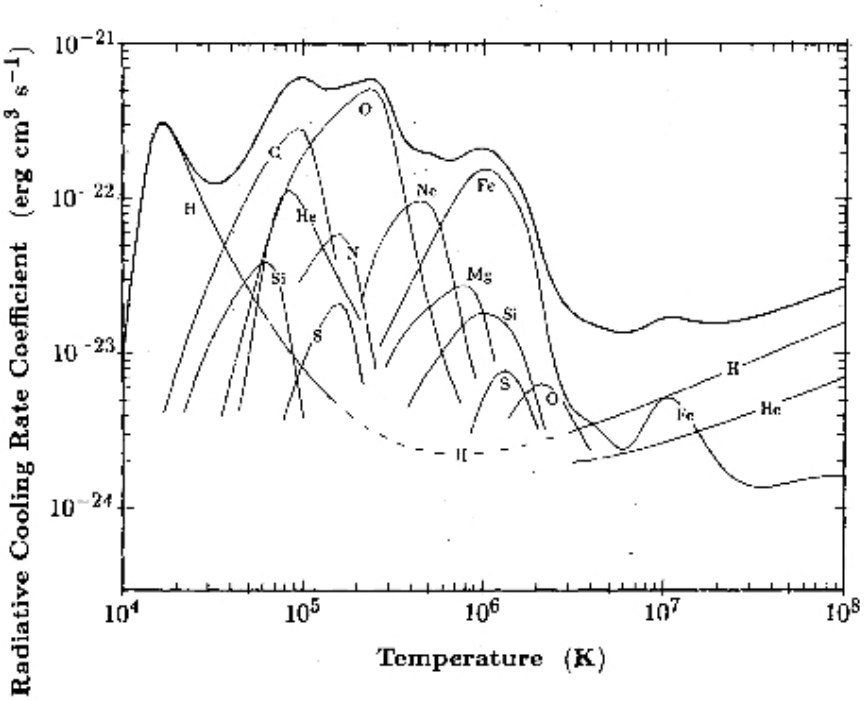

Figure 5.8: Contributions of different elements to the cooling rate. Figure from Böhringer & Hensler (1989).

The single values of $C_{i,i+1}$ and $\beta_{i,i+1}$ for different temperature ranges can be found in table 5.1 and the plotted function in 5.9. The resulting cooling function is a simplified form of the Wolfire et al. (1995) (hereafter WHMTB) standard equilibrium $P-\rho$ curve, assuming a constant background heating rate per unit mass of $\Gamma_0 = 0.015$ ergs $s^{-1}g^{-1}$. WHMTB included the photoelectric heating from polycyclic aromatic hydrocarbons (PAHs) as a dominating heating process in the warm neutral phase and the cold neutral phase. Since the heating function is only slightly depending of density in the density range of interest, the approximation of a constant heating rate should be sufficiently accurate for our simulation. The cooling processes taken into account by WHMTB and therefore - in a reduced way - in this model are cooling due to collisional excitation of fine-structure lines (C II 158 μm and O I 63 μm, dominant for $T \leq 8000\,K$), fine structure transitions of the ground electronic state of C I, Si I, Si II, S I, Fe I, and Fe II, and electron recombination onto positively charged grains and PAHs (for $T \geq 10^4\,K$).

Böhringer & Hensler (1989) for $T > 10^4\,K$: Böhringer & Hensler (1989) investigated the radiative cooling processes in the hot medium for temperatures between 10^4 and 10^8 K. They focus on the effect of different metallicities and the contribution of the 10 most dominant elements to the total cooling function. A table for H, He, C, N, O, Ne, Mg, Si, S and Fe cooling is available and can be combined for the required composition. In Fig. 5.8 the total cooling function

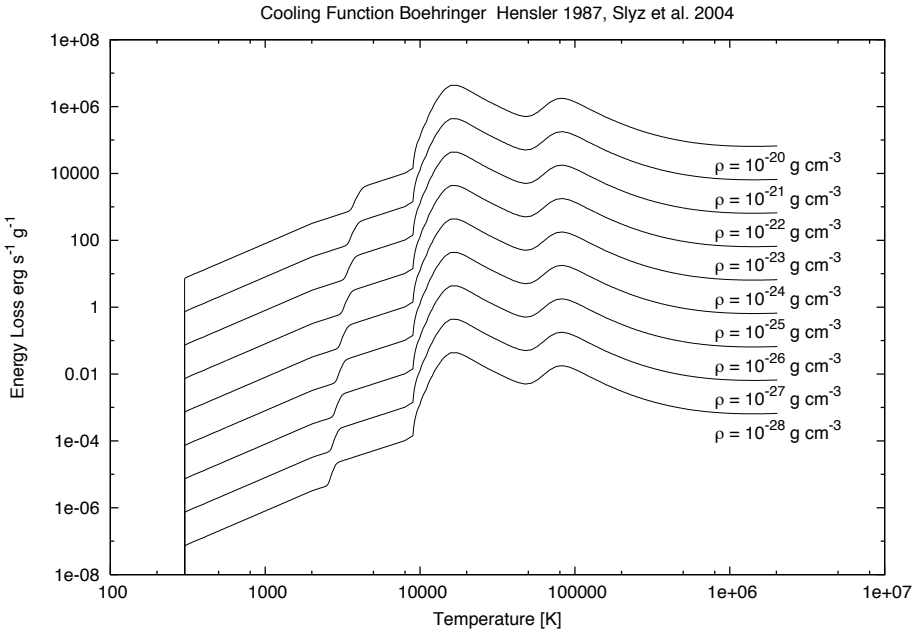

Figure 5.9: Energy loss due to the cooling function by Slyz et al. (2005) for $T < 10^4\,K$ and Böhringer, Hensler (1987) for $T > 10^4\,K$ for different densities. No cooling for temperatures below 310 K.

as the sum of the 10 elements listed above for solar metallicity is shown. Since the HVCs have sub-solar metallicities, the expected dominant cooling features are the H peak at $T \approx 2 \times 10^4\,K$ and the He peak at $T \approx 8 \times 10^4\,K$.

5.6.2 Heating

Different processes in the interstellar medium lead to different heating rates of the cloud and the surrounding ambient hot gas. The energy gain due to the heating rate is given by

$$\frac{\partial \epsilon}{\partial t} = n\Gamma(T) \tag{5.61}$$

where n is the particle density and $\Gamma(T)$ is the total heating function in dependence of the temperature T. Included in this simulation are the following processes based on the work by Vieser (2001):

Thermalisation of turbulent motions: Due to viscosity forces the kinetic energy can be converted into thermal energy in turbulent regions . The accurate conversion factor is not well known but the heating rate is given by Falgarone et al. (1992) with:

$$\Gamma_\eta = 7 \cdot 10^{-28} n_H ergcm^{-3} s^{-1} \tag{5.62}$$

Cosmic Rays: The cosmic rays' primary ionization of neutral gas leads to an enhancement of free electrons between 5.7 and 7.3 eV (Cravens & Dalgarno

1978) in the gas. A primary ionization rate of $\zeta_p = 4 \cdot 10^{-17}\, s^{-1}$ (Black 1987) gives a heating rate of

$$\Gamma_{cr,n} = 9 \cdot 10^{-12} \zeta_p (n_H + n_{H_2}) erg cm^{-3} s^{-1} \tag{5.63}$$

Since the fraction of H_2 is negligible in the given conditions the equation is modified with the given value of ζ_p to:

$$\Gamma_{cr,n} = 3.6 \cdot 10^{-28} n_H \, erg \, cm^{-3} \, s^{-1} \tag{5.64}$$

The heating rate is more efficient when the gas is mostly ionized because the many free electrons can interact directly with the cosmic radiation and in addition the primary electron can interact more often with the free electrons and transmit the energy that way, the following correction for a ionized medium with the level of ionization f has to be done.

$$\Gamma_{cr} = (1 - f)\Gamma_{cr,n} + f\Gamma_{cr,i} \tag{5.65}$$

with

$$\Gamma_{cr,i} = (2 \cdot 10^{-27}(1 - f) + 2 \cdot 10^{-26} f) n_H \, erg \, cm^{-3} \, s^{-1} \tag{5.66}$$

X - Rays: Similar consideration to that corresponding to the cosmic rays lead to the heating rate due to x-radiation. However in this case a increased heating rate in ionized areas are not taken into account since the interaction between the x-ray photons and the free electrons is negligible (Dalgarno & McCray 1972). The heating rate for x-radiation is determined by Scheffler & Elsässer (1992) with:

$$\Gamma_x = (1 - f)\Gamma_{cr,n} + f(1 - f) 2 \cdot 10^{-27} n_H \, erg \, cm^{-3} \, s^{-1} \tag{5.67}$$

Dust Heating: For temperatures below $10000\, K$ heating is dominated by the photoelectric effect on dust particles. The corresponding heating rate was calculated by de Jong (1977) as follows:

$$\Gamma_{pe} = 7.5 \cdot 10^{-25} y\chi (n_H + 2n_{H_2}) \frac{(1 - x_d)^2}{x_d + 2\gamma} erg cm^{-3} s^{-1} \tag{5.68}$$

where y describes the number of released electrons per photon, x_d is the required energy in units of $13.6\, eV$ and χ is dependent of the EUV filed, standardized on the value by Habing (1968).

$$\gamma = 2.9 \cdot 10^{-4} \frac{y\chi\sqrt{T}}{n_e} \tag{5.69}$$

5.6.3 Heating and Cooling Equilibrium

The deviation of the thermal energy ϵ in time is given by the sum of the energy gain due to heating processes and the energy loss due to radiative cooling

$$\frac{\partial \epsilon}{\partial t} = n\Gamma(T) - n^2 \Lambda(T) \tag{5.70}$$

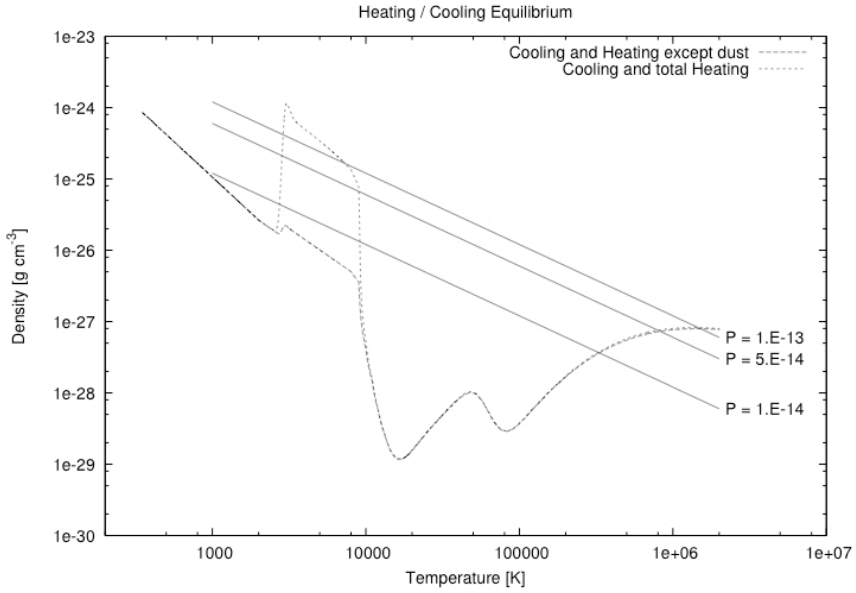

Figure 5.10: Equilibrium function for heating and cooling processes with iso-pressure lines to estimate the different gas phases that can occur for pressure equilibrium.

where n is the particle density, $\Gamma(T)$ is the total heating function and $\Lambda(T)$ the total cooling function, both in dependence of the temperature T. For a thermally stable configuration the time derivative has to vanish and therefore:

$$n\Gamma(T) = n^2\Lambda(T) \tag{5.71}$$

In Fig. 5.10 the equilibrium function for the included heating and cooling processes are shown. One of the most obvious features is the peak due to dust heating in the temperature range between 3000 K and 7000 K. Also plotted are iso-pressure lines to get an idea about the thermally stable phases in pressure equilibrium. Assuming a hot phase with temperatures between $T_{HIM} = 1 \times 10^6\,K..2 \times 10^6\,K$ lead to densities for which thermal equilibrium is reached between $\rho_{HIM} = 10^{-27}..2 \times 10^{-27}\,g\,cm^{-3}$ correlating to particle densities of $n_{HIM} = 6 \times 10^{-4} - 1.2 \times 10^{-3}\,cm^{-3}$. Following the iso-pressure lines to smaller temperatures and therefore larger densities, the warm phase can be found between temperatures of $T_{WNM} = 6000..9000\,K$ and with a larger density range of $\rho_{WNM} = 10^{-26}..2{\times}10^{-25}\,g\,cm^{-3}$ ($n_{WNM} = 6{\times}10^{-3}..1.2{\times}10^{-1}\,cm^{-3}$). A thermally stable cold phase is reached for temperatures of a few hundred K and densities of $\rho_{CNM} = 10^{-25}..10^{-24}\,g\,cm^{-3}$ ($n_{CNM} = 0.1..1\,cm^{-3}$). Note that a warm phase in pressure equilibrium with the HIM would not be possible without the heating due to dust extinction, which is the dominant heating process for $T < 10000\,K$. In Fig. 5.10 the equilibrium curve separates the $T - \rho$ domain in two regions, where in the part with densities higher than the equilibrium density the cooling is dominant while in the other part the heating dominates the cooling function. For regions where $d\rho/dT < 0$ a small tempera-

ture perturbation at a constant density is balanced on a very short time-scale. For example increasing the temperature from $T = 1000\,K$ to $T = 1000 + \delta T$ with $\delta T > 0$ leads to an area of dominant cooling and therefore a temperature drop until the thermal equilibrium is reached. Thermal instability occurs for $d\rho/dT > 0$ since for a larger temperature the region with dominant heating and the other way round for smaller temperatures. For the included heating and cooling processes thermal instability happens for temperature ranges between $T = 3000 - 4000\,K, 12000 - 15000\,K, > 80000\,K$. A 3-phase medium was proposed by McKee & Ostriker (1977) for the interaction of supernova remnants with cloudy structure of the interstellar medium in the disk. They found the following stable gas phases with temperatures T, particle densities n and ionization fractions x (with x=1 refers to a fully ionized medium) :

- HIM (hot ionized medium): $T = 4.5 \times 10^5\,K$, $n = 3.5 \times 10^{-3}\,cm^{-3}$, $x = 1.0$
- WIM (warm ionized medium): $T = 8000\,K$, $n = 0.25\,cm^{-3}$, $x = 0.68$
- WNM (warm neutral medium): $T = 8000\,K$, $n = 0.37\,cm^{-3}$, $x = 0.15$
- CNM (cold neutral medium): $T = 80\,K$, $n = 42\,cm^{-3}$, $x = 10^{-3}$

Chapter 6

Results

6.1 Overview

This section provides a overview of all runs, which are separated in two different test series. The tables 6.1 and 6.2 give a summary of the applied parameters, namely the temperature of the ambient medium, the cloud radius, the halo radius, the halo core radius and the streaming velocity. In addition, the included processes like self-gravity (igrav), cooling (icool), heating (iheat) and the dark matter halo (ihalo) are listed, where 0 means that this process is not included in this run, while 1 is the marker for included processes. Since the initial distribution of a cloud differs if it is embedded in a dark matter mini-halo or not, the parameter ihalo_init is invented to allow for a better comparison between the runs with and without an additional gravitational potential. If ihalo_init = 1 the initial distribution of the gas cloud is calculated as if the cloud would have a dark matter mini halo, although ihalo=0. In this case, the cloud would not be stable over 100 Myrs but for streaming velocities of 100 to $300\,km\,s^{-1}$ the ram pressure dominates the self-gravity of the cloud and the small gravitational instability of the cloud on a larger time-scale is negligible. In addition to the run parameters, also derived parameters can be found in the tables, like the density of the HIM, that is derived from the heating and cooling equilibrium function, the central density and temperature of the cloud, the cloud mass and the derived parameters for the dark matter halo, the central DM density and the halo mass.

For each run, the results are shown as the temperature and density distributions after 0, 50, 75 and 100 Myrs of simulation time. The computational domain for the runs is $3.75 \times 10^{22}\,cm \times 3.75 \times 10^{22}\,cm$ (12.15 kpc × 12.15 kpc) but only a zoom-in is shown in the following figures. The most obvious features in all runs with thermal processes (icool = iheat = 1) are cold dense cores in the front part of the cloud. These cores arise from the ram pressure region where a over-density is created and therefore the cooling dominates the heating since the energy loss is proportional to n^2 while the energy gain increases only linear with the particle density n. Without any thermal processes (icool = iheat = 0) the observed core/envelope structure can not be reproduced.

Table 6.1: Simulation Run Overview: Test Series 1

	Run Nr.			
	1	2	3	4
Free Parameter:				
Temperature HIM [10^6 K]	1	1	1	1
Cloud Radius [pc]	300	300	300	300
Halo Radius [pc]	500	500	500	600
Halo Core Radius (R_0) [pc]	200	200	200	200
Velocity [cms^{-1}]	2×10^7	2×10^7	2×10^7	2×10^7
Simulation Parameter:				
igrav	1	1	1	0
icool	0	1	1	1
iheat	0	1	1	1
ihalo	0	0	1	1
ihalo_init	1	0	1	1
Derived Parameter:				
Density HIM [gcm^{-3}]	8.014×10^{-28}	8.014×10^{-28}	8.014×10^{-28}	8.014×10^{-28}
Central Density Cloud [gcm^{-3}]	1.942×10^{-25}	9.433×10^{-26}	1.943×10^{-25}	1.943×10^{-25}
Central Temperature Cloud [K]	6.748×10^3	8.629×10^3	6.746×10^3	6.746×10^3
Mass Cloud [$M_\odot$]	1.819×10^5	1.557×10^5	1.820×10^5	1.820×10^5
Central Density DM Halo	0	0	8.908×10^{-24}	8.908×10^{-24}
Mass DM Halo [$M_\odot$]	0	0	6.961×10^6	8.516×10^6

	Run Nr.			
	5	6	7	
Free Parameter:				
Temperature HIM [10^6 K]	2	1.5	1	
Cloud Radius [pc]	300	300	300	
Halo Radius [pc]	750	500	500	
Halo Core Radius (R_0) [pc]	300	200	200	
Velocity [cms^{-1}]	3×10^7	2×10^7	2×10^7	
Simulation Parameter:				
igrav	1	1	1	
icool	1	1	1	
iheat	1	1	1	
ihalo	1	1	0	
ihalo_init	1	1	1	
Derived Parameter:				
Density HIM [gcm^{-3}]	7.971×10^{-28}	8.233×10^{-28}	8.014×10^{-28}	
Central Density Cloud [gcm^{-3}]	1.009×10^{-24}	1.003×10^{-24}	1.943×10^{-25}	
Central Temperature Cloud [K]	3.100×10^3	3.151×10^3	6.746×10^3	
Mass Cloud [$M_\odot$]	4.775×10^5	4.544×10^5	1.820×10^5	
Central Density DM Halo	0	8.908×10^{-24}	0	
Mass DM Halo [$M_\odot$]	0	6.961×10^6	0	

Table 6.2: Simulation Run Overview: Test Series 2

	Run Nr.			
	8	9	10	11
Free Parameter:				
Temperature HIM [10^6 K]	1	1	1	1
Cloud Radius [pc]	300	300	300	300
Halo Radius [pc]	750	500	500	500
Halo Core Radius (R_0) [pc]	300	200	200	200
Velocity [cms^{-1}]	2×10^7	1×10^7	1×10^7	3×10^7
Simulation Parameter:				
igrav	1	1	1	1
icool	1	1	1	1
iheat	1	1	1	1
ihalo	1	1	0	1
ihalo_init	1	1	1	1
Derived Parameter:				
Density HIM [gcm^{-3}]	8.014×10^{-28}	8.014×10^{-28}	8.014×10^{-28}	8.014×10^{-28}
Central Density Cloud [gcm^{-3}]	2.325×10^{-25}	1.943×10^{-25}	1.943×10^{-25}	1.943×10^{-25}
Central Temperature Cloud [K]	6.162×10^3	6.746×10^3	6.746×10^3	6.746×10^3
Mass Cloud [$M_\odot$]	1.952×10^5	1.820×10^5	1.820×10^5	1.820×10^5
Central Density DM Halo	6.798×10^{-24}	8.908×10^{-24}	0	8.908×10^{-24}
Mass DM Halo [$M_\odot$]	1.793×10^7	6.961×10^6	0	6.961×10^6

	Run Nr.			
	13	14	15	
Free Parameter:				
Temperature HIM [10^6 K]	1	1	1.5	
Cloud Radius [pc]	300	300	300	
Halo Radius [pc]	500	750	750	
Halo Core Radius (R_0) [pc]	200	300	300	
Velocity [cms^{-1}]	3×10^7	3×10^7	3×10^7	
Simulation Parameter:				
igrav	1	1	1	
icool	1	1	1	
iheat	1	1	1	
ihalo	0	1	1	
ihalo_init	1	1	1	
Derived Parameter:				
Density HIM [gcm^{-3}]	8.014×10^{-28}	8.014×10^{-28}	8.233×10^{-28}	
Central Density Cloud [gcm^{-3}]	1.943×10^{-25}	2.325×10^{-25}	1.099×10^{-24}	
Central Temperature Cloud [K]	6.746×10^3	6.162×10^3	3.100×10^3	
Mass Cloud [$M_\odot$]	1.820×10^5	1.952×10^5	4.779×10^5	
Central Density DM Halo	0	6.798×10^{-24}	6.798×10^{-24}	
Mass DM Halo [$M_\odot$]	0	1.793×10^7	1.793×10^7	

6.2 Data Correction

The current chapter deals with the question if a DM halo can provide a special velocity structure, as observed in some HVCs with head-tail structure. One dimensional cuts following the x-axis through the clouds are made to compare the simulation with the observations. Since the resolution of the simulation is quite high and beside the innermost core, turbulent dynamical processes of the low-density ambient medium and the cloud gas occur, at some places of y=0 not the velocity of the cloud gas is taken into account but the velocity of the hot halo gas (see Fig. 6.1). This is contrary to the observations, where only the velocities of the high column density HI gas are measured (see Fig. 2.14).

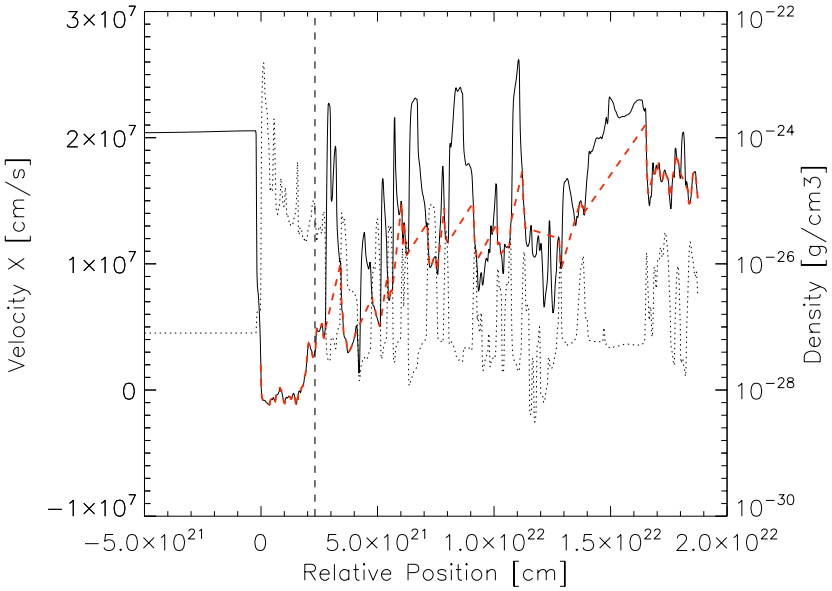

Figure 6.1: Run Nr. 8 after 100 Myrs: Uncorrected x-velocity (left y-axis, solid line) and density (right y-axis, dotted line) 1D distribution. The cut is located at the x-axis in the original 2D plot. Note that the peaks in the velocity are in almost perfect agreement with the low density gas of the ambient medium. The red dashed line relates to the velocity distribution, where only the velocities of regions with densities larger than $\rho_{min} = 3 \times 10^{-27}\, g\, cm^{-3}$ are taken into account. The black dashed line indicates the edge of the dark matter mini halo.

6.3 Effect of self-gravity on/off (Run 7 vs. Run 4)

The differences in the initial distributions between clouds with and without self-gravity are explained in Sec. 5.1.2. In Fig. 6.2 the results of runs without self-gravity, with self-gravity and with self-gravity and an additional gravitational potential after 100 Myrs of simulation time can be found. The ram pressure leads to an enhanced density in the front part of the cloud which starts to cool because of the n^2 dependence of the energy loss due to radiative cooling. Both, the run with self-gravity and the run without show a finger-like structure occurring from the inital ram pressure exposed area of the cloud. The beginning of the formation of these fingers is visible in the plot of the x-velocity distribution after 50 Myrs (Fig. 6.3) and their growth is well explained by the Rayleigh-Taylor instability (see Sec. 5.5.1). The difference in the position of $\Delta r \approx 5 \times 10^{21}\, cm$ in 100 Myrs leads to a velocity decrease of $\Delta v = 16\, km\, s^{-1}$. In Fig. 6.3 and Fig. 6.4 the x-velocity distributions in 2D (color coded) and 1D can be found for runs with igrav=0 and igrav=1. Contrary to the stable clouds where the self-gravity is a very dominant process, the differences between the runs with and without self-gravity for streaming velocities of $200\, km\, s^{-1}$ are not very obvious. Both the morphologic appearance and the 1D data analysis of the x-velocity show similarities. The most prominent differences are the beginning of the formation of an additional finger and a much more extended gas enhancement between $x = 1.8 \times 10^{21}\, cm$ and $x = 1.1 \times 10^{22}\, cm$ in the run without self-gravity after 100 Myrs. Both runs cannot reproduce the head-tail structure observed for several compact high velocity clouds.

Run Nr. 4: Without self-gravity and without DM halo

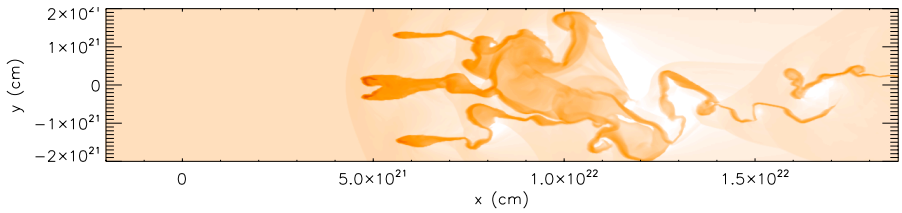

Run Nr. 7: With self-gravity and without DM halo

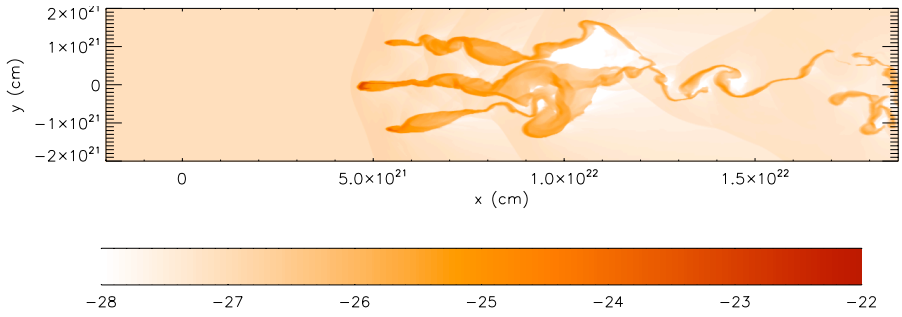

Figure 6.2: Log density distributions, each after 100 Myrs

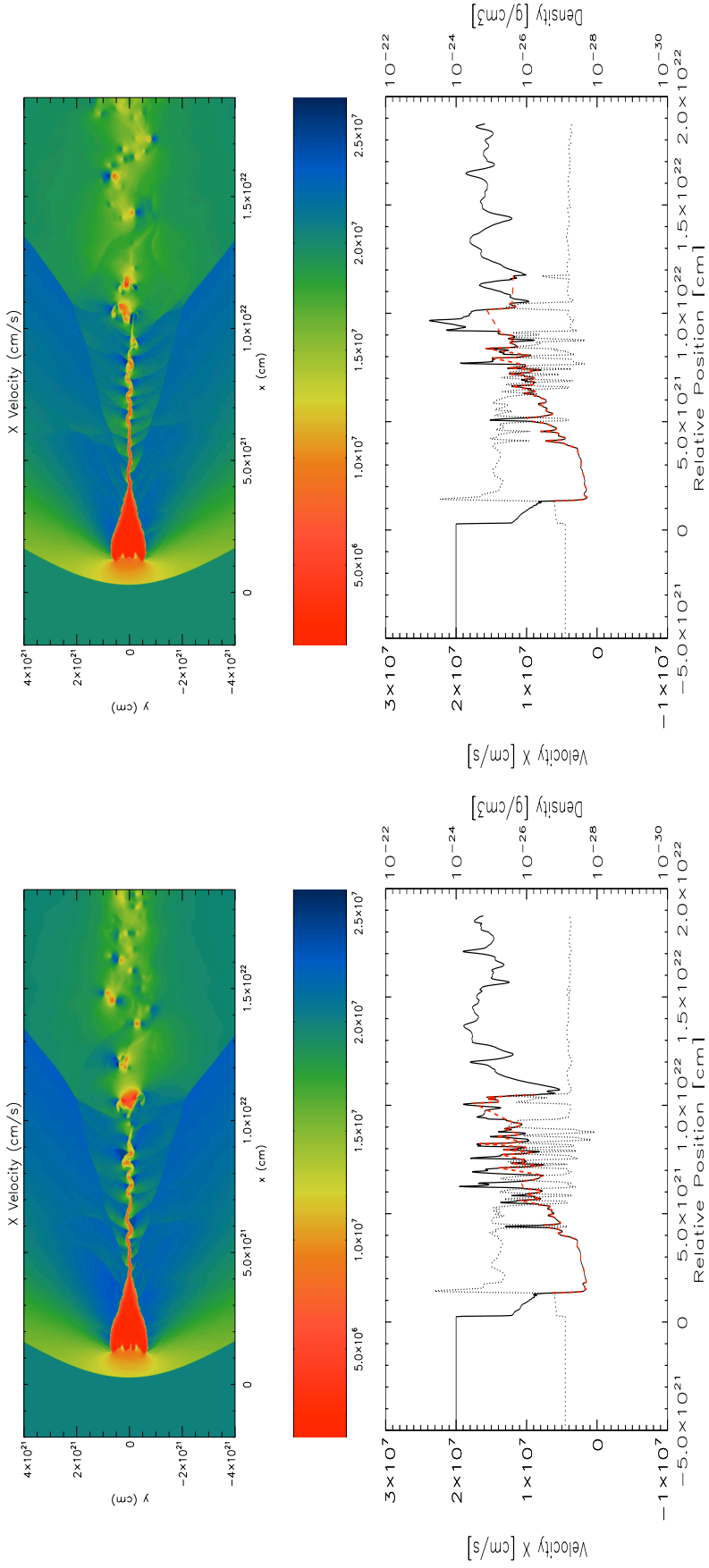

Figure 6.3: Run 4 (left panels, without self-gravity) vs. Run 7 (right panels, with self-gravity) after 50 Myrs. Fig. 6.3 and Fig. 6.4: The upper panels show the 2D x-velocity distribution in color code, while the lower panels describe both the x-velocity and density distribution along the x-axis as explained in Fig. 6.1.

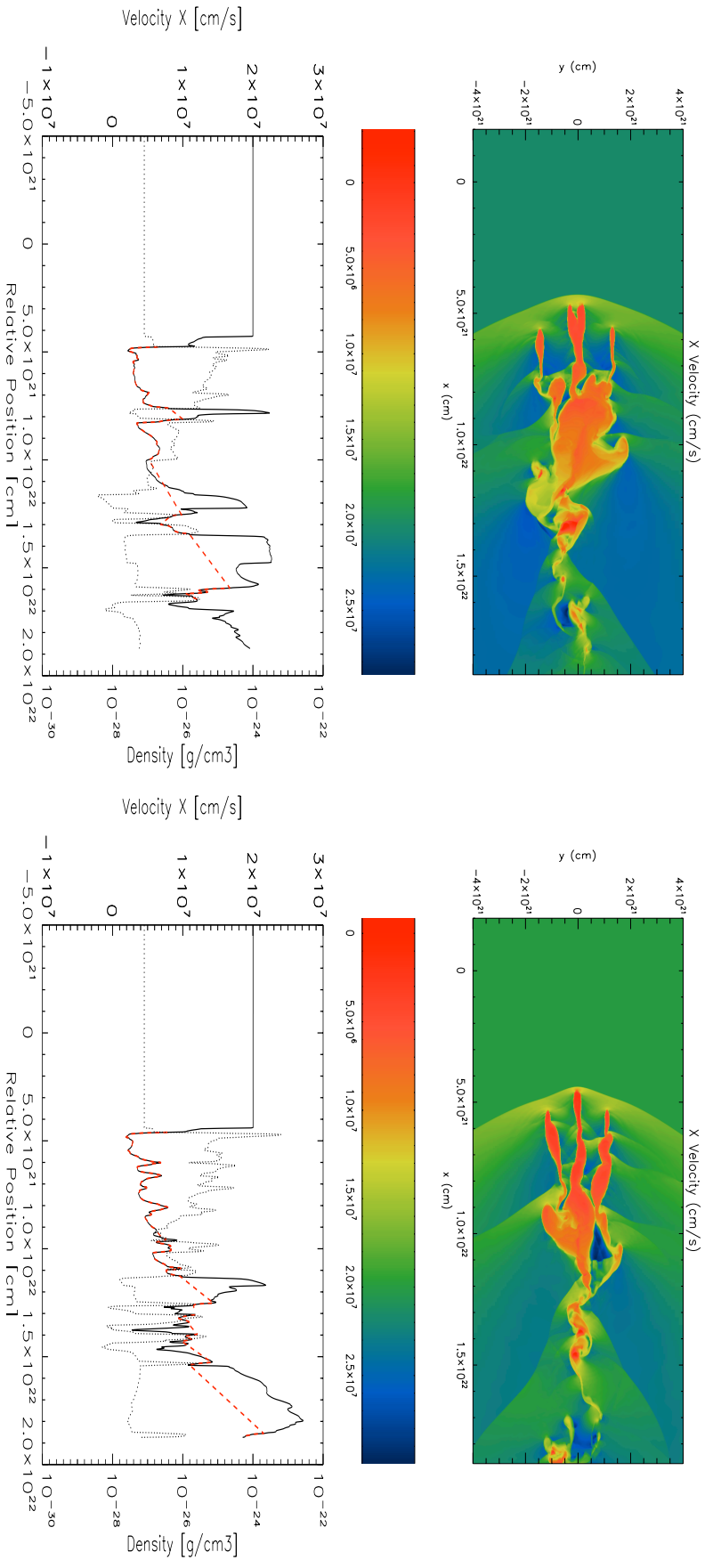

Figure 6.4: Run 4 (left panels, without self-gravity) vs. Run 7 (right panels, with self-gravity) after 100 Myrs.

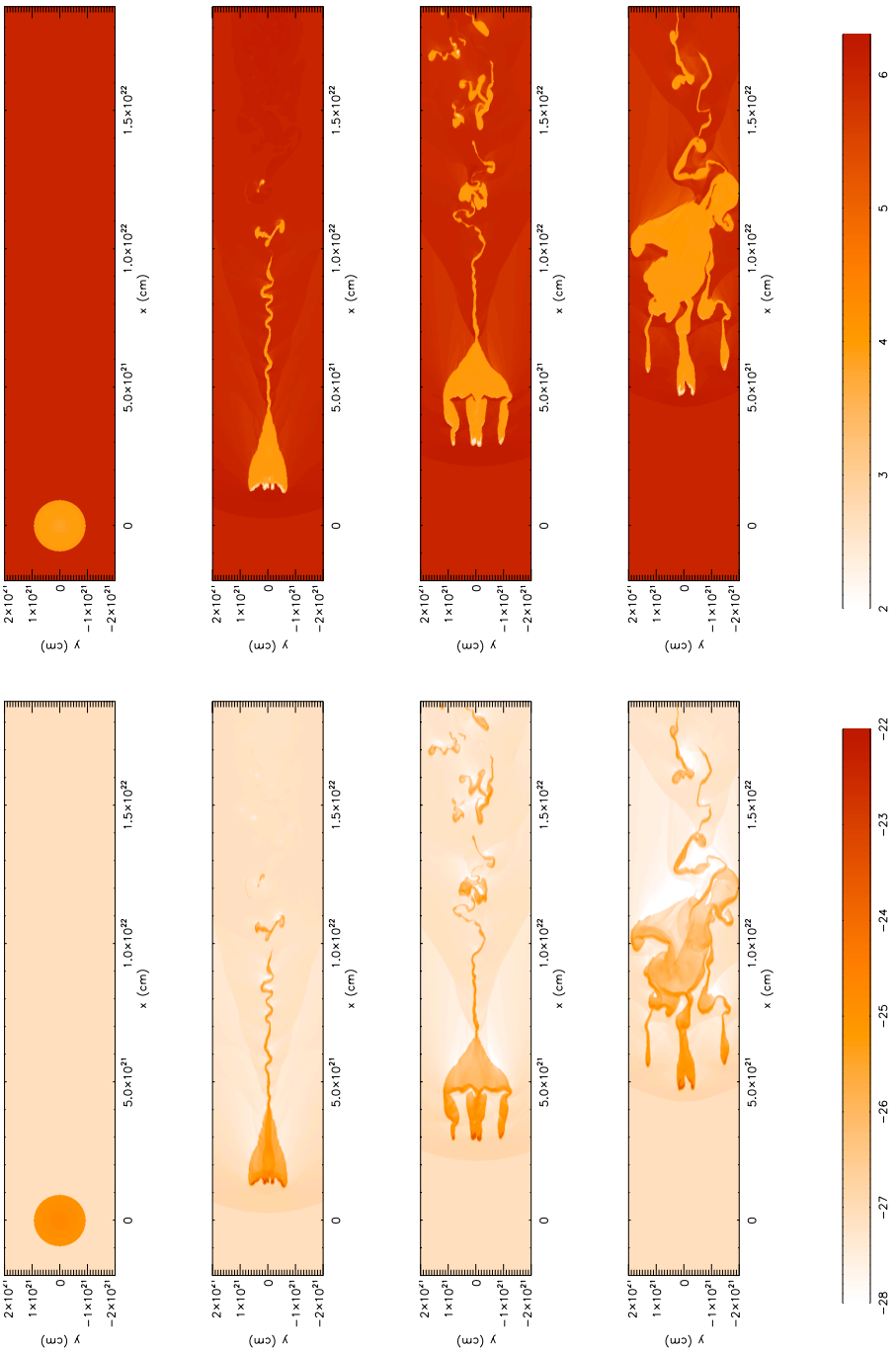

Figure 6.5: Streaming velocity = 200 km/s: Run 4 (without self-gravity): Time dependent evolution of temperature (upper panels) and density (lower panels) after 0, 50, 75 and 100 Myrs (from left to right). Color codes as in the corresponding color bars on the right.

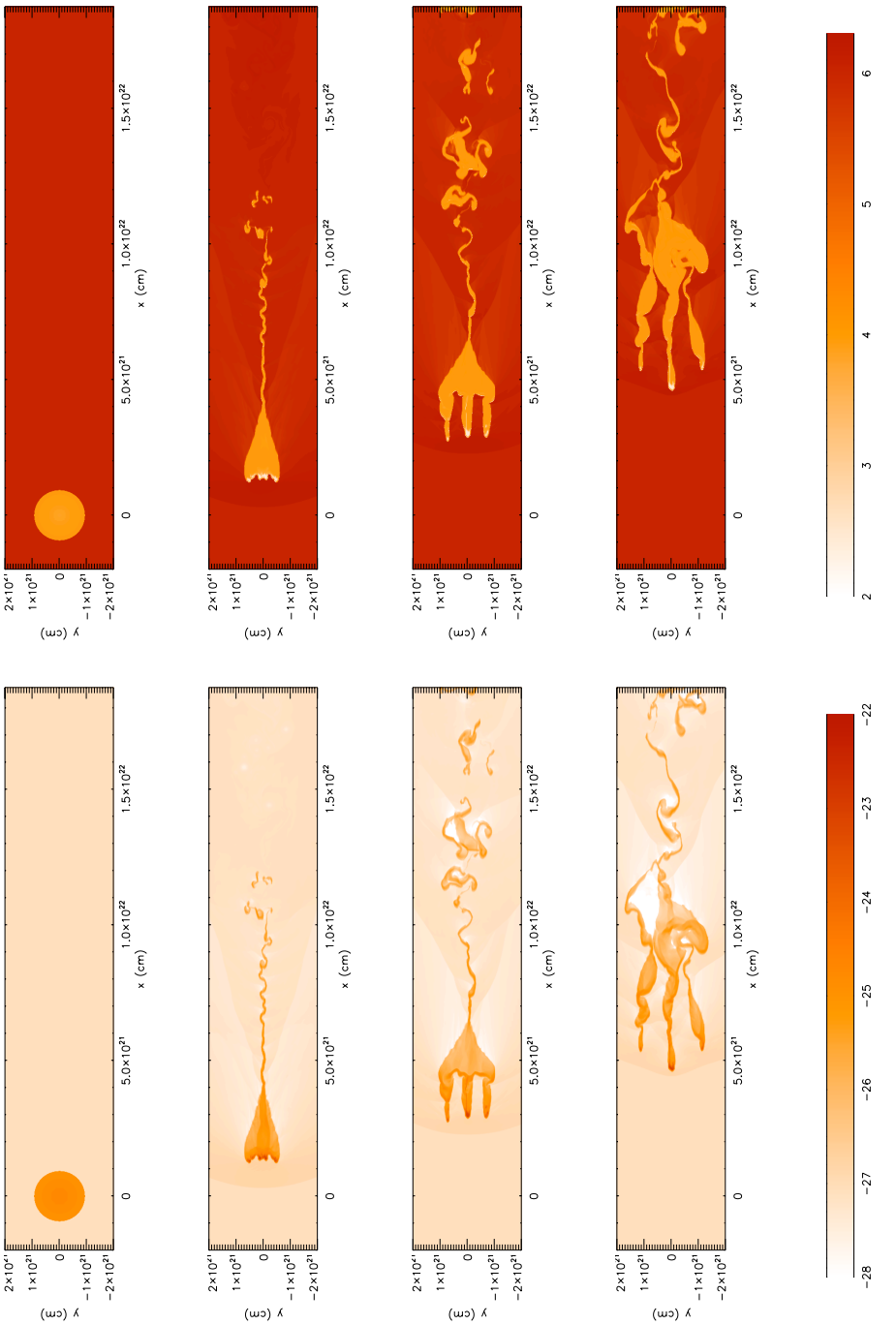

Figure 6.6: As in Fig. 6.5, but for Run 7 (with self-gravity).

6.4 Effect of DM halo (Run 7 vs. Run 3 and Run 2 vs. Run 8)

Adding a dark matter potential to the potential of the gas cloud does not only effect the dynamics of the gas, but also the initial setup of the cloud. Since the cloud is not supposed to collapse and form stars or get too diffuse to be detectable within the simulated time of 100 Myrs the cloud should be stable within this time-scale. The differences of the initial setups of clouds with and without dark matter halo can be found in Fig. 6.8 and Fig. 6.9. For both cases the required pressure equilibrium for the cloud is fulfilled but the intrinsic distribution of temperature, density, pressure and enclosed mass differ in a decisive way. Another important fact is that the dark matter potential provides a force that is counteracting to the occurring ram pressure. While the ram pressure decelerates the cloud which is visible in a motion in the direction of the streaming velocity, the gravitational potential leads to a motion in the direction of the center of the gravitational potential, which is in that case directed opposite to the streaming velocity for most of the gas. The x-position of the cloud after 50 Myrs for a setup with DM and another one without DM together with the x-velocity can be seen in Fig. 6.7 after 50 Myrs. From Fig. 6.10 to Fig. 6.13 the x-velocity of runs which differ only in the simulation parameter ihalo is shown. Both the two dimensional v_x distribution after 50 and 100 Myrs and 1D cuts with the data correction explained in Sec. 6.2 are shown.

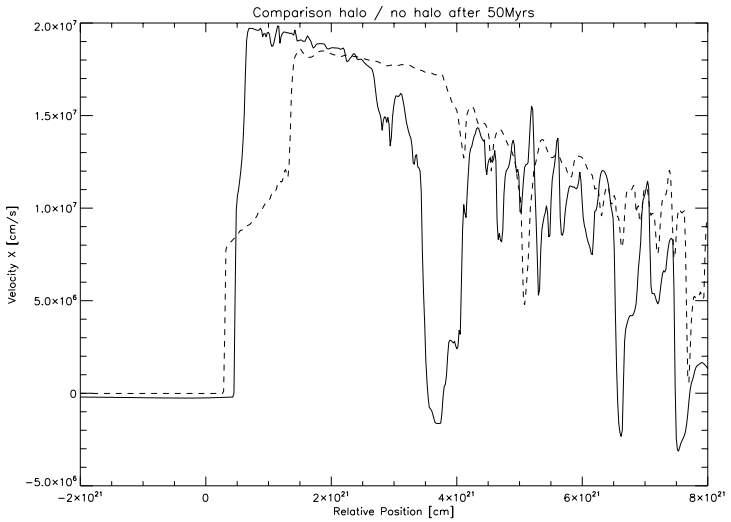

Figure 6.7: Comparison of the velocities (here: $vel_x = 2 \cdot 10^7 - vel_x$) between Run Nr. 3 (with DM halo, solid line) and Run Nr. 7 (without DM halo, dashed line) after 50 Myrs.

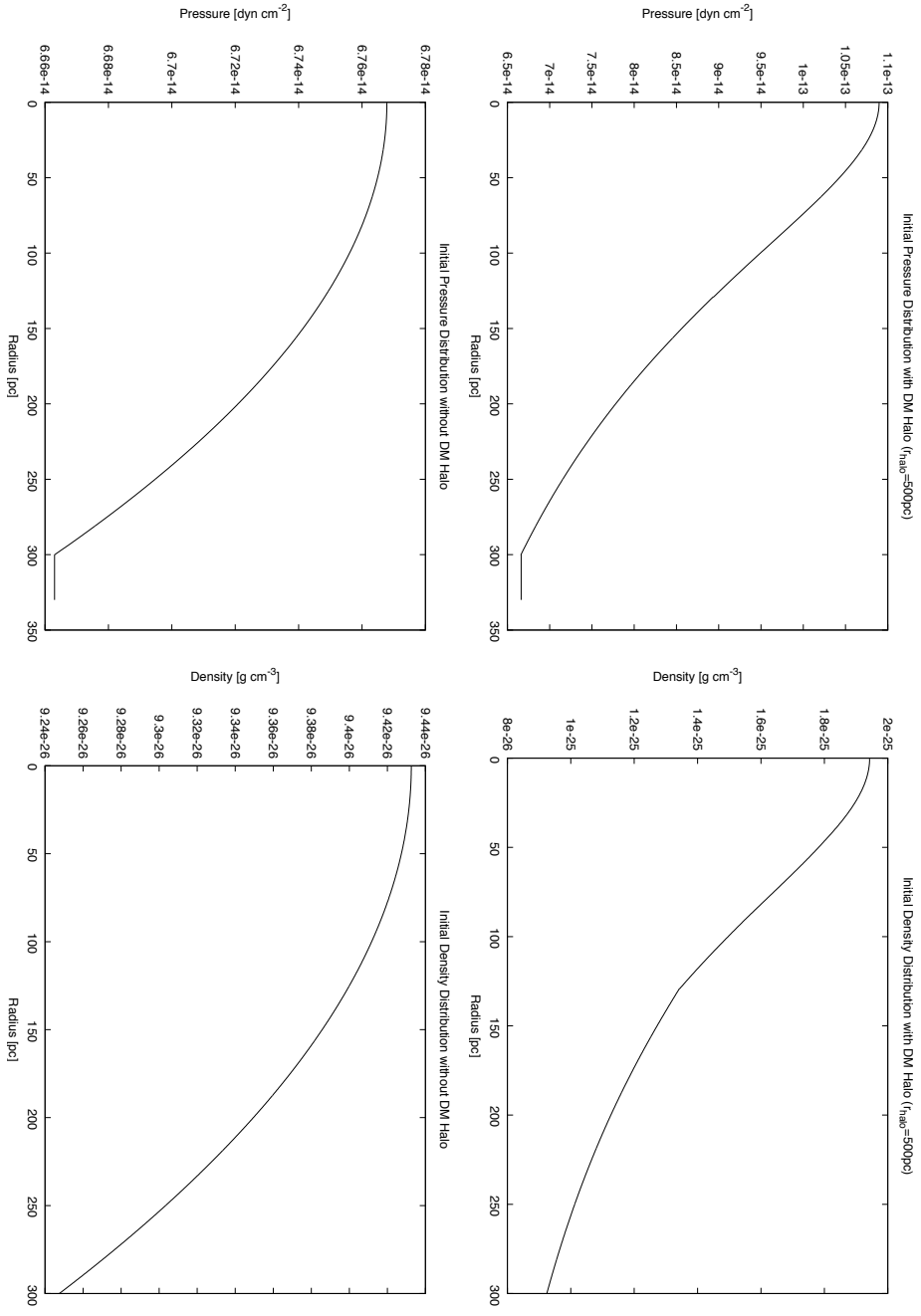

Figure 6.8: Initial 1D pressure and density distributions of a stable cloud without DM halo (left) and with DM halo (right, $r_{halo} = 500\,pc$, $r0_{halo} = 200\,pc$).

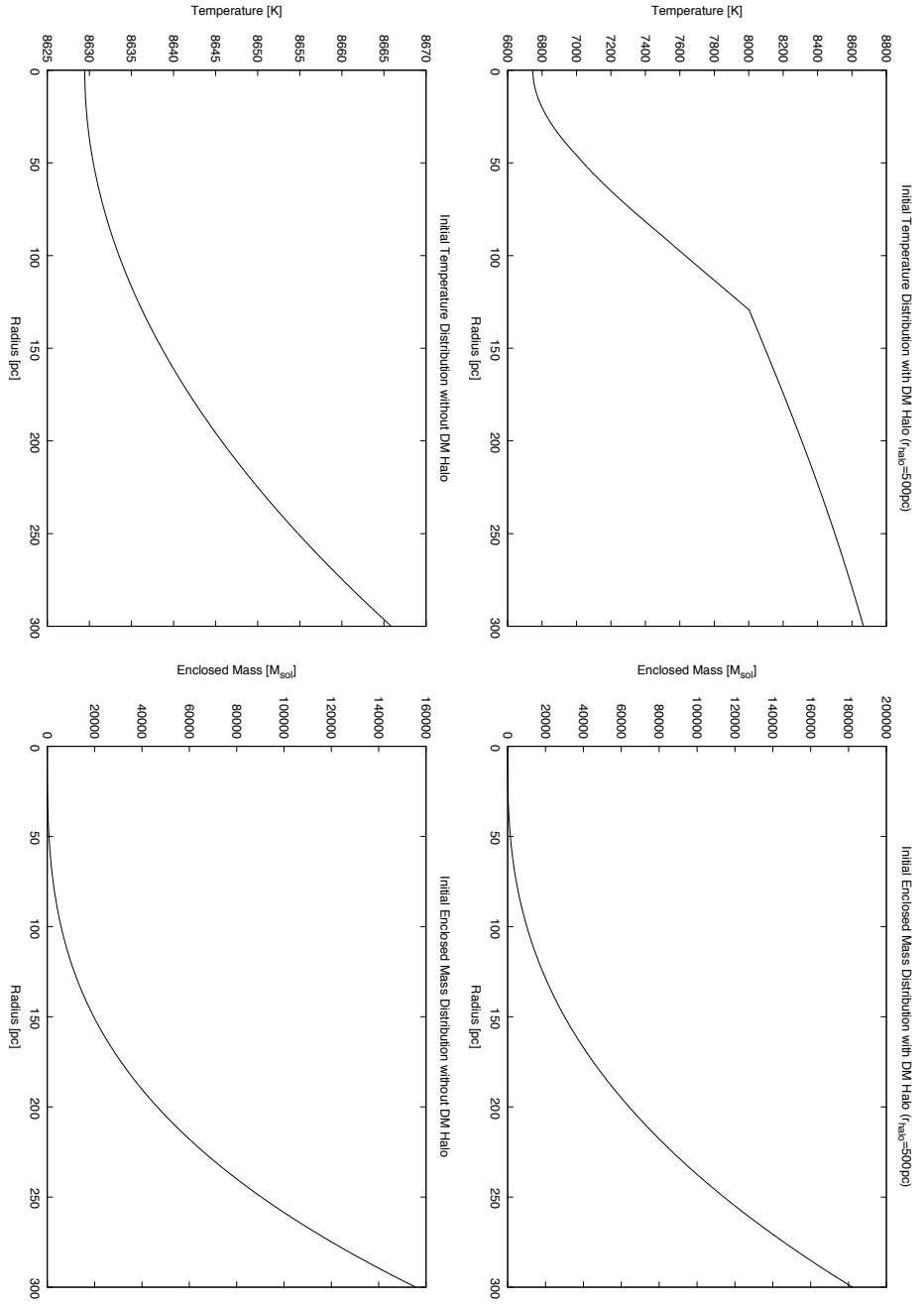

Figure 6.9: Initial 1D temperature distribution and enclosed mass of a stable cloud without DM halo (left) and with DM halo (right, $r_{halo} = 500\,pc$, $r0_{halo} = 200\,pc$).

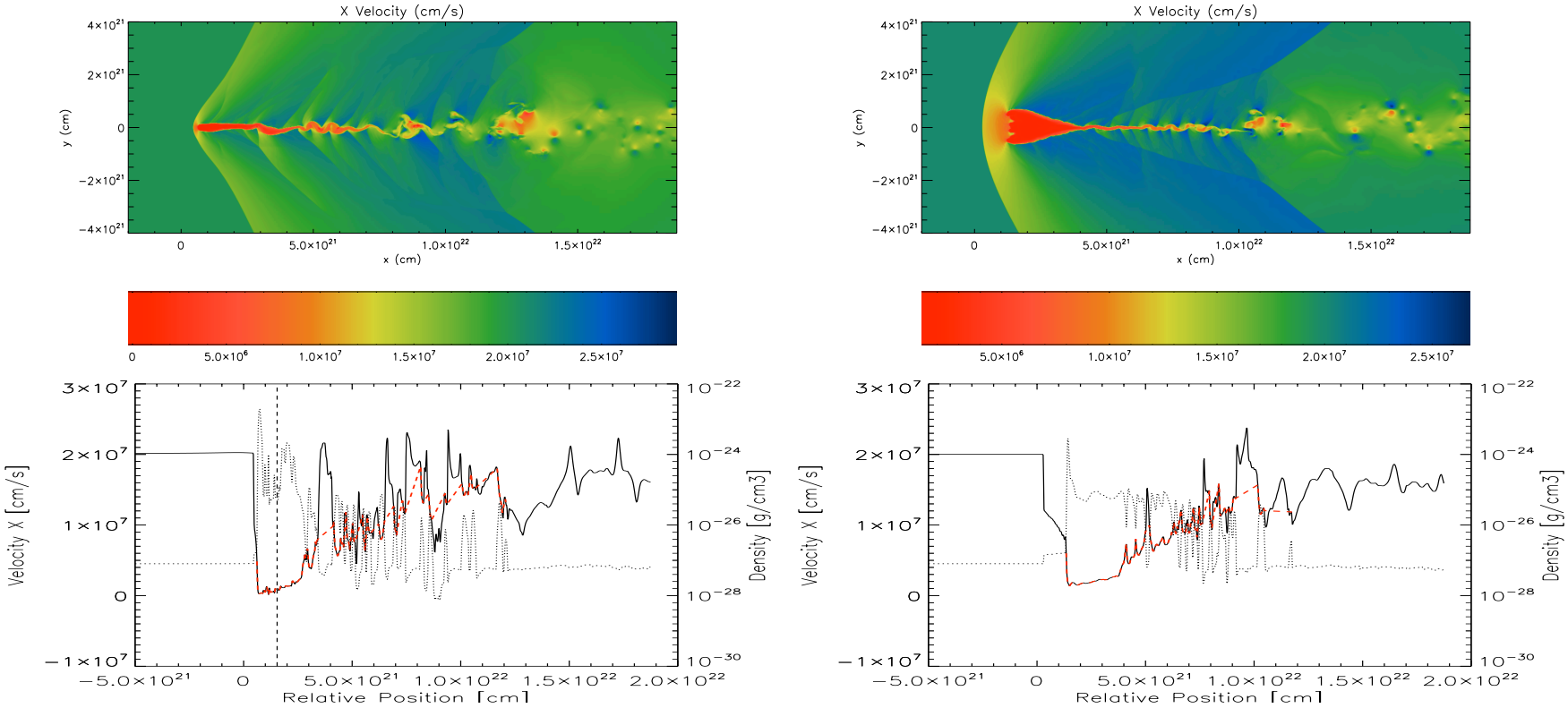

Figure 6.10: Streaming velocity = 200 km/s: Run 3 (left panels, with DM) vs. Run 7 (right panels, without DM) after 50 Myrs. Fig. 6.10 to Fig. 6.13: The upper panels show the 2D x-velocity distribution in color code, while the lower panels describe both the x-velocity and density distribution along the x-axis as explained in Fig. 6.1. The black dashed lines in runs with DM indicate the edge of the gravitational potential.

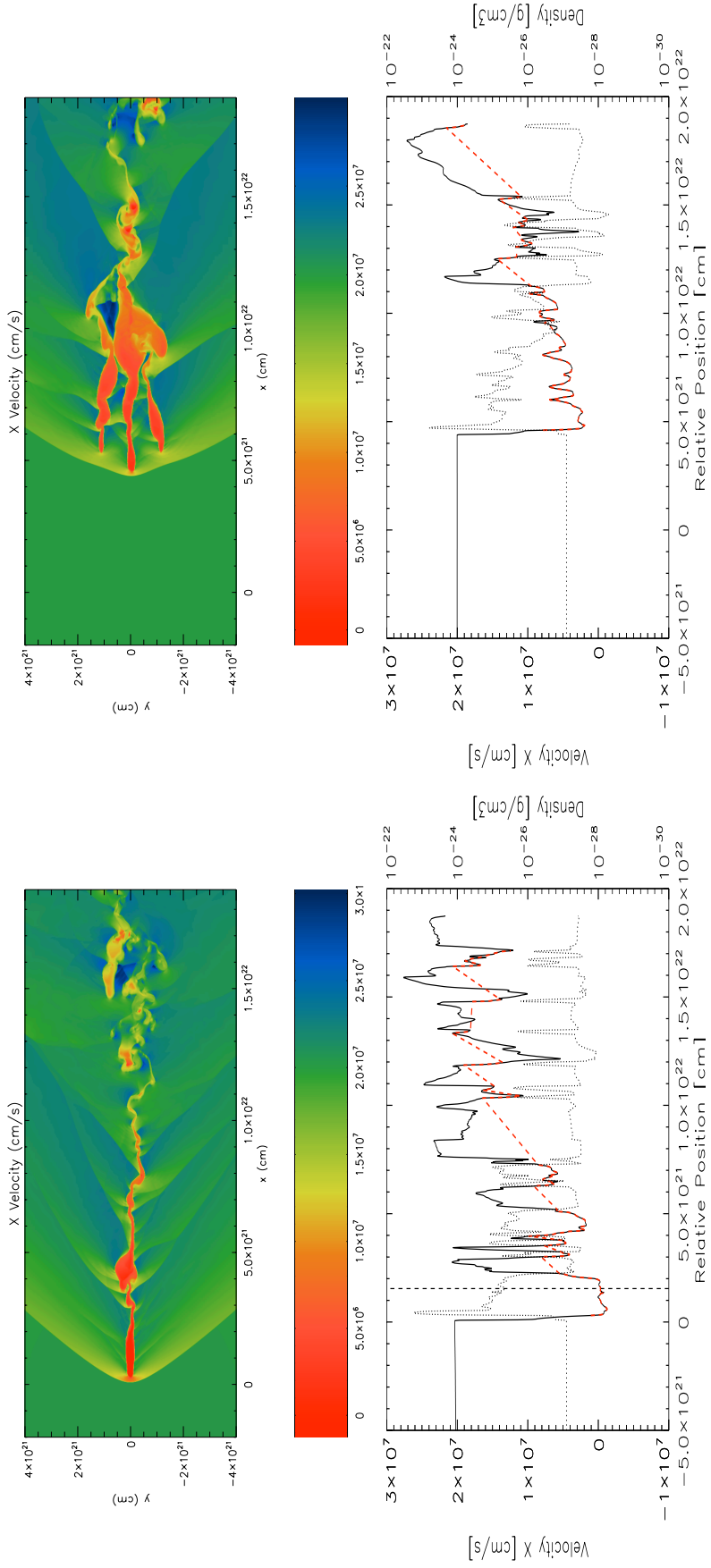

Figure 6.11: Run 3 (left panels, with DM) vs. Run 7 (right panels, without DM) after 100 Myrs.

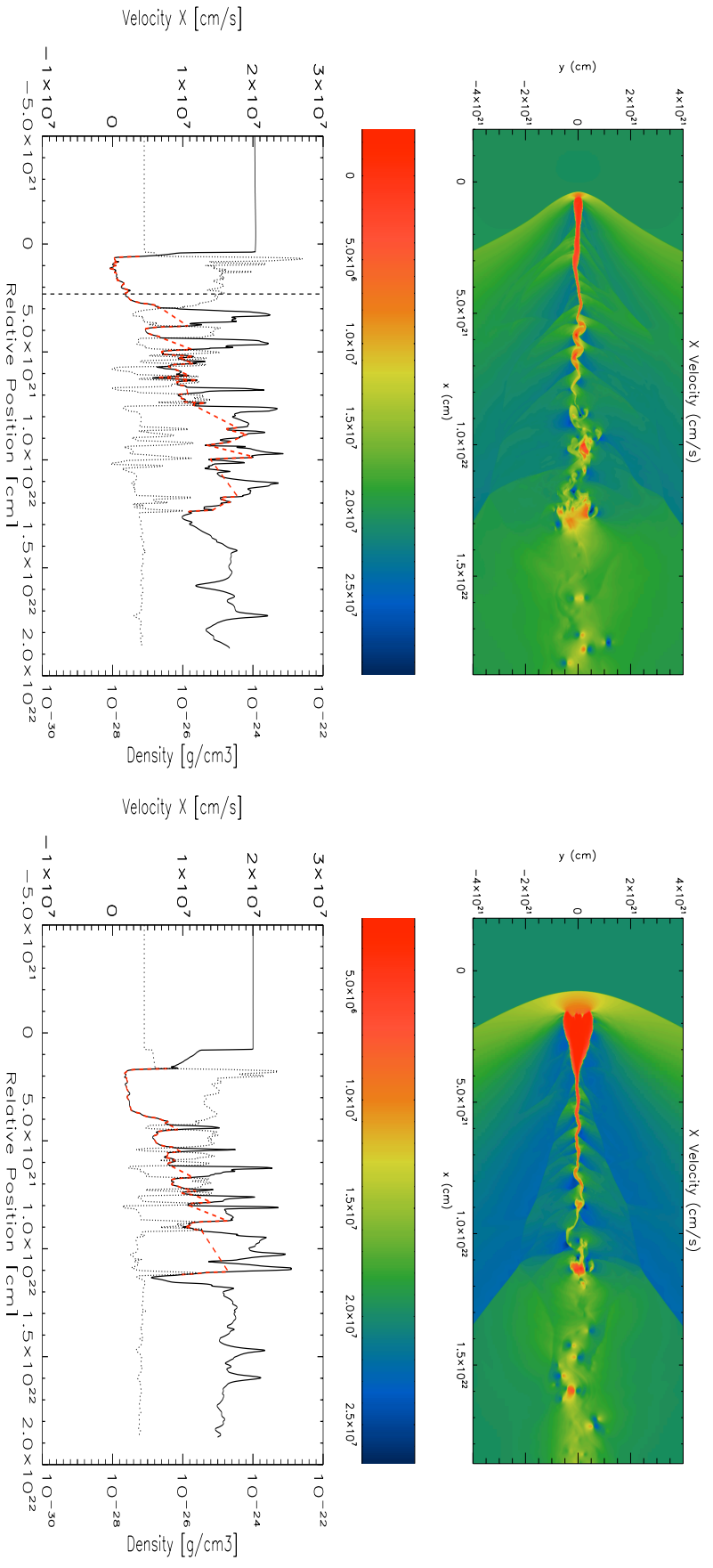

Figure 6.12: Run 8 (left panels, with DM) vs. Run 2 (right panels, without DM) after 50 Myrs.

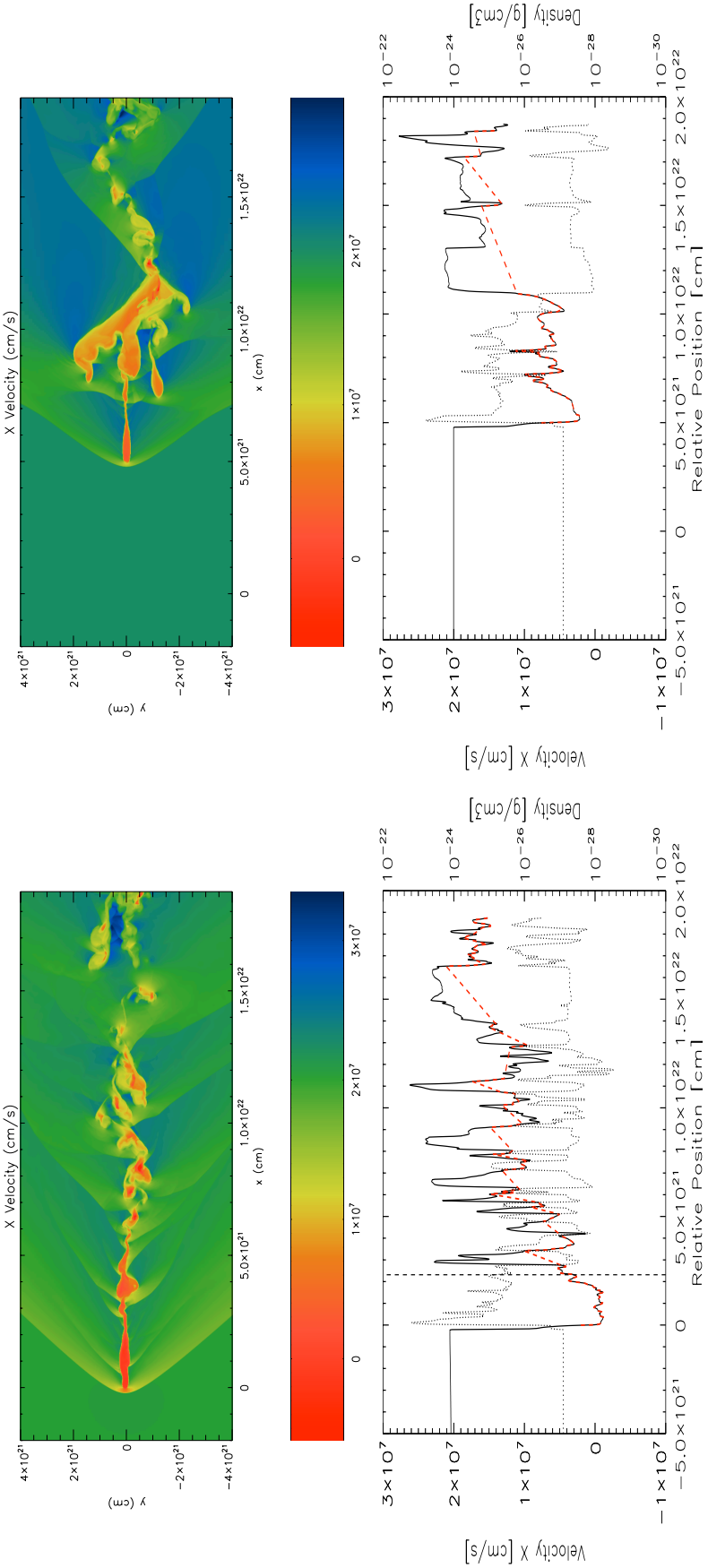

Figure 6.13: Run 8 (left panels, with DM) vs. Run 2 (right panels, without DM) after 100 Myrs.

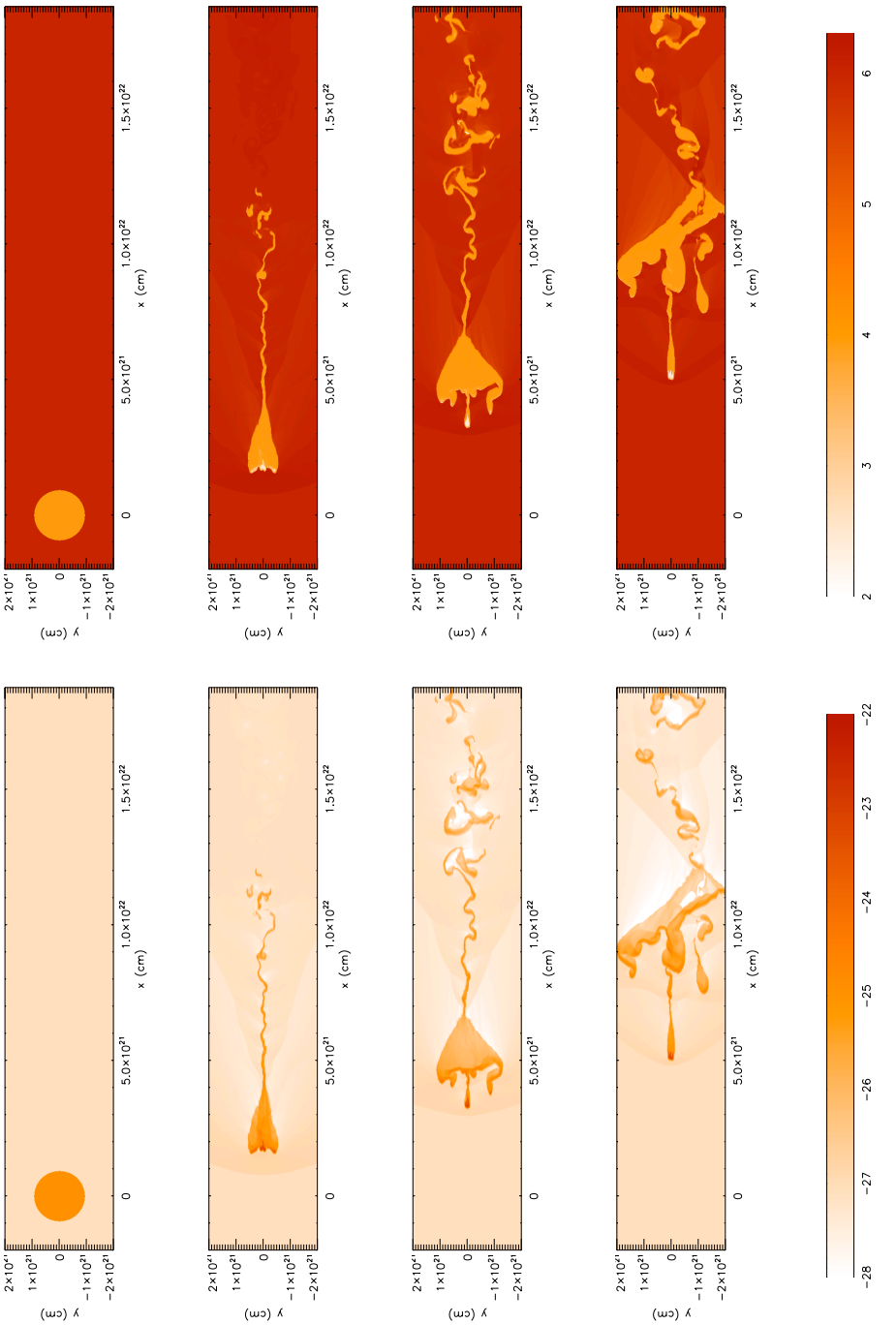

Figure 6.14: As in Fig. 6.5, but for Run 2 (without DM halo).

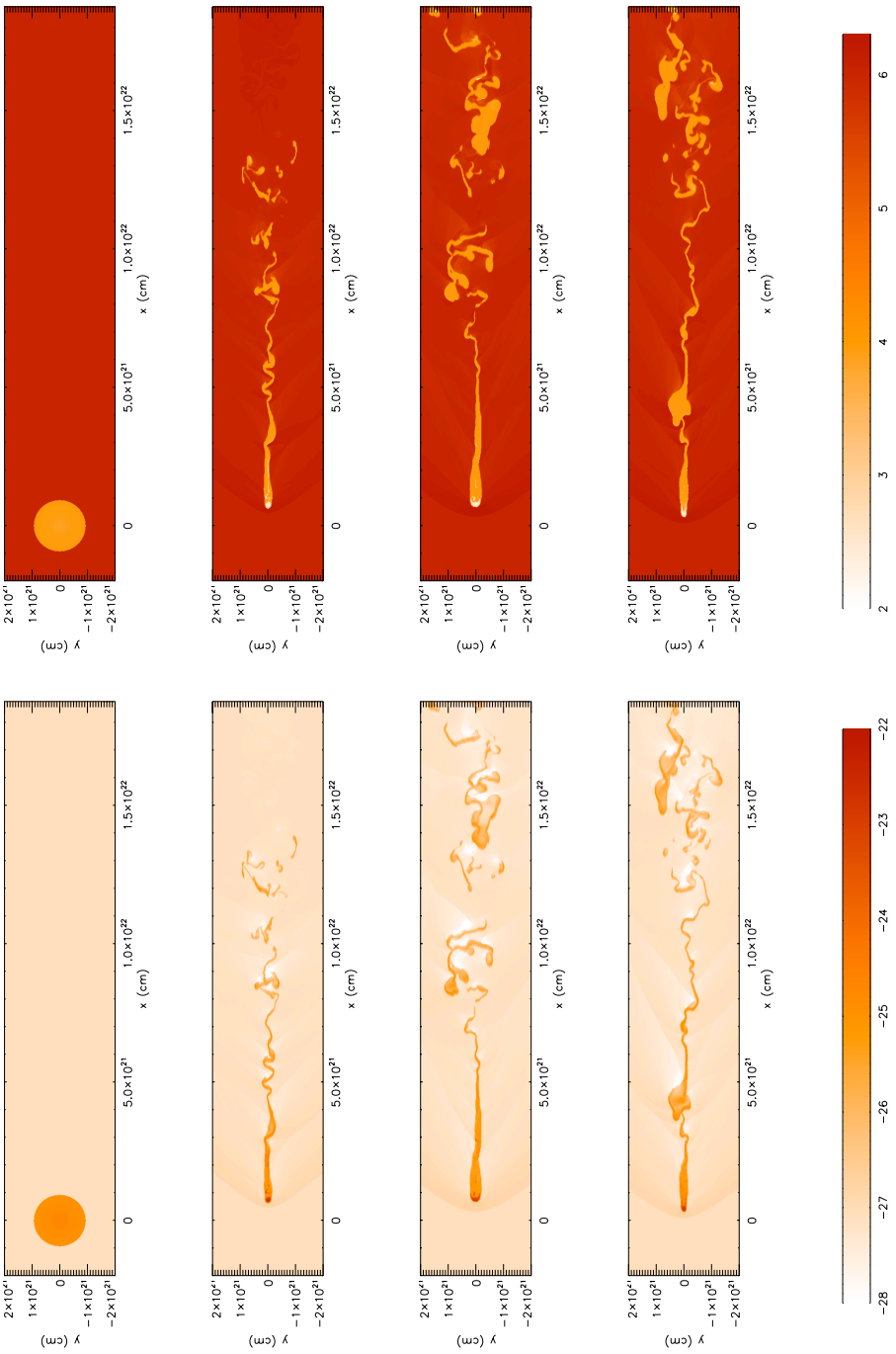

Figure 6.15: As in Fig. 6.5, but for Run 3 (with DM halo).

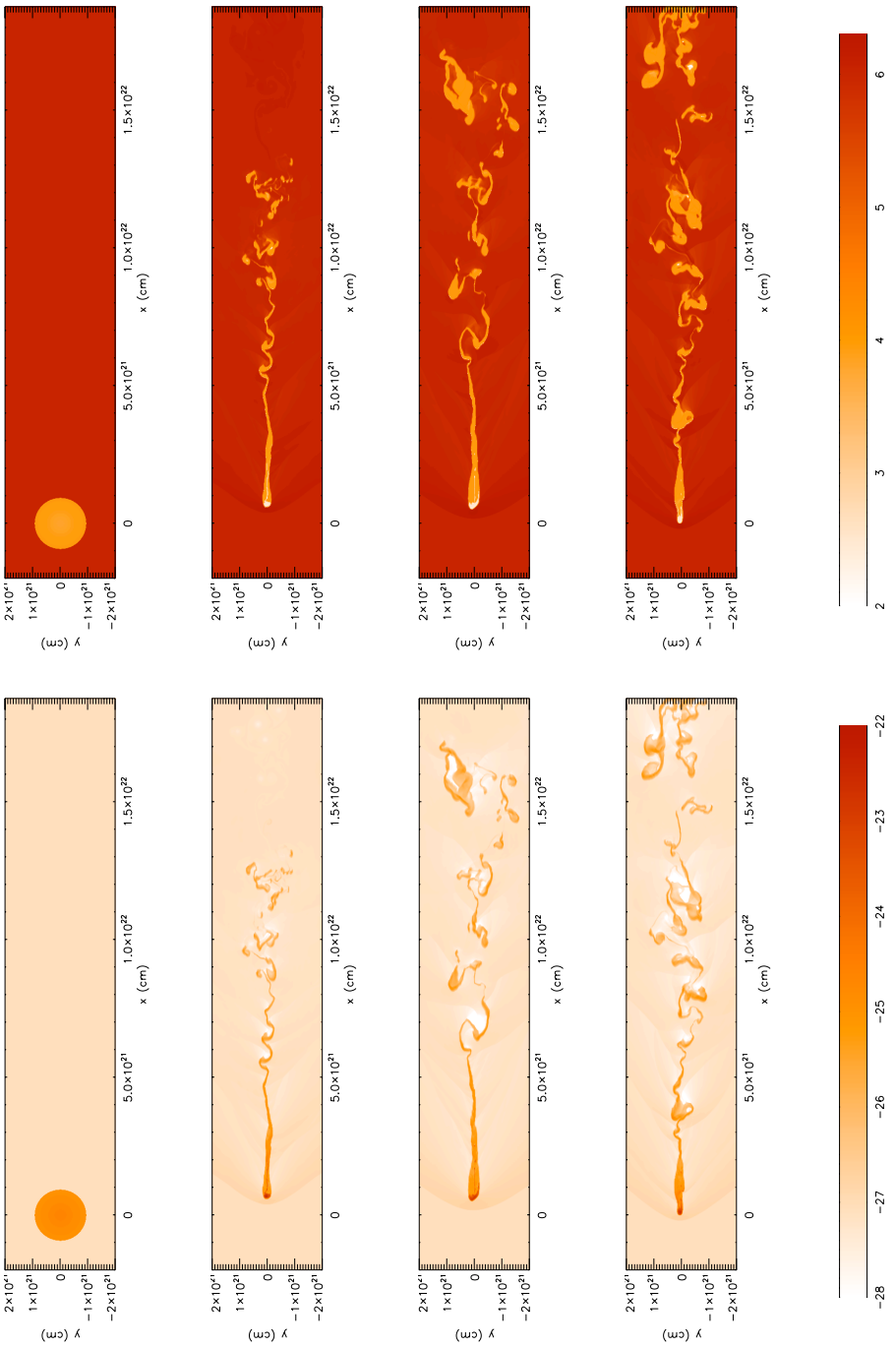

Figure 6.16: As in Fig. 6.5, but for Run 8 (with DM halo).

6.5 Effect of cloud velocity (Run 10 vs. Run 9 and Run 12 vs. Run 13)

The observed absolute radial velocities of HVCs lie roughly in the range of 100 to 400 $km\,s^{-1}$ relative to the LSR. For velocities above the sound speed c_s corresponding to a Mach number of more than 1, a bow show occurs in front of the cloud. The sound speed for an ideal gas can be determined by

$$c_s = \sqrt{\gamma \cdot \frac{p}{\rho}} \tag{6.1}$$

where γ is the adiabatic index, p the pressure and ρ the density of the gas. Together with the equation of state for an ideal gas

$$p = R_{ideal}\rho T \tag{6.2}$$

where R_{ideal} is the specific gas constant, the sound speed only depends on the gas temperature:

$$c_s = \sqrt{\gamma R_{ideal} T} \tag{6.3}$$

For a ISM temperature of $10^6 K$ the speed of sound is $c_s = 91.2\,km\,s^{-1}$. The streaming velocities used in the simulation are 100, 200 and 300 $km\,s^{-1}$, with Mach numbers of 1.1, 2.2 and 3.3 (see Fig. 6.17 to Fig. 6.20 for v_{stream} = 100 and 300 $km\,s^{-1}$ and Fig. 6.10 to Fig. 6.13 for $v_{stream} = 200\,km\,s^{-1}$). Therefore all setups are supersonic and bow shocks occur in every simulation run. For every streaming velocity a comparison is shown between the runs with and without a DM halo. The deviation in the relative position Δr and therefore the velocity decrease Δv due to the ram pressure for $vel_x = 100\,km\,s^{-1}$ is $\Delta r \approx 1 \times 10^{21} cm$ in 100 Myrs and therefore $\Delta v = 3\,km\,s^{-1}$, for $\Delta r \approx vel_x = 200\,km\,s^{-1}$ it is $4.5 \times 10^{21}\,cm$ in 100 Myrs and already $\Delta v = 14\,km\,s^{-1}$, while for $vel_x = 300\,km\,s^{-1}$ the velocity drop due to drag force is $3 \times 10^{21}\,cm$ in 100 Myrs and $\Delta v = 9.5\,km\,s^{-1}$. The explanation for a smaller Δx for the highest streaming velocity is the much smaller area that is affected by drag due to the more powerful stripping and the more streamlined shape of the cloud. The observed HT structure can be reproduced only for very high velocities without an additional gravitational potential. The terminal velocity model by Benjamin & Danly (1997) describes the motion of an in-falling gas cloud with

$$m_c \frac{dv_c}{dt} = \frac{1}{2} C_D \rho_h(z) v_c^2 A_c - m_c g(z) \tag{6.4}$$

where m_c, v_c, A_c are the mass, velocity and surface area of the cloud, C_D is the drag coefficient, $\rho_h(z)$ is the density of the halo and g(z) is the gravitational acceleration in dependence of the galactic height z. They claim that there should be a height z for which the drag force equals the gravitational force of the galaxy and therefore dv_c/dt will vanish. The galactic height would then correlate to a terminal velocity v_T. In their theory the surface area of the cloud would be constant over time. This simulation shows that the surface area of the cloud changes dramatically over time and the density decrease Δv is not proportional to the streaming velocity vel_x (compare: $vel_x = 100\,km\,s^{-1} \rightarrow \Delta v = 3\,km\,s^{-1}$ $vel_x = 200\,km\,s^{-1} \rightarrow \Delta v = 14\,km\,s^{-1}$ while $vel_x = 300\,km\,s^{-1} \rightarrow \Delta v = 9.5\,km\,s^{-1}$).

Figure 6.17: Streaming velocity = 100 km/s: Run 9 (left panels, with DM) vs. Run 10 (right panels, without DM) after 50 Myrs. Fig. 6.17 to Fig. 6.20: The upper panels show the 2D x-velocity distribution in color code, while the lower panels describe both the x-velocity and density distribution along the x-axis as explained in Fig. 6.1.

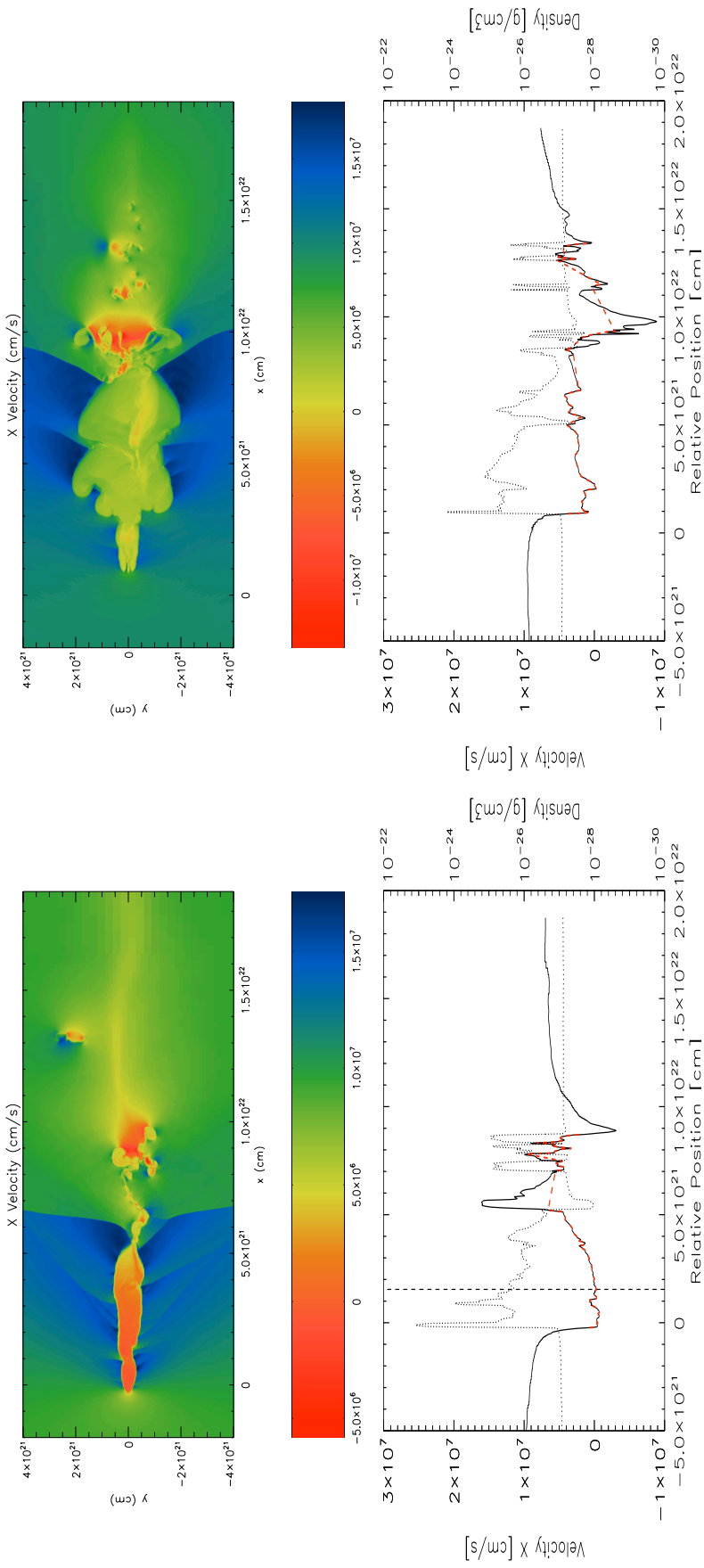

Figure 6.18: Streaming velocity = 100 km/s: Run 9 (left panels, with DM) vs. Run 10 (right panels, without DM) after 100 Myrs.

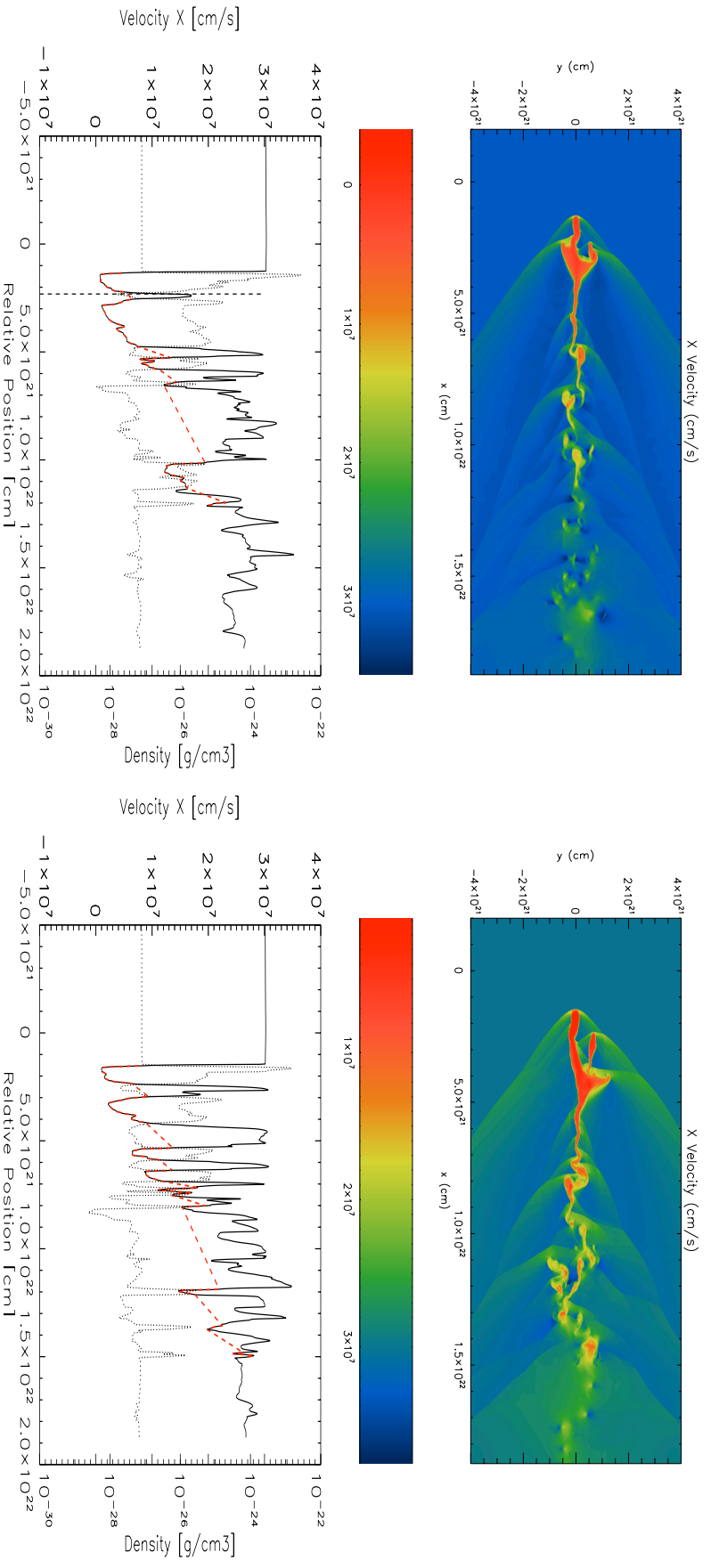

Figure 6.19: Streaming velocity = 300 km/s: Run 13 (left panels, with DM) vs. Run 12 (right panels, without DM) after 50 Myrs.

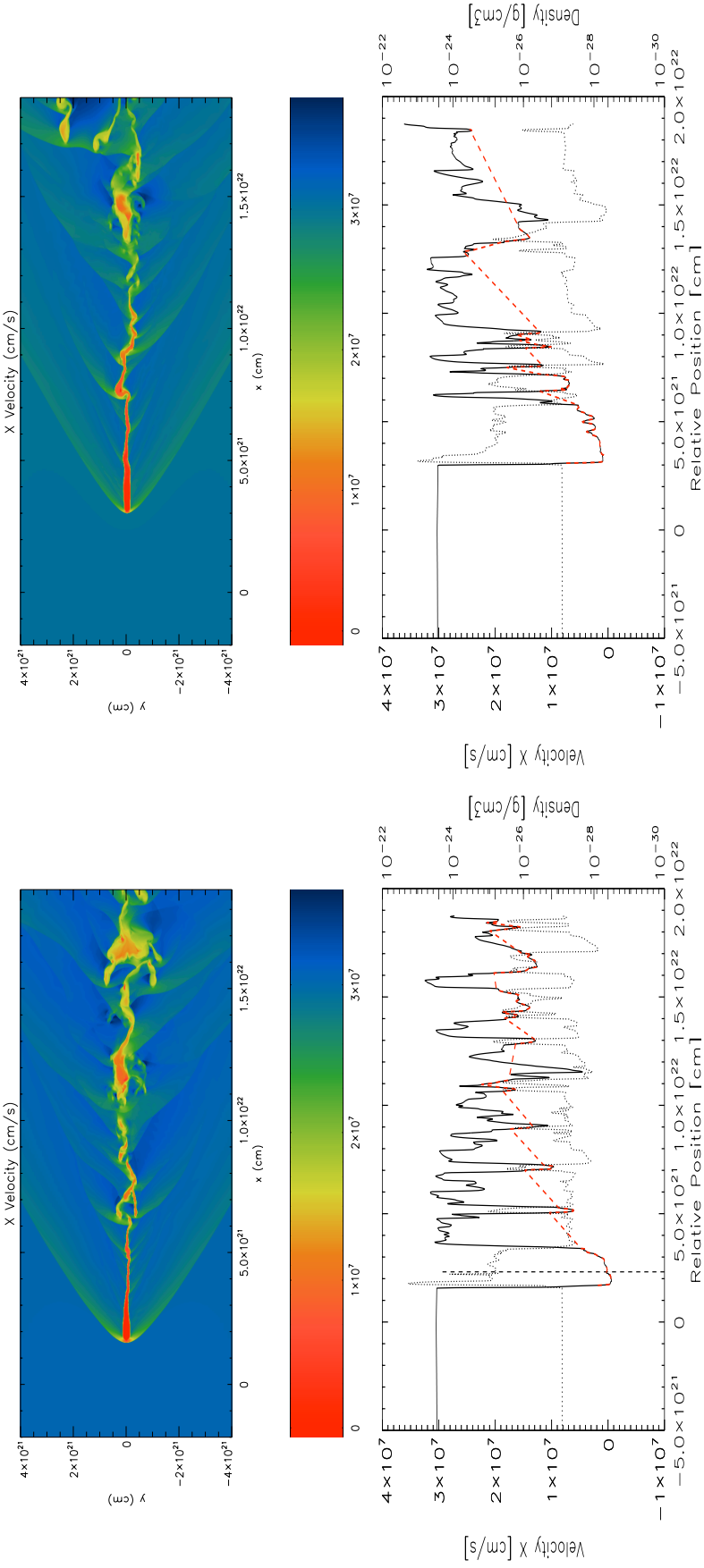

Figure 6.20: Streaming velocity = 300 km/s: Run 13 (left panels, with DM) vs. Run 12 (right panels, without DM) after 100 Myrs.

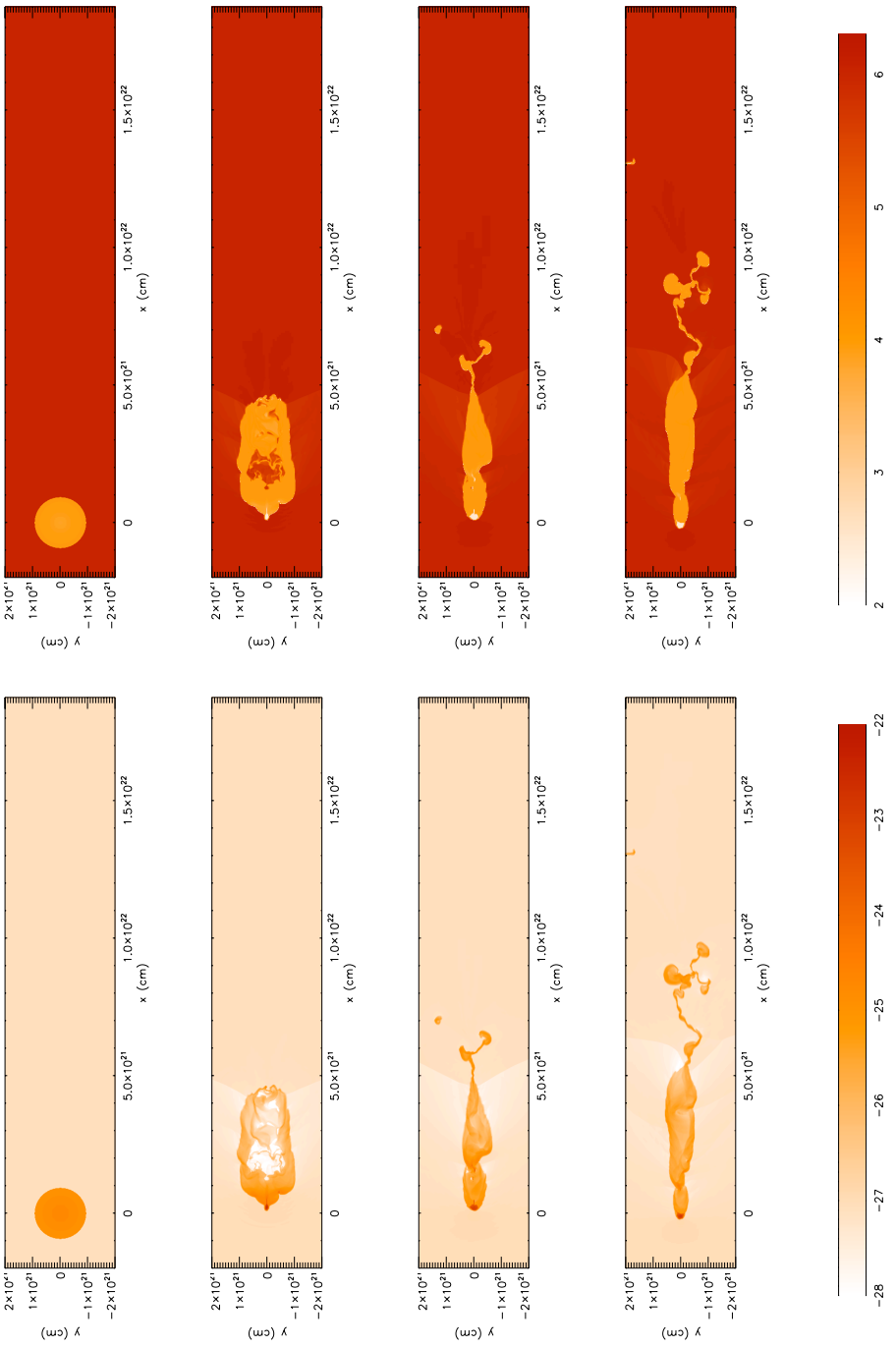

Figure 6.21: As in Fig. 6.5, but for Run 9 (with DM halo, $v_{stream} = 100\,km\,s^{-1}$).

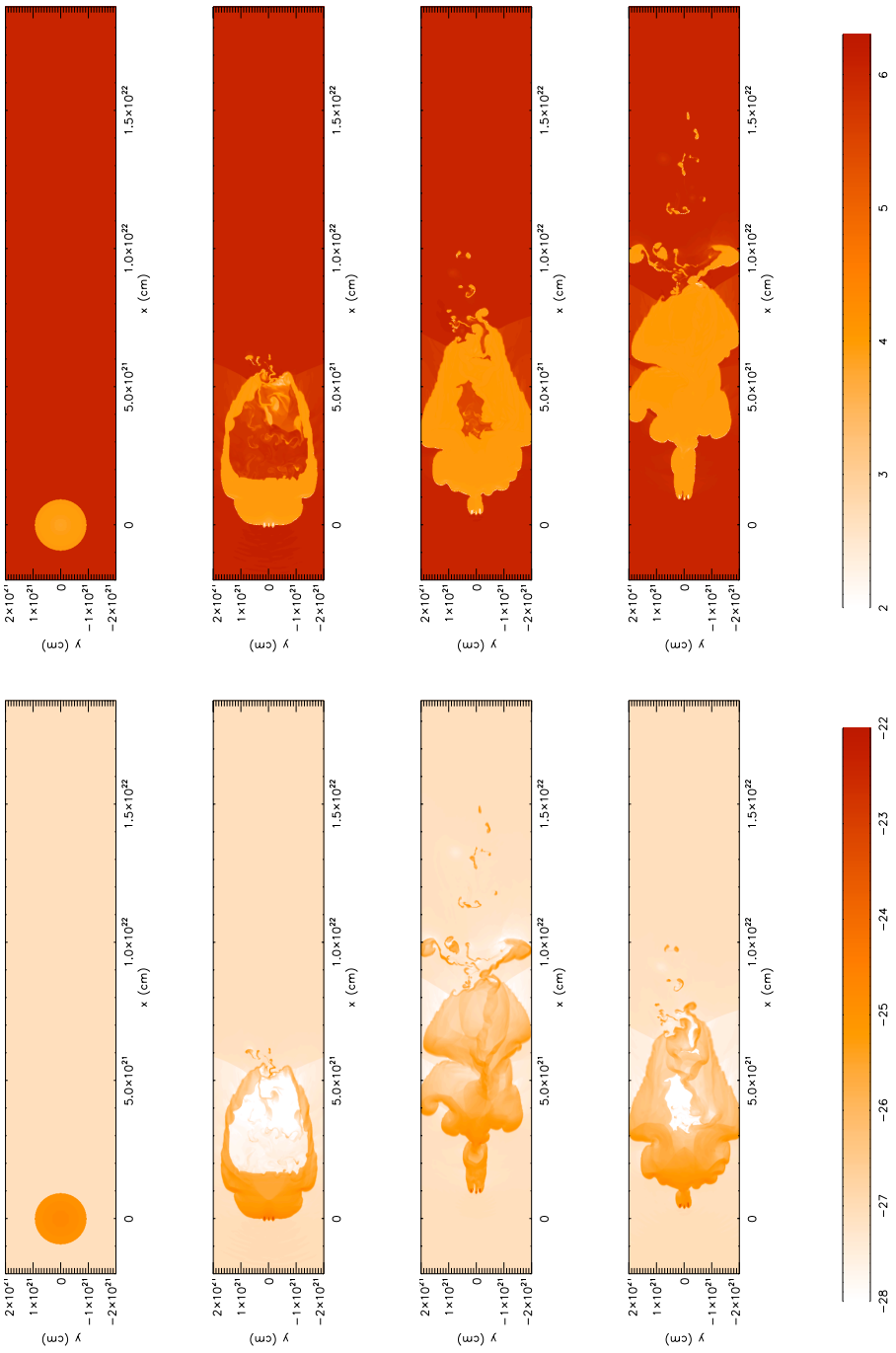

Figure 6.22: As in Fig. 6.5, but for Run 10 (without DM halo, $v_{stream} = 100\,km\,s^{-1}$).

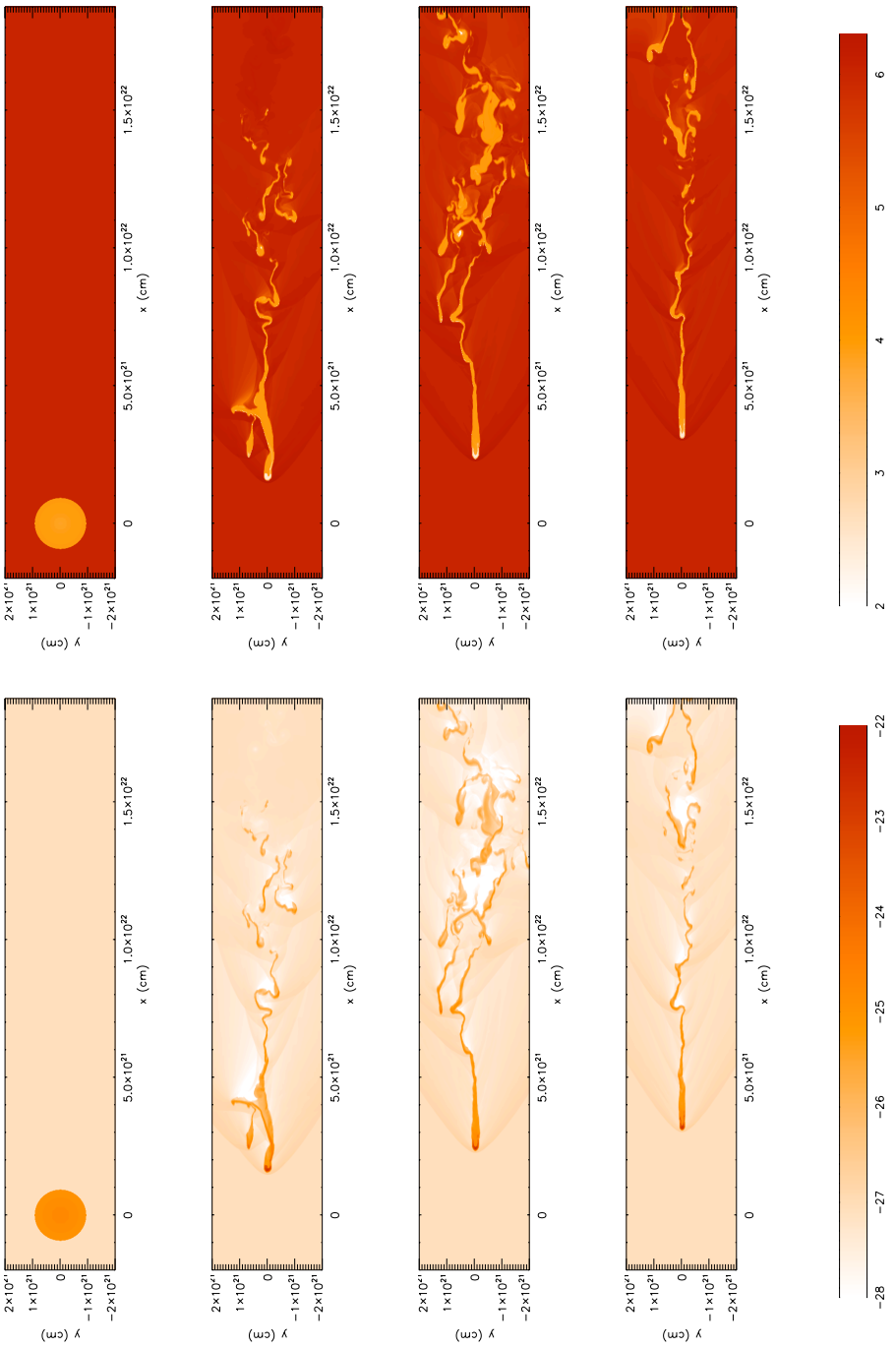

Figure 6.23: As in Fig. 6.5, but for Run 12 (without DM halo, $v_{stream} = 300\,km\,s^{-1}$).

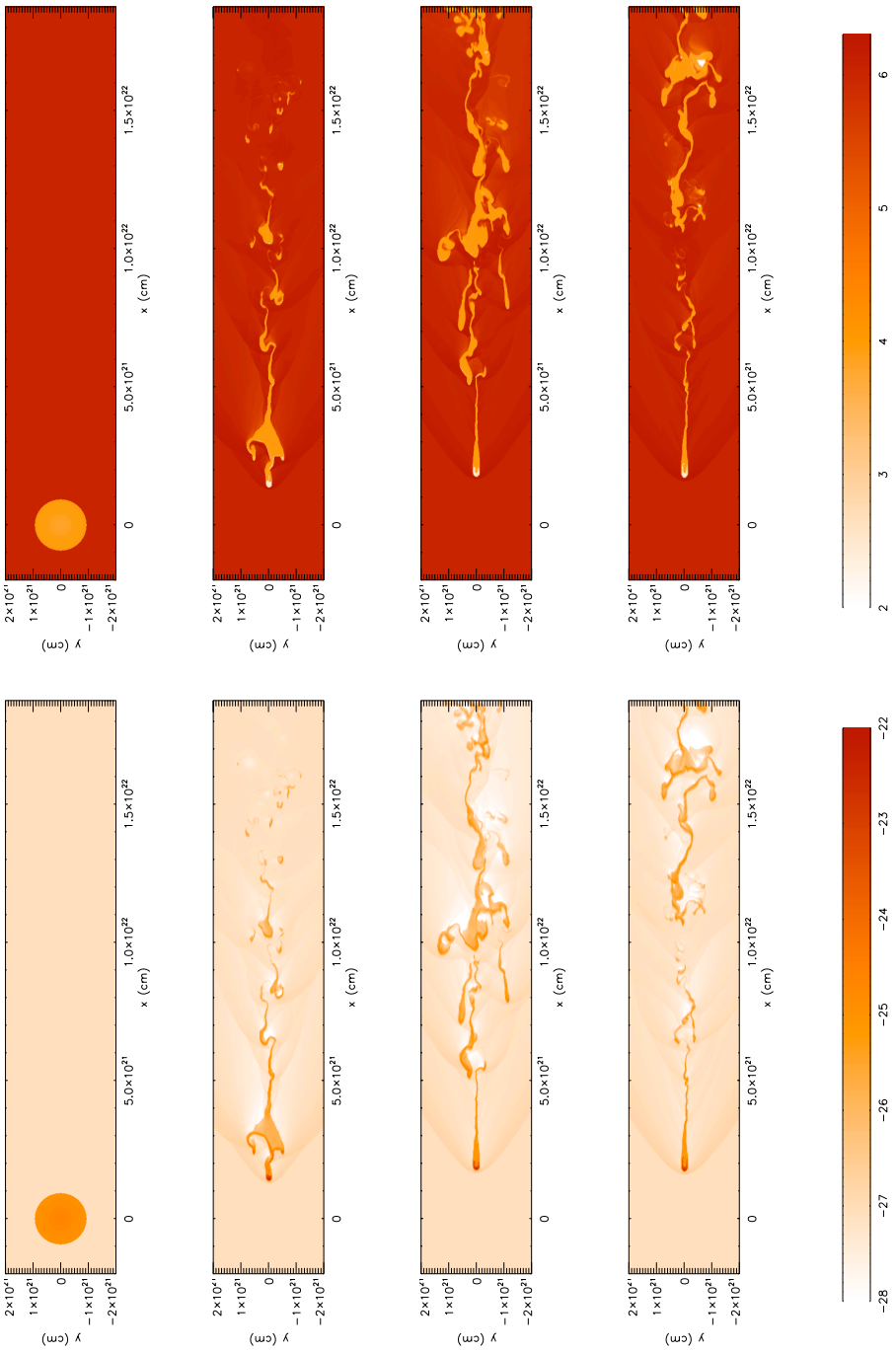

Figure 6.24: As in Fig. 6.5, but for Run 13 (with DM halo, $v_{stream} = 300\,km\,s^{-1}$).

6.6 Effect of HIM temperature (Run 5 vs. Run 14)

The temperature is the only free parameter of the ambient medium. The density is determined by the cooling and heating equilibrium function, because the hot ionized medium (HIM) is not supposed to change due to any thermal processes within the simulation time. Subsequently the pressure is calculated using the ideal gas equation. The following table shows the values for the three different HIM temperatures used for simulation runs. In Fig. 6.25 the internal cloud distribution for a stable cloud with different HIM temperatures can be found. The whole build up of a stable cloud is very sensitive to an outer pressure. The differences of the cloud behavior when they face a streaming with $vel_x = 300\,km\,s^{-1}$ is shown in Fig. 6.26 to Fig. 6.27.

Temperature [K]	Density $[g\,cm^{-3}]$	Density $[cm^{-3}]$	Pressure [dyne cm^{-2}]
1.0×10^6	8.014×10^{-28}	4.79×10^{-4}	6.66×10^{-14}
1.5×10^6	8.233×10^{-28}	4.92×10^{-4}	1.03×10^{-13}
2.0×10^6	7.971×10^{-28}	4.76×10^{-4}	1.33×10^{-13}

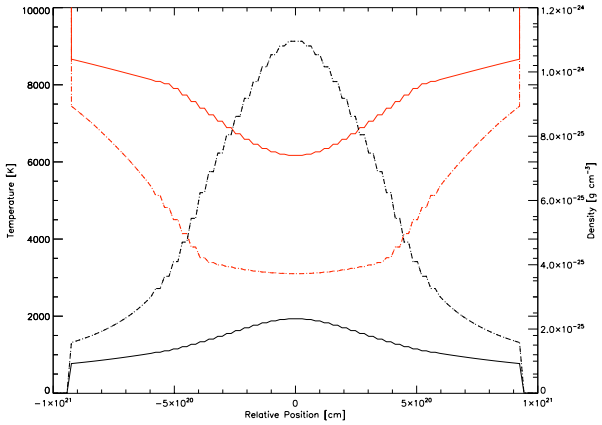

Figure 6.25: Temperature (red lines, left y-axis) and density (black lines, right y-axis) distribution of stable clouds in dependence of the HIM temperature. The solid lines refer to $T_{HIM} = 1 \times 10^6\,K$ and the dotted and dashed lines to $T_{HIM} = 1.5 \times 10^6\,K$ and $T_{HIM} = 2 \times 10^6\,K$. Since the pressures of $T_{HIM} = 1.5 \times 10^6\,K$ and $T_{HIM} = 2 \times 10^6\,K$ with their corresponding densities are almost equal (see Tab. 6.6) the initial cloud distributions are hardly distinguishable. Every cloud is embedded in a dark matter halo with $r = 750\,pc$ and $r_0 = 300\,pc$. The steps in the distributions are due to the 1D cut through the initial AMR grid.

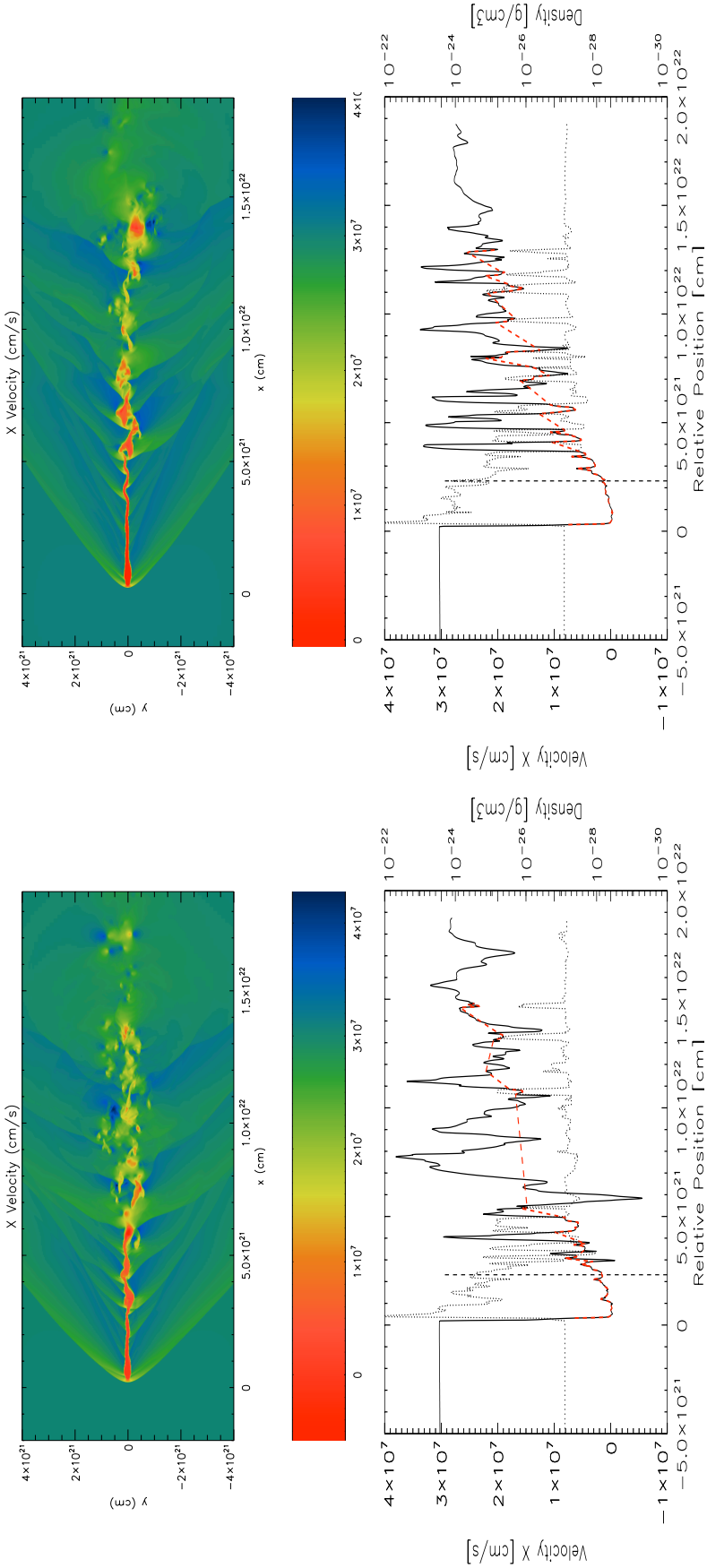

Figure 6.26: Streaming velocity = 300 km/s: Run 5 (left panels, $T_{ISM} = 2 \times 10^6\,K$) vs. Run 14 (right panels, $T_{ISM} = 1.5 \times 10^6\,K$) after 50 Myrs. Fig. 6.26 to Fig. 6.27: The upper panels show the 2D x-velocity distribution in color code, while the lower panels describe both the x-velocity and density distribution along the x-axis as explained in Fig. 6.1.

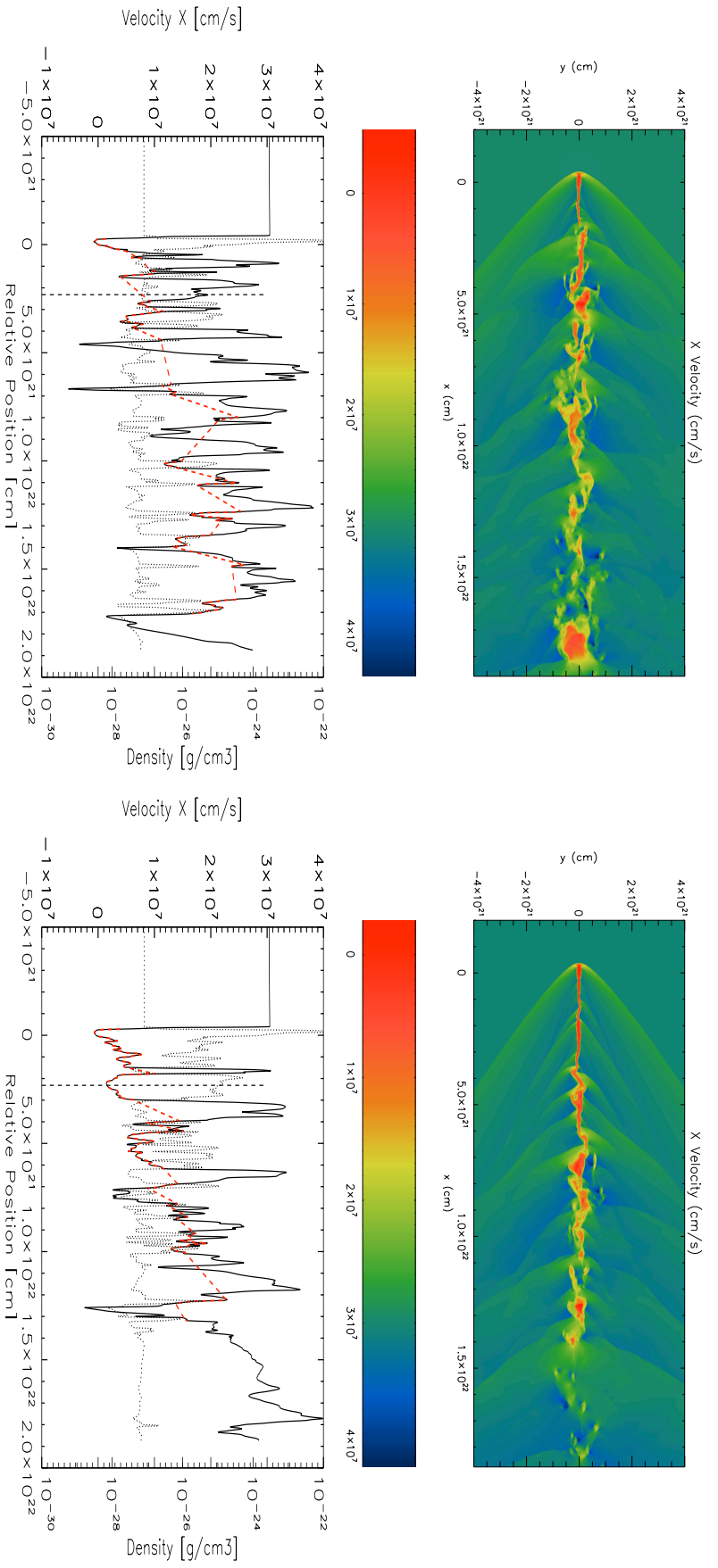

Figure 6.27: Streaming velocity = 300 km/s: Run 5 (left panels, $T_{ISM} = 2 \times 10^6\,K$) vs. Run 14 (right panels, $T_{ISM} = 1.5 \times 10^6\,K$) after 100 Myrs.

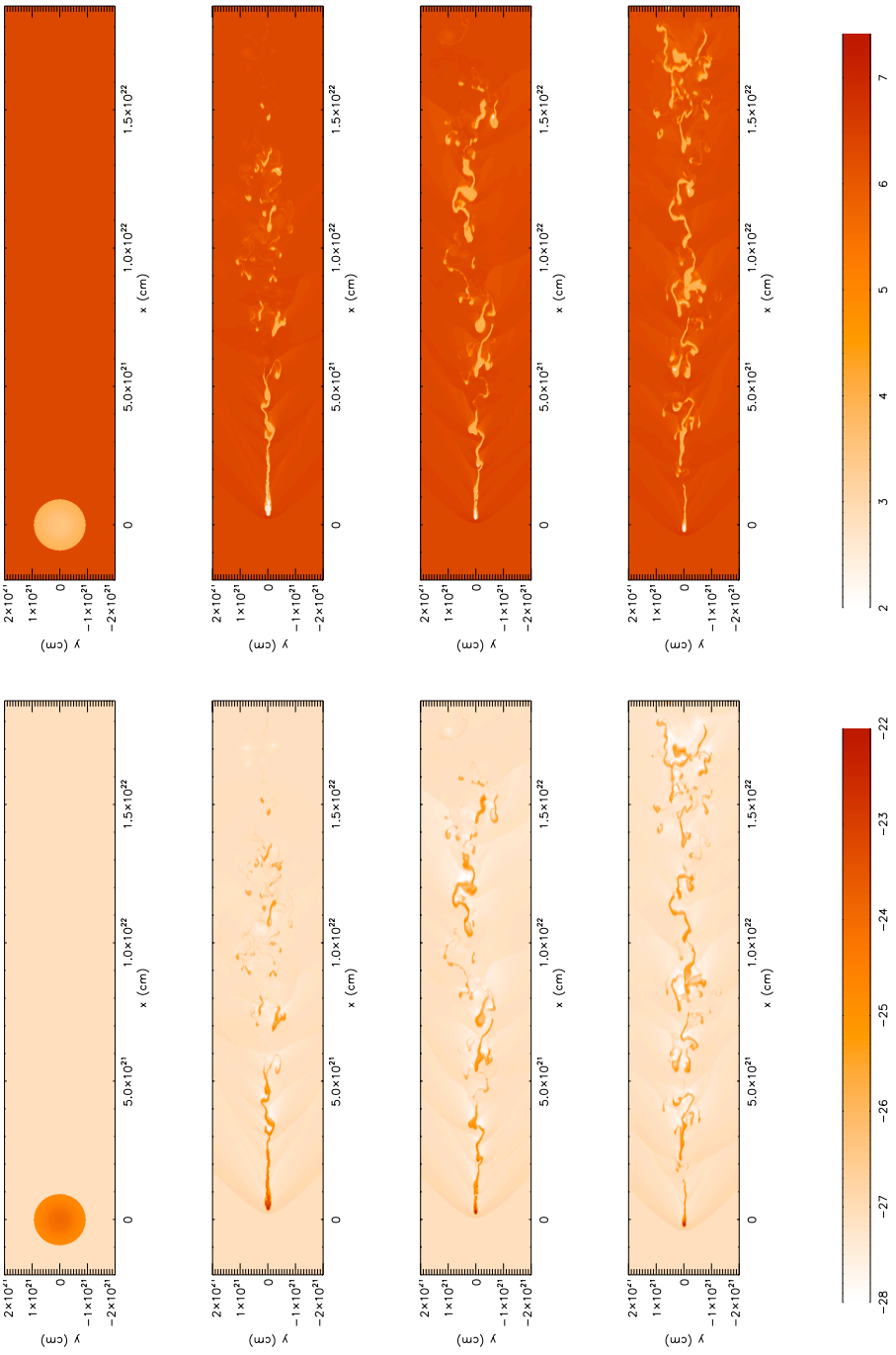

Figure 6.28: As in Fig. 6.5, but for Run 5 (with DM halo, $v_{stream} = 300\,km\,s^{-1}$, $T_{ISM} = 2 \times 10^6\,K$).

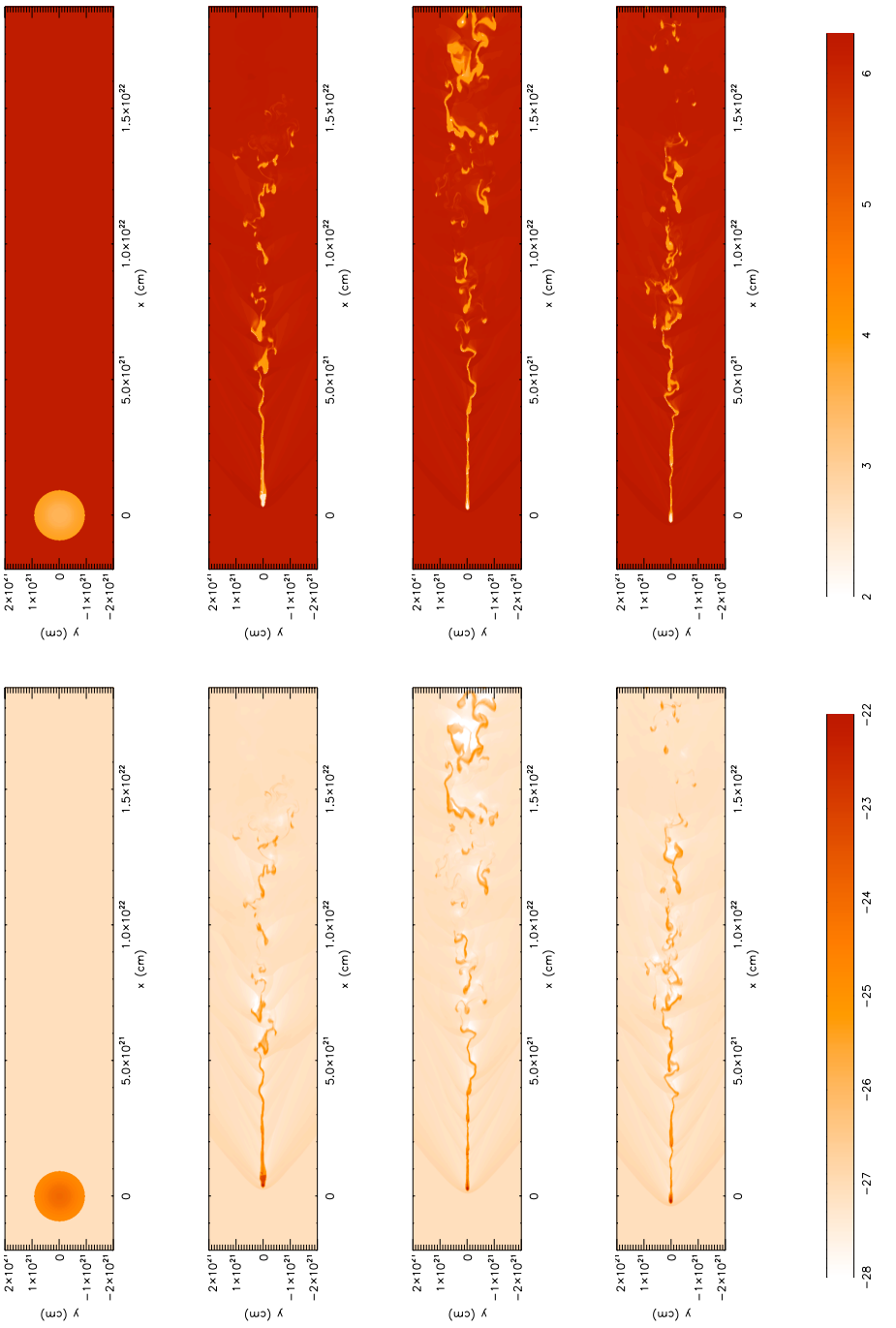

Figure 6.29: As in Fig. 6.5, but for Run 14 (with DM halo, $v_{stream} = 300\,km\,s^{-1}$, $T_{ISM} = 1.5 \times 10^6\,K$).

6.7 Effect of thermal processes on/off (Run 7 vs. Run 1)

The thermal processes have a large impact on a cloud affected by streaming. The internal energy derivative

$$\frac{\partial \epsilon}{\partial t} = n\Gamma(T) - n^2\Lambda(T) \tag{6.5}$$

leads to a very effective cooling for higher densities, which subsequently decreases the thermal pressure in this region, increasing the density at that place even more. This temperature drop is possible until temperatures of about 300 K are reached, where heating is more effective than cooling even for high densities. In all runs including thermal processes, the cloud forms a cold core with temperatures around 300 K and a warmer envelope with temperatures of 8000 K which is in perfect agreement with the observations. The runs without dark matter halo and with streaming velocities of $vel_x = 100\,km\,s^{-1}$ or $vel_x = 200\,km\,s^{-1}$ show a finger-like structure with a core/envelope structure in each finger. These structures can also be observed for example in M16, the eagle nebula (see Fig. 6.30).

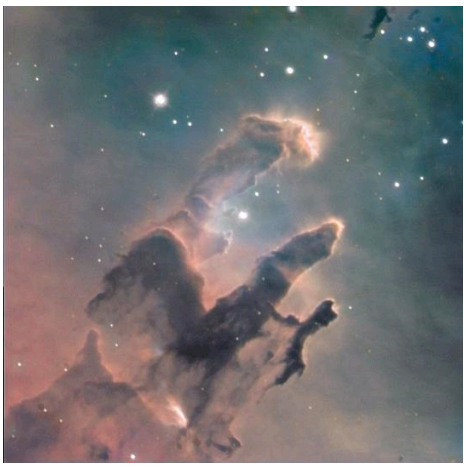

Figure 6.30: Image of the Eagle Nebula by Nik Szymanek (http://faulkes-telescope.com/)

Although there is no gravitational collapse appearing in the simulation contrary to the star formation on the tips of the eagle nebula, similarities in the density distribution can be found. The simulations show that the morphology of runs without a dark matter halo is similar to observed structures in emission nebulae not supposed to contain any dark matter, while the results of runs with an additional gravitational potential reproduce the structure of CHVCs very well. The thermal processes play an important role in any case, since without cooling and heating the evolution of the clouds is very different and no core/envelope structure can be reproduced (see Fig. 6.31 and Fig. 6.32).

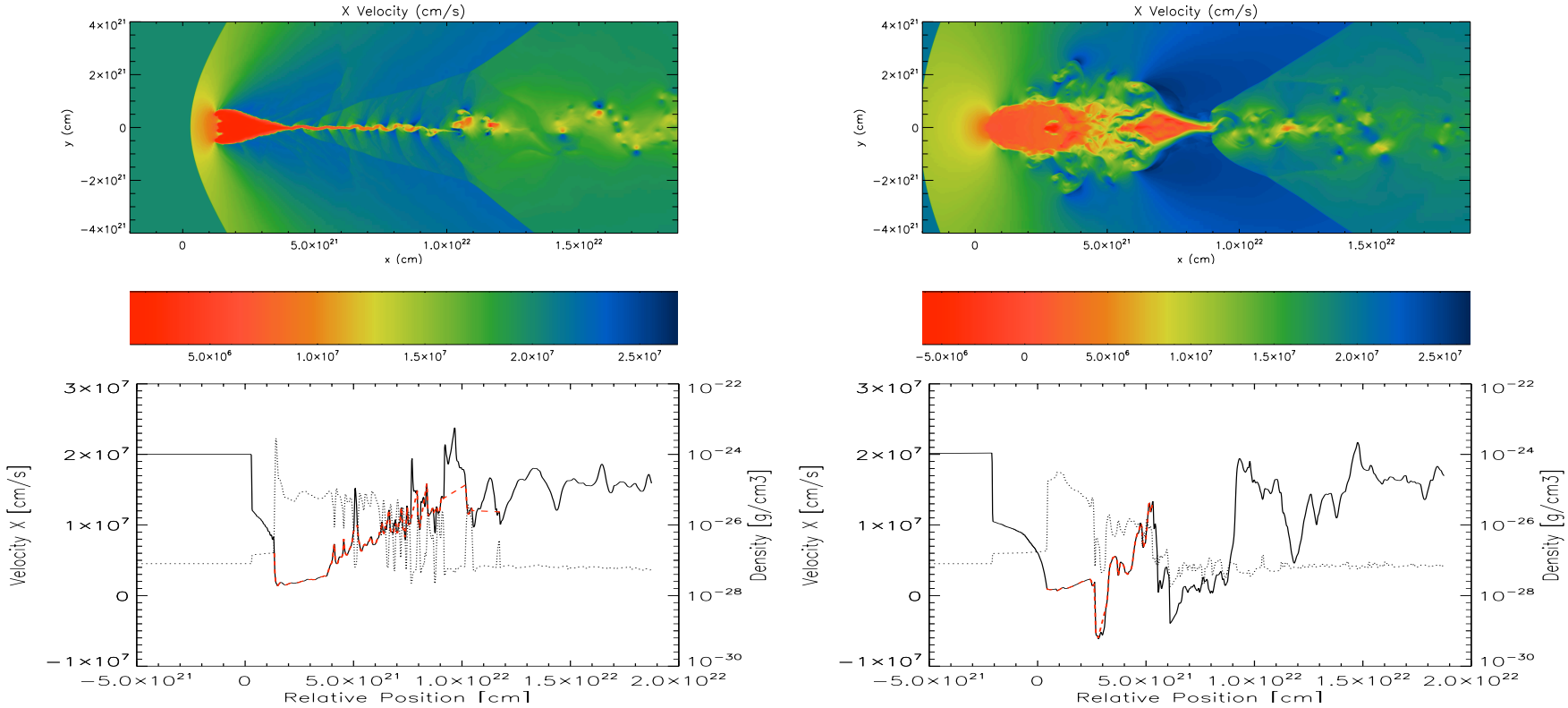

Figure 6.31: Streaming velocity = 200 km/s: Run 7 (left panels, with thermal processes) vs. Run 1 (right panels, without thermal processes) after 50 Myrs. Fig. 6.26 to Fig. 6.27: The upper panels show the 2D x-velocity distribution in color code, while the lower panels describe both the x-velocity and density distribution along the x-axis as explained in Fig. 6.1.

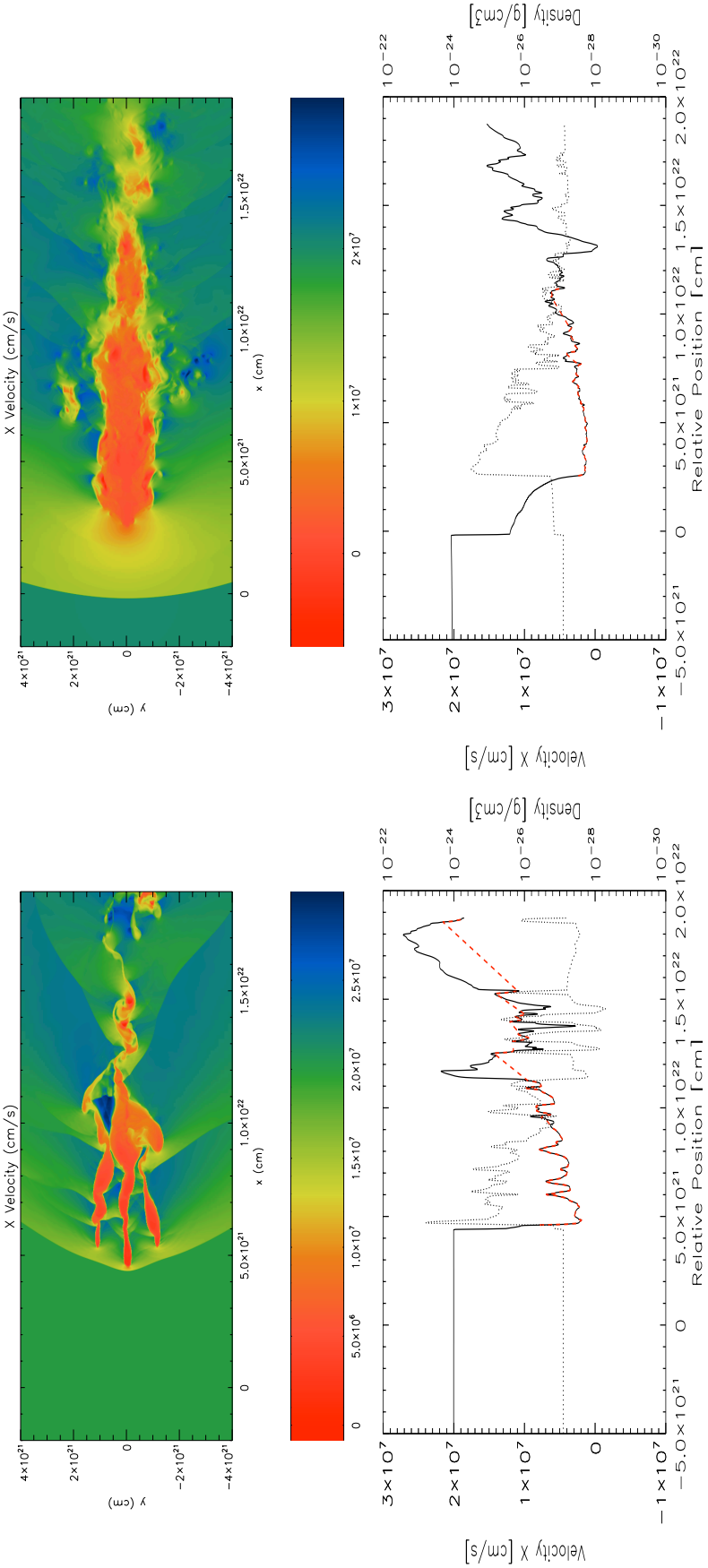

Figure 6.32: Streaming velocity = 200 km/s: Run 7 (left panels, with thermal processes) vs. Run 1 (right panels, without thermal processes) after 100 Myrs.

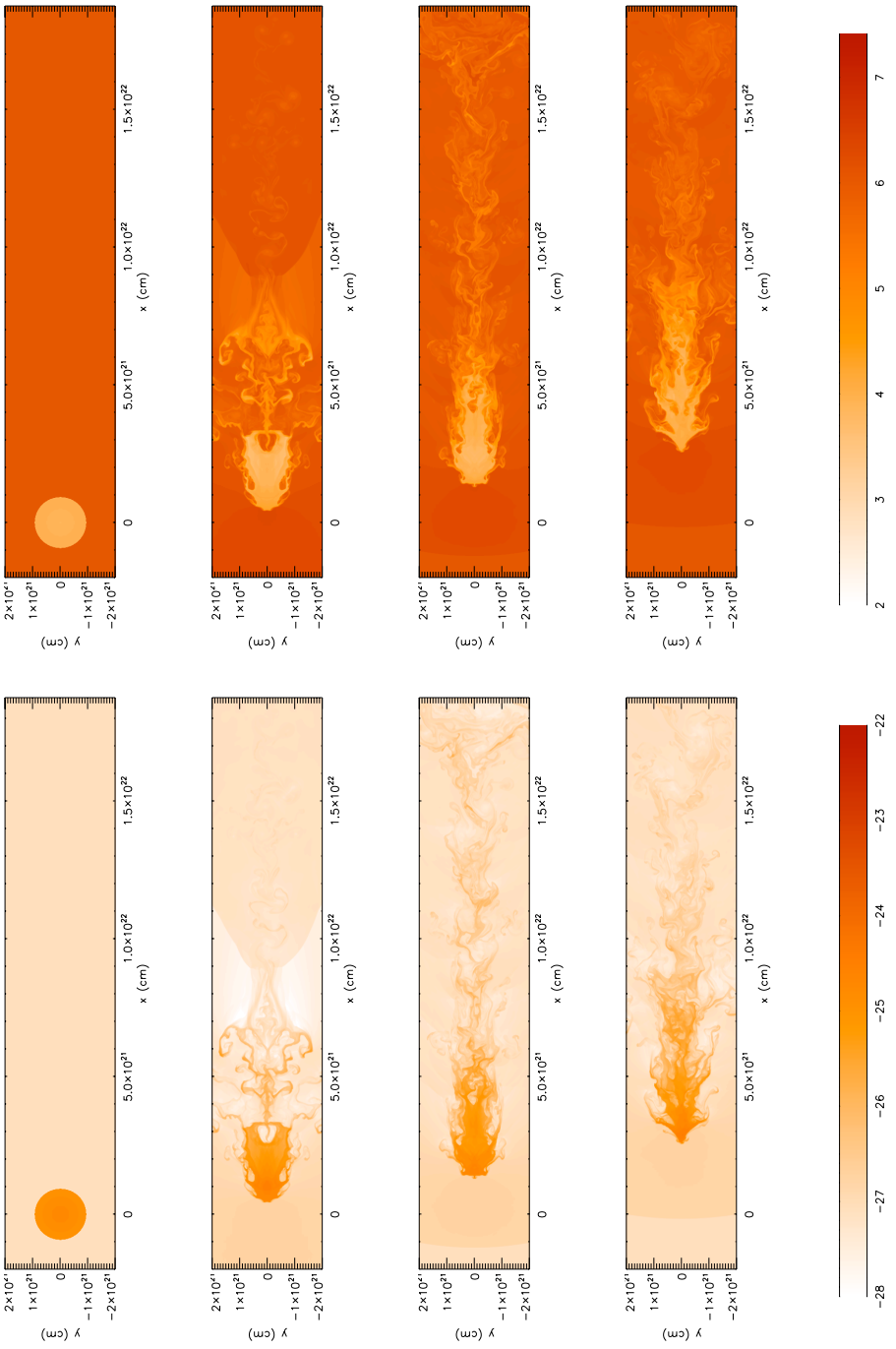

Figure 6.33: As in Fig. 6.5, but for Run 1 ($v_{stream} = 200\,km\,s^{-1}$, no thermal processes).

Chapter 7

Discussion

The aim of this work was first to reproduce observed features of the subclass of high velocity clouds, the compact high velocity clouds (CHVCs), like the head-tail structure visible in column density measurements of neutral hydrogen (see Sec. 7.1) and the multiphase appearance with a cold, dense core and a warmer, more tenuous envelope (see Sec. 7.2). Secondly, the focus was to investigate the question if the observed sharp change in the velocity gradient along the direction of the head-tail structure could be a verification for the theory of an additional gravitational potential in which the baryonic part of the cloud is embedded (see Sec. 7.3). This would rule out a galactic origin, where no large amount of dark matter in CHVCs would be expected and would be an additional evidence for the discussion about CHVCs originating from dark matter satellites.

7.1 Head-Tail Structure

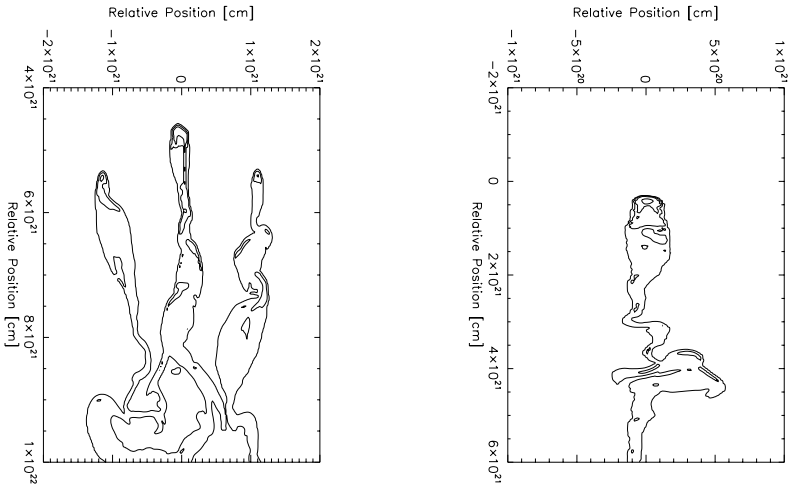

Figure 7.1: Contour plot of the density distributions after 100 Myrs, contour lines at $\rho = 10^{-25}, 10^{-24}, 10^{-23}$ and $10^{-22}\, g\, cm^{-3}$ in each panel. Left: Run 7 (without DM halo). Right: Run 3 (with DM halo).

The observed cometary appearance of the CHVCs can be easily reproduced within a large variety of streaming velocities, when the gaseous part is embedded in a dark matter potential. For clouds with no dark matter content, the compressed area in the front part of the cloud cools due to the larger density and therefore more effective radiative cooling as in runs with dark matter, but the gravitational potential of the gas alone is for a large variety of streaming velocities not strong enough to prevent from Rayleigh-Taylor instabilities (RTI) that occur because of the motion of the rarer interstellar medium into the denser cloud gas. The RTI leads to a fragmentation of the cloud and the resulting finger-like structure, which is not yet observed in CHVCs. Only for velocities as high as $300\,km\,s^{-1}$, the powerful ram pressure confines the cloud to the observed head-tail structure, even without any dark matter content. In Fig. 7.1 a comparison of runs with and without a surrounding halo is shown.

7.2 Multiphase Appearance

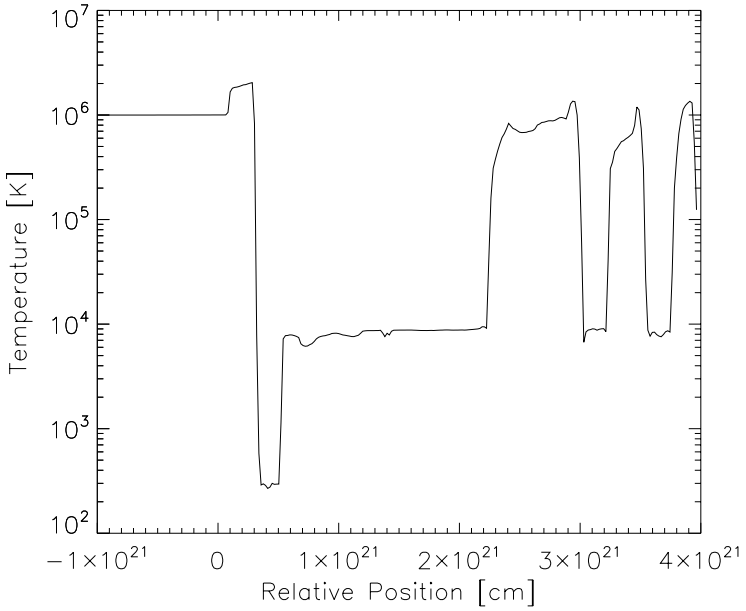

Figure 7.2: 1D temperature cut of Run 3 after 100 Myrs. Beside the temperature rise at the position of the bow shock, also the cold core at a temperature of $\approx$ 300 K and the warmer gas in the tail at $\approx$ 8000 K are visible.

In the simulations for this work the multiphase structure of the clouds is, as expected, highly sensitive to the included heating and cooling processes. As visible in Run 1 without thermal processes the overall appearance of the cloud changes dramatically. A multiphase structure cannot be reproduced without the corresponding heating and cooling modules. For all runs with thermal processes at least one cold, dense core is produced. For setups which lead to a fragmentation of the cloud, the cold gas phase can be found at every finger

tip. The temperatures of the resulting cold and warm phases fit very well the measured quantities (see Sec. 2.2) of about 300 K for the cold phase and 8000 K for the warm phase. The interstellar medium and therefore the hot phase is initially determined to be $1 \times 10^6\,K$, $1.5 \times 10^6\,K$ and $2 \times 10^6\,K$, depending on the run parameters. A 1D temperature cut along the x-axis through the 2D distribution of a run with dark matter halo after 100 Myrs is shown in Fig. 7.2.

7.3 Velocity Gradient

The observed sharp change in the velocity gradient could be successfully reproduced for clouds with dark matter haloes for different conditions of the ambient medium (Run 3: $T_{ISM} = 10^6\,K$, Run 5: $T_{ISM} = 1.5 \times 10^6\,K$, Run 14: $T_{ISM} = 1.5 \times 10^6\,K$) and for all simulated velocities (Run 9: $v_{stream} = 100\,km\,s^{-1}$, Run 3: $v_{stream} = 200\,km\,s^{-1}$, Run 13: $v_{stream} = 300\,km\,s^{-1}$). In all cases, especially for the run with the lowest velocity, the structure takes some time to evolve, but after 100 Myrs a good correlation between the halo edge and a deviation in the velocity gradient can be found.

For runs without dark matter halo, a similar structure appears in a short period of time but vanishes again after a couple of Myrs and result in a almost homogenous velocity gradient after 100 Myrs (f.e. Run 7 after 50 and 100 Myrs), while this feature is getting more dominant with time for clouds with dark matter halo.

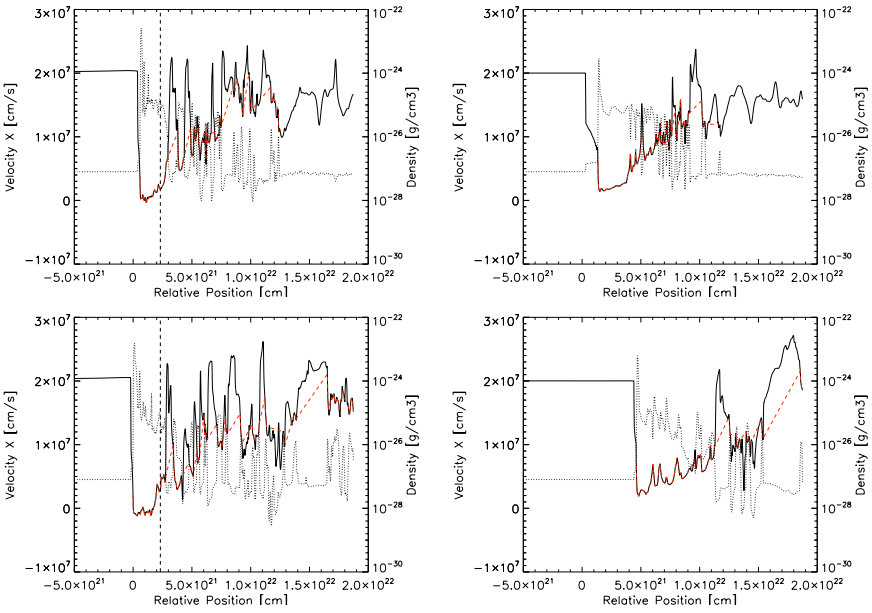

Figure 7.3: Left: Run 8 (with DM halo). Right: Run 7 (without DM halo). The upper panels show a snapshot of the simulation after 50 Myrs while the lower ones describe the velocity and density distribution after 100 Myrs. Line-styles as described in Fig. 6.1.

Chapter 8

Outlook

8.1 Simulations in 3D

Every discussed simulation run in this thesis was performed on a 2-dimensional cartesian grid, after several test-runs to ensure that both the Poisson solver module and the thermal processes show no differences between 2D and 3D runs. The big advantage for simulations in 2D is the much less CPU time and required memory space. A test run for the heating and cooling module for example took 16 min on a single processor in 2D while in 3D eight processors needed 295 min to perform the 100 Myrs run. In addition the file-size increased from 316 KB to 11 MB for each checkpoint file. Even though, for a more detailed study, the following simulation runs will be performed in 3 dimensions to allow for a better comparison of simulated column densities and mass loss with the observations and possible line of sights effects. The program is already adopted for 3 dimensional runs and the first results are shown in Fig. 8.1.

8.2 Heat Conduction

The gas clouds in the above discussed simulation runs have all a very small extent perpendicular to the direction of the head-tail structure due to the mass loss by ram pressure stripping and Kelvin-Helmholtz instabilities. Vieser & Hensler (2007) investigated the effect of heat conduction in molecular clouds, that are surrounded by a hot ambient medium. They showed both analytically and numerically that heat conduction creates a transition zone at the edge of the cloud, in which the density and velocity gradient are lowered and therefore a state can be reached where the Kelvin-Helmholtz instability is suppressed successfully. This leads to a smaller amount of mass loss and therefore to a larger stripping radius (see Fig. 8.2). The implementation of heat conduction in FLASH is part of the PhD thesis by Bastian Arnold at the Institute of Astronomy in Vienna and will deliver preliminary results soon.

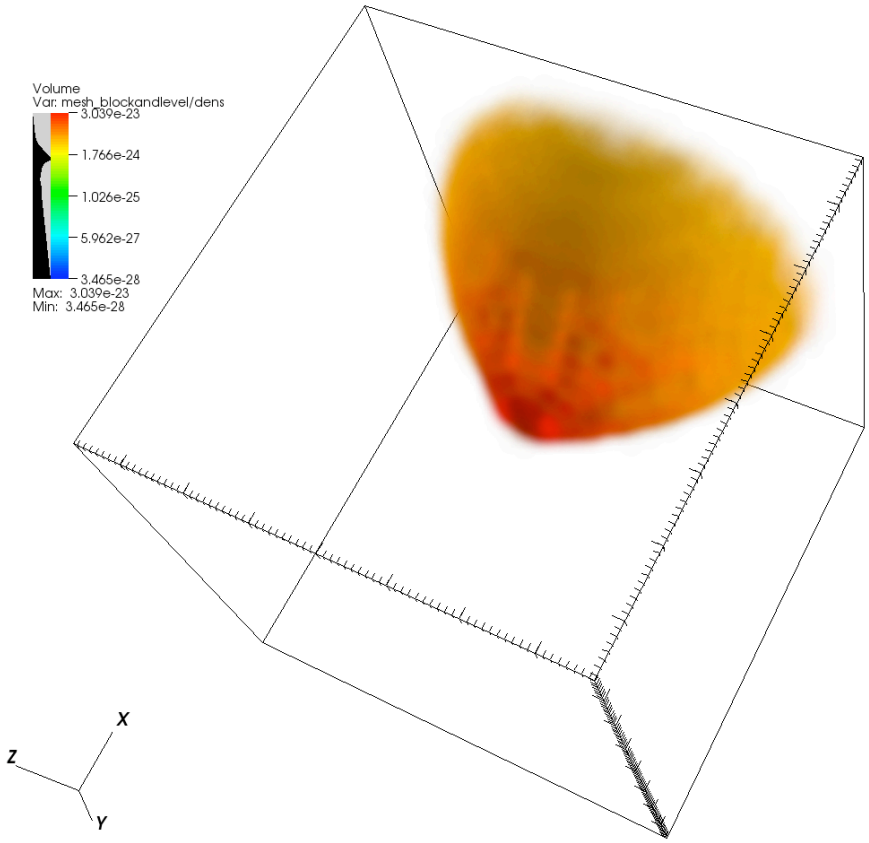

Figure 8.1: Snapshot of one of the first 3D runs after 38 Myrs. Due to the chosen opacity ranges the occurring bow shock is visible in the density distribution.

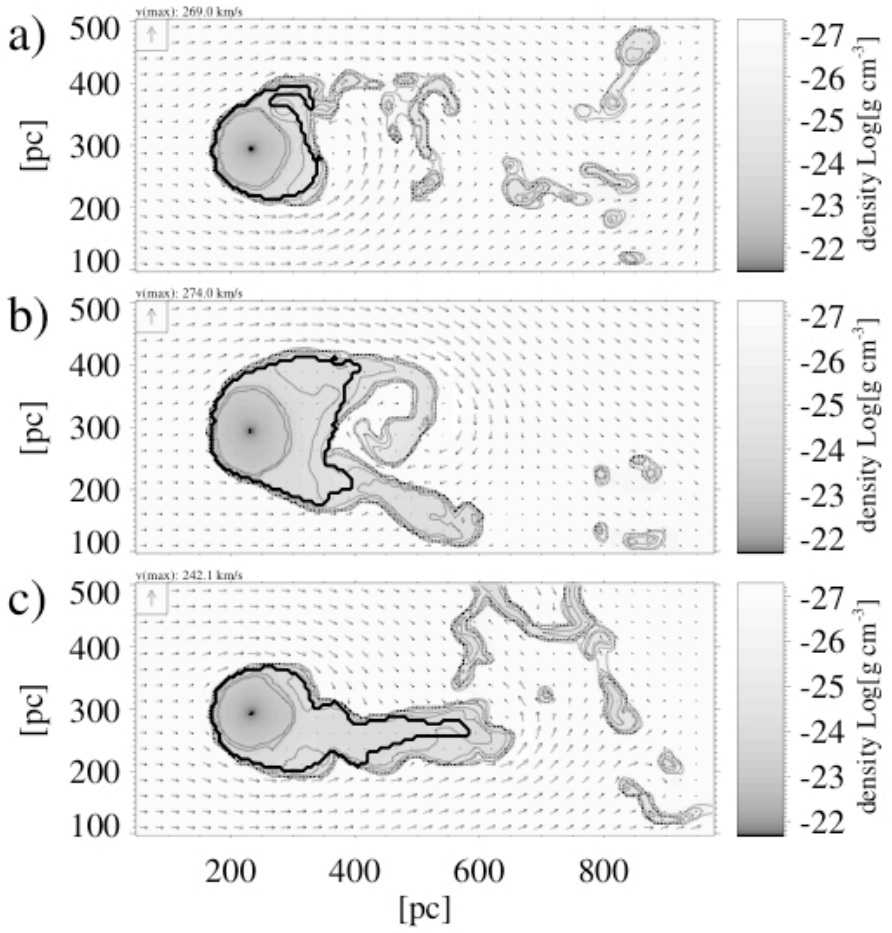

Figure 8.2: Evolution of a molecular cloud after 25 Myr (upper panel), 50 Myr (middle) and 75 Myr (lower). The contours represent the densities of 5, 10, 50, $100 \times \rho_{ISM}$ and the thick contour line indicates the edge of the gravitationally bound gas. Figure from Vieser & Hensler (2007).

Acknowledgements

I want to thank my supervisor Gerhard Hensler for this very interesting topic, for helpful discussions related to both my bachelor and my master thesis and together with Dieter Breitschwerdt and Miguel Avillez for the opportunity to join IP Erasmus in Evora. My team colleagues there, Oliver Gressel and Christian Schwarz helped me a lot to get into "Super-computing". The start with FLASH would have been much harder if Stefan Hirche didn't help me to get to know the basic structure of the FLASH Code. Bastian Arnold provides the possibility to discuss FLASH related topics in the institute. Wolfgang Vieser helped me to set up a stable cloud, while the discussion with Martin Huarte-Espinosa helped me to fix a bug I was looking for for weeks. The software used in this work was in part developed by the DOE-supported ASC / Alliance Center for Astrophysical Thermonuclear Flashes at the University of Chicago.

Beside the persons that helped me directly with this thesis, I would have never got this far without the support of my family. I want to thank my father for his financial support during the study, my mother and my sister (the elder one) for taking care of Tobias to get me some free time, (where "free time" refers to time I can work on my thesis without the time limit to get my son from the kindergarten), and most of all I want to thank my husband, who supported me more than anyone else. We became a great team and managed everything brilliantly together! Last but not least I want to thank my son Tobias and use the opportunity to apologize for this summer holidays where I spent much more time in front of the laptop to finish my thesis than with my family.

Abstract Deutsch

Interstellare Wolken, die hauptsächlich aus neutralem Wasserstoff bestehen, werden seit etwas mehr als 45 Jahren mit Radioteleskopen beobachtet. Durch die sehr schmale 21 cm Linie des neutralem Wasserstoff ist es möglich die Geschwindigkeiten der Wolken sehr genau zu bestimmen, was eine Einteilung in Wolken mit mittlerer (intermediate velocity clouds - IVC) und hoher (high velocity clouds - HVC) Geschwindigkeit relativ zum Ruhesystem der Sonne (local standard of rest -LSR) erlaubt. Hochgeschwindigkeitswolken haben somit per Definition Geschwindigkeiten von zumindest 200 km/s relativ zum Sonnenruhesystem. Während sehr viele HVCs hohe negative Geschwindigkeiten aufweisen, was auf eine Bewegung in Richtung der Sonne schließen lässt, gibt es auch HVC-Komplexe die sich mit hohen Geschwindigkeiten von der Sonne wegbewegen, was zu hohen positiven Geschwindigkeiten führt. Seit der Entdeckung dieser interstellaren Wolken besteht eine Diskussion über einen möglichen Ursprung, die bis heute anhält. Der Grund für die große Diversität der einzelnen Theorien ist vor allem die Schwierigkeit der Distanzmessung. Um den Abstand zwischen Sonne und einer beliebigen Gaswolke direkt messen zu können, sind Sterne mit bekannten Abstand in der Sichtlinie der Wolke notwendig in deren Spektren Linien der Wolke gefunden oder nicht gefunden werden, was zu minimalen oder maximalen Distanzen führt. Während für die großen Wolkenkomplexe mittlerweile recht gute Distanzmessungen vorliegen, ist es für die Unterklasse der kompakten HVCs (CHVC) wegen ihres geringen Winkeldurchmessers selten der Fall, dass sich in der exakten Sichtrichtung passende Objekte befinden. Ohne Distanzmessung ist es allerdings nicht möglich die Masse bzw. die tatsächliche Ausdehnung der Wolke zu bestimmen. So gibt es Theorien, welche die CHVCs in Entfernungen von wenigen kpc in den galaktischen Halo setzen, während andere sie der Lokalen Gruppe mit Entfernungen von bis zu einem Mpc zuordnen, was sich natürlich dramatisch in den zugehörigen Massenberechnungen niederschlägt. Durch Beobachtungen mit immer besseren Auflösungen in unterschiedlichen Wellenlängenbereichen von galaktischen als auch extragalaktischen HVCs kristallisieren sich Szenarien heraus, welche die aktuell verfügbaren Daten besonders gut beschreiben bzw. reproduzieren können. Eine dieser Theorien beschäftigt sich mit dem kosmologischen Hintergrund der hierarchischen Strukturbildung des Universums und der daraus folgenden Verteilung der dunklen Materie. In Simulationen darüber zeigt sich, dass sich rund um die Milchstrasse deutlich mehr Satellitenobjekte befinden sollten, als derzeit als Satellitengalaxien beobachtet werden. Eine mögliche Erklärung für diese Diskrepanz könnte die große Anzahl an CHVCs sein, wenn diese Teil der immer noch andauernden hierarchischen Strukturbildung des Universums sind. In diesem Fall kondensiert Gas in einem Halo aus dunkler Materie und wird dadurch erst von dem

umliegenden heißen Gas unterscheid- und somit beobachtbar. Im Laufe der Akkretion durch eine größere Galaxie, wie zum Beispiel der Milchstrasse, tritt das Paket aus Gas und dunkler Materie in den galaktischen Halo ein. Dabei wird der Staudruck am vorderen Ende der Wolke durch steigende Dichte des umliegenden Mediums immer größer, was zu einer Abstreifung von Wolkenmaterial führt. Da dunkle Materie (DM) ausschließlich gravitativ wechselwirkt bleibt diese davon unbeeinflusst, was dazu führen kann, dass Gas aus dem Gravitationspotential des DM-Halos hinausgedrückt wird. An dieser Stelle, an der das Gas gravitativ ungebunden wird, erwartet man eine deutliche Änderung des Geschwindigkeitsgradienten, was auch bei mehreren HVCs und CHVCs beobachtet wurde. Eine numerische Überprüfung dieser Theorie wird mit dieser Diplomarbeit durchgeführt. Mit Hilfe von FLASH2.5, einem Hydrodynamik Code mit adaptiver Gitterverfeinerung ist ein derartiges Szenario simuliert worden. Ausgehend von einer ruhenden Wolke, die unter Eigengravitation, mit den inkludierten Heiz- und Kühlprozessen, sowie in einem Halo aus dunkler Materie über 100 Millionen Jahre stabil ist, wurden Simulationen mit unterschiedlichen Parametern gerechnet. Dabei konnten neben der Änderung des Dichtegradienten auch die kometenartige Struktur, sowie das multiphasen Erscheinungsbild der beobachteten Wolken erfolgreich reproduziert werden, wenn diese in einen DM-Halo eingebettet waren. Ohne DM-Halo ist es nicht möglich die beobachtete Geschwindigkeitsverteilung über längere Zeit zu stabilisieren. Weiters fragmentieren die Wolken in Simulationsläufen ohne DM-Halo auf Grund von Rayleigh-Taylor Instabilitäten. Damit gelingt mit dieser Arbeit ein weiterer Hinweis für die Theorie von kompakten Hochgeschwindigkeitswolken in DM-Halos und somit für einen Ursprung aus der Strukturbildung des Universums.

Abstract English

Interstellar gas clouds, that consist mainly of neutral hydrogen are observed with radio telescopes since 1963. Since the 21 cm fine-structure line of neutral hydrogen is a very narrow and sharp line, the velocities of the clouds can be determined very accurately, which allows for a classification of clouds with intermediate (IVC) and high (HVC) velocity relative to the local standard of rest (LSR). HVCs have therefore velocities of at least 200 km/s relative to the LSR, which include clouds with high positive velocities, that are moving away from the sun, as well as clouds with high negative velocities, which indicates a motion towards the sun. The theories about the origin of the observed gas clouds diverge between a galactic origin with distances of a few kpc to theories supporting an extragalactic origin with distances between the sun and the clouds as high as 1 Mpc. This work focus on the theory of an origin of HVCs (in particular the more compact subclass - CHVCs) in dark matter mini-halos which allow gas to condense and therefore become observable within their hot ambient medium. This theory bases on the hierarchical structure formation within a Λ-CDM universe. Several dark matter simulations of this on-going formation scenario show a much larger number of satellite objects than observed as satellite galaxies around the Milky Way Galaxy (MWG). If HVCs origin from a similar formation process as the satellite galaxies, they should be embedded in an additional gravitational potential, arising from the mass of the non-baryonic dark matter halo. During the accretion, the gas cloud will enter the galactic halo and will therefore face an increasing density gradient. This leads to a higher ram pressure, which can strip off material from the gas cloud. While the baryonic matter in the cloud is affected by drag force, the dark matter interacts only gravitationally and is not decelerated. Therefore it is very likely that stripped off gas becomes unbound and leaves the dark matter dominated gravitational potential. At the edge of the dark matter halo a rapid change in the velocity gradient would be expected, which is already observed in several HVCs and CHVCs. A numerical verification of this theory was the subject of this master thesis, which was realised with FLASH2.5, a grid-based hydrodynamic code with adaptive mesh refinement. Based on a stable self-gravitating gas sphere in both hydrodynamic and thermal equilibrium surrounded by a hot ambient medium, this work shows how different additional gravitational potentials influence the effect of ram pressure stripping. Performing the simulations for a periode of 100 Myrs, both the cometary appearance and the observed multiphase structure could be successfully reproduced for clouds that are embedded in a dark matter mini-halo, while without an additional gravitational potential the clouds fragment due to Rayleigh-Taylor instabilities and form rather a finger-like than than the observed head-tail structure. Only for runs with streaming velocities

as high as 300 km/s the head-tail structure is created also for runs without dark matter. Furthermore the rapid change of the velocity gradient in the gas material, when it is pushed out of the dark matter halo is reproduced very well. In runs without dark matter a similar distribution can be found during the simulation run, but in comparison to the runs with halo, where this feature is getting more distinctive over time, it is not stable but disappears again after a short time.Therefore this work accomplish an additional hint for the theory of the CHVCs in DM haloes and furthermore for an origin out of the hierarchical structure formation of the universe.

Curriculum Vitae

Nachname(n) / Vorname(n)	**Plöckinger Sylvia Isolde**
Adresse(n)	Laaben 30/10, 3053 Laaben bei Neulengbach
E-mail	ploeckinger@astro.univie.ac.at
Staatsangehörigkeit	Österreich
Geburtsdatum	31.08.1983
Schul- und Universitätsbildung	
Zeitraum	03/2007 - 09/2009
Bezeichnung	Magisterstudium Astronomie (A 066 861)
Betreuer der Diplomarbeit	Univ.-Prof. Dipl.-Phys. Dr. Gerhard Hensler
Titel der Diplomarbeit	Head Tail High Velocity Clouds: A possibility to test the theory of dark matter mini-halos
Name und Art der Bildungseinrichtung	Institut für Astronomie Türkenschanzstrasse 17, 1180 Wien
Stufe der nationalen oder internationalen Klassifikation	Mag. rer. nat.
Zeitraum	10/2002 - 02/2003 und 10/2003 - 12/2006
Bezeichnung	Bakkalaureatsstudium Astronomie (A 033 661)
Betreuer der Bakk. Arbeit	Univ.-Prof. Dipl.-Phys. Dr. Gerhard Hensler
Titel der Bakk. Arbeit	High Velocity Clouds
Name und Art der Bildungseinrichtung	Institut für Astronomie Türkenschanzstrasse 17, 1180 Wien
Stufe der nationalen oder internationalen Klassifikation	Bakk. rer. nat.
Zeitraum	09/1993 - 05/2001
Name und Art der Bildungseinrichtung	BG und BRG Wels Anton-Brucknerstrasse 16, 4600 Wels
Stufe der nationalen oder internationalen Klassifikation	Matura
Tagungen, Workshops	
Zeitraum	21.09.2009 - 25.09.2009
Titel	The Annual Fall Meeting of the Astronomische Gesellschaft (AG) "Deciphering the Universe through Spectroscopy"
Ort	Potsdam, Deutschland
Zeitraum	02.09.2009 - 04.09.2009
Titel	Joint Annual Meeting of ÖPG, SPS, ÖGA
Ort	Innsbruck, Österreich
Zeitraum	04.02.2008 - 23.02.2008
Titel	IP Erasmus Supercomputing and Astrophysical Fluid Flow Modelling
Ort	Evora, Portugal
Sonstiges	
Zeitraum	10/2005 - 09/2007
Tätigkeit	Mitglied der Studentenvertretung Astronomie

Bibliography

Barentine, J. C., et al. 2008, in Astronomical Society of the Pacific Conference Series, Vol. 393, New Horizons in Astronomy, ed. A. Frebel, J. R. Maund, J. Shen, & M. H. Siegel, 179–+

Belokurov, V., et al. 2007, ApJ, 658, 337

Benjamin, R. A., & Danly, L. 1997, ApJ, 481, 764

Benjamin, R. A., Wakker, B. P., Otte, B., & Dixon, W. V. 2006, in Astronomical Society of the Pacific Conference Series, Vol. 348, Astrophysics in the Far Ultraviolet: Five Years of Discovery with FUSE, ed. G. Sonneborn, H. W. Moos, & B.-G. Andersson, 391–+

Binney, J., Nipoti, C., & Fraternali, F. 2009, ArXiv e-prints

Binney, J., & Tremaine, S. 1988, Galactic Dynamics (Princeton Series in Astrophysics)

Black, J. H. 1987, in Astrophysics and Space Science Library, Vol. 134, Interstellar Processes, ed. D. J. Hollenbach & H. A. Thronson, Jr., 731–744

Bland-Hawthorn, J., & Maloney, P. R. 2002, in Astronomical Society of the Pacific Conference Series, Vol. 254, Extragalactic Gas at Low Redshift, ed. J. S. Mulchaey & J. T. Stocke, 267–+

Blitz, L., Spergel, D. N., Teuben, P. J., Hartmann, D., & Burton, W. B. 1999, ApJ, 514, 818

Blumenthal, G. R., Faber, S. M., Primack, J. R., & Rees, M. J. 1984, Nature, 311, 517

Boehringer, H., & Hensler, G. 1989, A&A, 215, 147

Bonnor, W. B. 1956, MNRAS, 116, 351

Boomsma, R., Oosterloo, T. A., Fraternali, F., van der Hulst, J. M., & Sancisi, R. 2008, A&A, 490, 555

Braun, R., & Burton, W. B. 1999, A&A, 341, 437

—. 2000, A&A, 354, 853

Brüns, C., Kerp, J., Kalberla, P. M. W., & Mebold, U. 2000, A&A, 357, 120

Brüns, C., Kerp, J., & Pagels, A. 2001, A&A, 370, L26

Brüns, C., & Westmeier, T. 2004, A&A, 426, L9

Burkert, A. 1995, ApJ, 447, L25+

—. 1997, ApJ, 474, L99+

Burkert, A., & Silk, J. 1999, in Dark matter in Astrophysics and Particle Physics, ed. H. V. Klapdor-Kleingrothaus & L. Baudis, 375–+

Burles, S., Nollett, K. M., & Turner, M. S. 2001, ApJ, 552, L1

Burton, W. B., Braun, R., & Chengalur, J. N. 2001, A&A, 375, 227

Burton, W. B., & Lockman, F. J. 1999, A&A, 349, 7

Carswell, R. F., Rauch, M., Weymann, R. J., Cooke, A. J., & Webb, J. K. 1994, MNRAS, 268, L1+

Collins, J. A., Shull, J. M., & Giroux, M. L. 2004, ApJ, 605, 216

—. 2007, ApJ, 657, 271

Connors, T. W., Kawata, D., & Gibson, B. K. 2006, MNRAS, 371, 108

Cravens, T. E., & Dalgarno, A. 1978, ApJ, 219, 750

Dalgarno, A., & McCray, R. A. 1972, ARA&A, 10, 375

Danly, L., Albert, C. E., & Kuntz, K. D. 1993, ApJ, 416, L29+

Dar, A. 1995, ApJ, 449, 550

Davis, M., Efstathiou, G., Frenk, C. S., & White, S. D. M. 1985, ApJ, 292, 371

de Bernardis, P., et al. 2002, ApJ, 564, 559

de Heij, V., Braun, R., & Burton, W. B. 2002a, A&A, 392, 417

—. 2002b, A&A, 391, 159

—. 2002c, A&A, 391, 67

de Jong, T. 1977, A&A, 55, 137

Dessauges-Zavadsky, M., Combes, F., & Pfenniger, D. 2007, A&A, 473, 863

Dobke, B. M., King, L. J., Fassnacht, C. D., & Auger, M. W. 2009, MNRAS, 397, 311

Ebert, R. 1955, Zeitschrift fur Astrophysik, 37, 217

Epstein, R. L., Arnett, W. D., & Schramm, D. N. 1976, ApJS, 31, 111

Espresate, J., Cantó, J., & Franco, J. 2002, ApJ, 575, 194

Ewen, H. I., & Purcell, E. M. 1951, Nature, 168, 356

Falgarone, E., Puget, J.-L., & Perault, M. 1992, A&A, 257, 715

Ferrara, A., & Field, G. B. 1994, ApJ, 423, 665

Fox, A. J., Savage, B. D., & Wakker, B. P. 2006, ApJS, 165, 229

Fox, A. J., Savage, B. D., Wakker, B. P., Richter, P., Sembach, K. R., & Tripp, T. M. 2004, ApJ, 602, 738

Fryxell, B., et al. 2000, ApJS, 131, 273

Fujita, Y., & Nagashima, M. 1999, ApJ, 516, 619

Ganguly, R., Sembach, K. R., Savage, B. D., & Tripp, T. M. 2006, in Astronomical Society of the Pacific Conference Series, Vol. 348, Astrophysics in the Far Ultraviolet: Five Years of Discovery with FUSE, ed. G. Sonneborn, H. W. Moos, & B.-G. Andersson, 394–+

Gao, L., White, S. D. M., Jenkins, A., Stoehr, F., & Springel, V. 2004, MNRAS, 355, 819

Gelb, J. M., & Bertschinger, E. 1994a, ApJ, 436, 467

—. 1994b, ApJ, 436, 491

Gibson, B. K., Fenner, Y., Maddison, S. T., & Kawata, D. 2002, in Astronomical Society of the Pacific Conference Series, Vol. 254, Extragalactic Gas at Low Redshift, ed. J. S. Mulchaey & J. T. Stocke, 225–+

Giocoli, C., Moreno, J., Sheth, R. K., & Tormen, G. 2007, MNRAS, 376, 977

Giovanelli, R., Verschuur, G. L., & Cram, T. R. 1973, A&AS, 12, 209

Grillmair, C. J. 2006, ApJ, 651, L29

Gunn, J. E., & Gott, J. R. I. 1972, ApJ, 176, 1

Habing, H. J. 1968, Bull. Astron. Inst. Netherlands, 19, 421

Hinshaw, G., et al. 2003, ApJS, 148, 135

Hoffman, G. L., Salpeter, E. E., & Hirani, A. 2004, AJ, 128, 2932

Holweger, H. 2001, in American Institute of Physics Conference Series, Vol. 598, Joint SOHO/ACE workshop "Solar and Galactic Composition", ed. R. F. Wimmer-Schweingruber, 23–30

Hoopes, C. G., Sembach, K. R., Hébrard, G., Moos, H. W., & Knauth, D. C. 2003, ApJ, 586, 1094

Hopp, U., Schulte-Ladbeck, R. E., & Kerp, J. 2007, MNRAS, 374, 1164

Hulsbosch, A. N. M., & Wakker, B. P. 1988, A&AS, 75, 191

Ibata, R., Irwin, M., Lewis, G. F., & Stolte, A. 2001, ApJ, 547, L133

Ibata, R. A., Gilmore, G., & Irwin, M. J. 1994, Nature, 370, 194

Ibata, R. A., & Lewis, G. F. 1998, ApJ, 500, 575

Jenkins, E. B., Tripp, T. M., Woźniak, P. R., Sofia, U. J., & Sonneborn, G. 1999, ApJ, 520, 182

Kalberla, P. M. W., & Haud, U. 2006, A&A, 455, 481

Klypin, A., Kravtsov, A. V., Valenzuela, O., & Prada, F. 1999, ApJ, 522, 82

Konz, C., Brüns, C., & Birk, G. T. 2002, A&A, 391, 713

Koribalski, B., Johnston, S., & Otrupcek, R. 1994, MNRAS, 270, L43+

Kravtsov, A. V., Gnedin, O. Y., & Klypin, A. A. 2004, ApJ, 609, 482

Lockman, F. J. 2003, ApJ, 591, L33

Lohner, R., Morgan, K., Peraire, J., & Vahdati, M. 1987, International Journal for Numerical Methods in Fluids, 7, 1093

MacTavish, C. J., et al. 2006, ApJ, 647, 799

Majewski, S. R., Skrutskie, M. F., Weinberg, M. D., & Ostheimer, J. C. 2003, ApJ, 599, 1082

Maloney, P. R., & Putman, M. E. 2003, ApJ, 589, 270

Mathewson, D. S., Cleary, M. N., & Murray, J. D. 1974, ApJ, 190, 291

McKee, C. F., & Ostriker, J. P. 1977, ApJ, 218, 148

Miller, E. D., & Bregman, J. N. 2005, in Astronomical Society of the Pacific Conference Series, Vol. 331, Extra-Planar Gas, ed. R. Braun, 261–+

Miller, E. D., Bregman, J. N., & Wakker, B. P. 2009, ApJ, 692, 470

Miville-Deschenes, M. ., Boulanger, F., Martin, P. G., Lockman, F. J., Reach, W. T., & Noriega-Crespo, A. 2006, ArXiv Astrophysics e-prints

Miville-Deschenes, M.-A. 2006, in CMB and Physics of the Early Universe

Miville-Deschênes, M.-A., Boulanger, F., Reach, W. T., & Noriega-Crespo, A. 2005, ApJ, 631, L57

Moore, B., Ghigna, S., Governato, F., Lake, G., Quinn, T., Stadel, J., & Tozzi, P. 1999, ApJ, 524, L19

Moos, H. W., et al. 2002, ApJS, 140, 3

Mori, M., & Burkert, A. 2000, ApJ, 538, 559

Morras, R., Bajaja, E., Arnal, E. M., & Pöppel, W. G. L. 2000, A&AS, 142, 25

Muller, C. A. 1963, Nature, 200, 155

Münch, G. 1956, PASP, 68, 351

Murphy, E. M., Lockman, F. J., & Savage, B. D. 1995, ApJ, 447, 642

Nulsen, P. E. J. 1982, MNRAS, 198, 1007

Olano, C. A. 2006, in Revista Mexicana de Astronomia y Astrofisica Conference Series, Vol. 26, Revista Mexicana de Astronomia y Astrofisica Conference Series, 183–+

Olano, C. A. 2008, A&A, 485, 457

Oort, J. H. 1969, Nature, 224, 1158

Peebles, P. J. E. 1982a, ApJ, 259, 442

—. 1982b, ApJ, 263, L1

Peek, J. E. G., Putman, M. E., McKee, C. F., Heiles, C., & Stanimirović, S. 2007, ApJ, 656, 907

Pisano, D. J., Barnes, D. G., Gibson, B. K., Staveley-Smith, L., Freeman, K. C., & Kilborn, V. A. 2004, ApJ, 610, L17

—. 2007, ApJ, 662, 959

Putman, M. E., Bland-Hawthorn, J., Veilleux, S., Gibson, B. K., Freeman, K. C., & Maloney, P. R. 2003, ApJ, 597, 948

Putman, M. E., & Moore, B. 2002, in Astronomical Society of the Pacific Conference Series, Vol. 273, The Dynamics, Structure & History of Galaxies: A Workshop in Honour of Professor Ken Freeman, ed. G. S. Da Costa & H. Jerjen, 195–+

Putman, M. E., Thom, C., Gibson, B. K., & Staveley-Smith, L. 2004, ApJ, 603, L77

Putman, M. E., et al. 2002, AJ, 123, 873

Quilis, V., & Moore, B. 2001, ApJ, 555, L95

Richter, P., Sembach, K. R., Wakker, B. P., & Savage, B. D. 2001, ApJ, 562, L181

Richter, P., Westmeier, T., & Brüns, C. 2005, A&A, 442, L49

Roediger, E., & Hensler, G. 2005, A&A, 433, 875

Schwarz, U. J., Wakker, B. P., & van Woerden, H. 1995, A&A, 302, 364

Sembach, K. R. 2002, in Astronomical Society of the Pacific Conference Series, Vol. 254, Extragalactic Gas at Low Redshift, ed. J. S. Mulchaey & J. T. Stocke, 283–+

Sembach, K. R., Gibson, B. K., Fenner, Y., & Putman, M. E. 2002, ApJ, 572, 178

Sembach, K. R., et al. 2004, ApJS, 150, 387

Shapiro, P. R., & Field, G. B. 1976, ApJ, 205, 762

Slyz, A. D., Devriendt, J. E. G., Bryan, G., & Silk, J. 2005, MNRAS, 356, 737

Smoker, J. V., Lynn, B. B., Christian, D. J., & Keenan, F. P. 2006, MNRAS, 370, 151

Smoker, J. V., Roger, R. S., Keenan, F. P., Davies, R. D., Lang, R. H., & Bates, B. 2001, A&A, 380, 673

Songaila, A., Cowie, L. L., Hu, E. M., & Gardner, J. P. 1994, ApJS, 94, 461

Spitoni, E., Recchi, S., & Matteucci, F. 2008, A&A, 484, 743

Spitzer, L. J. 1956, ApJ, 124, 20

Springel, V., et al. 2005, Nature, 435, 629

Sternberg, A., McKee, C. F., & Wolfire, M. G. 2002, ApJS, 143, 419

Sutherland, R. S., & Dopita, M. A. 2002, Astrophysics of the Diffuse Universe (Astronomy and Astrophysics Library)

Thilker, D. A., Braun, R., Walterbos, R. A. M., Corbelli, E., Lockman, F. J., Murphy, E., & Maddalena, R. 2004, ApJ, 601, L39

Thom, C., Peek, J. E. G., Putman, M. E., Heiles, C., Peek, K. M. G., & Wilhelm, R. 2008, ApJ, 684, 364

Thom, C., Putman, M. E., Gibson, B. K., Christlieb, N., Flynn, C., Beers, T. C., Wilhelm, R., & Lee, Y. S. 2006, ApJ, 638, L97

Thorburn, J. A. 1994, ApJ, 421, 318

Tripp, T. M., et al. 2003, AJ, 125, 3122

Tufte, S. L., Wilson, J. D., Madsen, G. J., Haffner, L. M., & Reynolds, R. J. 2002, ApJ, 572, L153

Vieser, W., & Hensler, G. 2001, in Astronomische Gesellschaft Meeting Abstracts, Vol. 18, Astronomische Gesellschaft Meeting Abstracts, ed. E. R. Schielicke, 106–+

Vieser, W., & Hensler, G. 2007, A&A, 472, 141

Wakker, B., Howk, C., Schwarz, U., van Woerden, H., Beers, T., Wilhelm, R., Kalberla, P., & Danly, L. 1996a, ApJ, 473, 834

Wakker, B. P. 1991a, A&A, 250, 499

—. 1991b, A&AS, 90, 495

—. 2001, ApJS, 136, 463

Wakker, B. P. 2004, in IAU Symposium, Vol. 217, Recycling Intergalactic and Interstellar Matter, ed. P.-A. Duc, J. Braine, & E. Brinks, 2–+

Wakker, B. P., & Boulanger, F. 1986, A&A, 170, 84

Wakker, B. P., & Mathis, J. S. 2000, ApJ, 544, L107

Wakker, B. P., & Schwarz, U. J. 1991, A&A, 250, 484

Wakker, B. P., & van Woerden, H. 1991, A&A, 250, 509

—. 1997, ARA&A, 35, 217

Wakker, B. P., van Woerden, H., Schwartz, U. J., Peletier, R. F., & Douglas, N. G. 1996b, A&A, 306, L25+

Wakker, B. P., van Woerden, H., Schwarz, U. J., Peletier, R. F., Douglas, N. G., Danly, L., & de Boer, K. S. 1996c, in IAU Symposium, Vol. 169, Unsolved Problems of the Milky Way, ed. L. Blitz & P. J. Teuben, 605–+

Wakker, B. P., York, D. G., Wilhelm, R., Barentine, J. C., Richter, P., Beers, T. C., Ivezić, Ž., & Howk, J. C. 2008, ApJ, 672, 298

Wakker, B. P., et al. 2007, ApJ, 670, L113

Wannier, P., & Wrixon, G. T. 1972, ApJ, 173, L119+

Westmeier, T., Braun, R., Brüns, C., Kerp, J., & Thilker, D. A. 2007, New Astronomy Review, 51, 108

Westmeier, T., Braun, R., & Thilker, D. 2005a, A&A, 436, 101

Westmeier, T., Brüns, C., & Kerp, J. 2004, in Astronomical Society of the Pacific Conference Series, Vol. 327, Satellites and Tidal Streams, ed. F. Prada, D. Martinez Delgado, & T. J. Mahoney, 297–+

Westmeier, T., Brüns, C., & Kerp, J. 2005b, in Astronomical Society of the Pacific Conference Series, Vol. 331, Extra-Planar Gas, ed. R. Braun, 105–+

Westmeier, T., Brüns, C., & Kerp, J. 2005c, A&A, 432, 937

—. 2008a, MNRAS, 390, 1691

Westmeier, T., Brüns, C., & Kerp, J. 2008b, in Astronomical Society of the Pacific Conference Series, Vol. 393, New Horizons in Astronomy, ed. A. Frebel, J. R. Maund, J. Shen, & M. H. Siegel, 283–+

Wolfire, M. G., Hollenbach, D., McKee, C. F., Tielens, A. G. G. M., & Bakes, E. L. O. 1995a, ApJ, 443, 152

Wolfire, M. G., McKee, C. F., Hollenbach, D., & Tielens, A. G. G. M. 1995b, ApJ, 453, 673

Zwicky, F. 1933, Helvetica Physica Acta, 6, 110

Note: Ich habe mich bemüht, sämtliche Inhaber der Bildrechte ausfindig zu machen und ihre Zustimmung zur Verwendung der Bilder in dieser Arbeit eingeholt. Sollte dennoch eine Urheberrechtsverletzung bekannt werden, ersuche ich um Meldung bei mir.